

University of Windsor

Scholarship at UWindor

Electronic Theses and Dissertations

Theses, Dissertations, and Major Papers

2013

Advancement of Shock-wave Induced Spraying Process through the Study of Gas and Particle Flow Fields

Mohammad Karimi Esfahani
University of Windsor

Follow this and additional works at: <https://scholar.uwindsor.ca/etd>

Recommended Citation

Karimi Esfahani, Mohammad, "Advancement of Shock-wave Induced Spraying Process through the Study of Gas and Particle Flow Fields" (2013). *Electronic Theses and Dissertations*. 4715.
<https://scholar.uwindsor.ca/etd/4715>

This online database contains the full-text of PhD dissertations and Masters' theses of University of Windsor students from 1954 forward. These documents are made available for personal study and research purposes only, in accordance with the Canadian Copyright Act and the Creative Commons license—CC BY-NC-ND (Attribution, Non-Commercial, No Derivative Works). Under this license, works must always be attributed to the copyright holder (original author), cannot be used for any commercial purposes, and may not be altered. Any other use would require the permission of the copyright holder. Students may inquire about withdrawing their dissertation and/or thesis from this database. For additional inquiries, please contact the repository administrator via email (scholarship@uwindsor.ca) or by telephone at 519-253-3000ext. 3208.

Advancement of Shock-wave Induced Spraying Process through
the Study of Gas and Particle Flow Fields

by

Mohammad Karimi Esfahani

A Dissertation

Submitted to the Faculty of Graduate Studies
through Mechanical, Automotive and Material Engineering
in Partial Fulfillment of the Requirements for
the Degree of Doctor of Philosophy at the
University of Windsor

Windsor, Ontario, Canada

2012

© 2012 Mo Karimi



Library and Archives
Canada

Published Heritage
Branch

395 Wellington Street
Ottawa ON K1A 0N4
Canada

Bibliothèque et
Archives Canada

Direction du
Patrimoine de l'édition

395, rue Wellington
Ottawa ON K1A 0N4
Canada

Your file Votre référence
ISBN: 978-0-494-79150-9

Our file Notre référence
ISBN: 978-0-494-79150-9

NOTICE:

The author has granted a non-exclusive license allowing Library and Archives Canada to reproduce, publish, archive, preserve, conserve, communicate to the public by telecommunication or on the Internet, loan, distribute and sell theses worldwide, for commercial or non-commercial purposes, in microform, paper, electronic and/or any other formats.

The author retains copyright ownership and moral rights in this thesis. Neither the thesis nor substantial extracts from it may be printed or otherwise reproduced without the author's permission.

In compliance with the Canadian Privacy Act some supporting forms may have been removed from this thesis.

While these forms may be included in the document page count, their removal does not represent any loss of content from the thesis.

AVIS:

L'auteur a accordé une licence non exclusive permettant à la Bibliothèque et Archives Canada de reproduire, publier, archiver, sauvegarder, conserver, transmettre au public par télécommunication ou par l'Internet, prêter, distribuer et vendre des thèses partout dans le monde, à des fins commerciales ou autres, sur support microforme, papier, électronique et/ou autres formats.

L'auteur conserve la propriété du droit d'auteur et des droits moraux qui protège cette thèse. Ni la thèse ni des extraits substantiels de celle-ci ne doivent être imprimés ou autrement reproduits sans son autorisation.

Conformément à la loi canadienne sur la protection de la vie privée, quelques formulaires secondaires ont été enlevés de cette thèse.

Bien que ces formulaires aient inclus dans la pagination, il n'y aura aucun contenu manquant.

Canada

ADVANCEMENT OF SHOCK-WAVE INDUCED SPRAYING PROCESS THROUGH
THE STUDY OF GAS AND PARTICLE FLOW FIELDS

by
Mo Karimi

APPROVED BY:

Dr. André G. McDonald
Mechanical Engineering, University of
Alberta

Dr. N. Zamani
Mechanical, Automotive and Material
Engineering

Dr. J. Villafuerte
Industrial Advisor, CenterLine
(Windsor) Limited

Dr. B. Jodoin, Co-Advisor
Mechanical Engineering, University of
Ottawa

Dr. R. Carriveau
Civil and Environmental Engineering

Dr. G. Rankin, Co-Advisor
Mechanical, Automotive and Material
Engineering

Dr. R. Barron
Mechanical, Automotive and Materials
Engineering

Dr. K. Tepe, Chair of Defense
Electrical and Computer Engineering

December 2012

Declaration of Co-Authorship / Previous Publication

I. Co-Authorship Declaration

I hereby declare that this dissertation incorporates the outcome of research undertaken under the co-supervision of Dr. G. Rankin, University of Windsor, and Dr. B. Jodoin, University of Ottawa, with Dr. J. Villafuerte, CenterLine (Windsor) Limited as Industrial Advisor. In all cases, I certify that I am the principal author and have had a major role in the preparation and writing of the manuscripts.

I am aware of the University of Windsor's Senate Policy on Authorship and I certify that I have properly acknowledged the contribution of other researchers to my dissertation.

I certify that, with the above qualifications, this dissertation, and the research to which it refers, is the product of my own work.

II. Declaration of Previous Publication

This dissertation includes two original papers that have been previously published in peer-reviewed journals as indicated below:

Publication Title / Full Citation	Co-authors' Nature and Extent of Contribution	Publication, Copyright Status
M. Karimi, B. Jodoin and G. Rankin, Shockwave Induced Spraying Process: Effect of Parameters on Coating Performance. International Thermal Spray Conference and Exposition, Seoul, South Korea (2013).	Dr. Jodoin and Dr. Rankin are providing supervisory and advisory role in preparing the manuscript.	Abstract and presentation: abstract accepted, manuscript underway. Authors still hold copyright.
M. Karimi, B. Jodoin and G. Rankin, Influence of Spray Variables on the Performance of the Shockwave Induced Spraying Process. North American Cold Spray Conference, Seattle, WA, USA (2013).	Dr. Jodoin and Dr. Rankin provided supervisory and advisory role in preparing the manuscript.	Abstract and presentation: abstract accepted. Authors hold copyright.

<p>M. Karimi, G. W. Rankin and B. Jodoin, Shock-wave induced spraying: Gas and particle flow and coating analysis. Surface and Coatings Technology (2012), 207, 435-442.</p>	<p>Dr. Jodoin and Dr. Rankin provided supervisory and advisory role in preparing the manuscript. Moreover, Dr. Jodoin provided a major portion of the Introduction, where a survey of the technology is presented. Although this formed the structure of Section 1.1 ('Technology Background') of this dissertation, it has been significantly expanded by me.</p>	<p>Journal article: published. Generic permission included in Appendix A.</p>
<p>M. Karimi, B. Jodoin and G.W. Rankin, Shockwave Induced Spraying Process: Prediction of Coating Formation in Shockwave-Induced Spray Process Through Modeling. International Thermal Spray Conference and Exposition, Houston, TX, USA (2012).</p>	<p>Dr. Jodoin and Dr. Rankin are providing supervisory and advisory role in preparing the manuscript.</p>	<p>Manuscript and presentation. Generic permission included in Appendix A.</p>

<p>M. Karimi, B. Jodoin and G. Rankin, Shockwave Induced Spraying: Modeling and Physics of a New Spray Process. Journal of Thermal Spray Technology (2011), 20, 866-881.</p>	<p>Dr. Jodoin and Dr. Rankin provided supervisory and advisory role in preparing the manuscript.</p>	<p>Journal article: published. Generic permission included in Appendix A.</p>
<p>M. Karimi, B. Jodoin, G.W. Rankin. Shock-wave Induced Spraying: Modeling and Analysis. North American Cold Spray Conference, Windsor, ON, Canada (2011).</p>	<p>Dr. Jodoin and Dr. Rankin provided supervisory and advisory role in preparing the manuscript.</p>	<p>Abstract, presentation and poster. Authors hold copyright.</p>
<p>M. Karimi, B. Jodoin and G.W. Rankin. Shock-wave Induced Spraying: Modeling and Physics of a New Spray Process. International Thermal Spray Conference and Exposition, Hamburg, Germany (2011).</p>	<p>Dr. Jodoin and Dr. Rankin are providing supervisory and advisory role in preparing the manuscript.</p>	<p>Manuscript and poster. Generic permission included in Appendix A.</p>

<p>M. Karimi, G.W. Rankin and B. Jodoin. Simulation and Post-processing of Transient Compressible Flow in a Long Tube. CFD Society of Canada Conference, Montreal, QC, Canada (2011).</p>	<p>Dr. Jodoin and Dr. Rankin are providing supervisory and advisory role in preparing the manuscript.</p>	<p>Manuscript and presentation. Authors hold copyright.</p>
<p>M. Karimi, B. Jodoin, G.W. Rankin. Shock-wave Induced Spraying: Modeling and Analysis. North American Cold Spray Conference, Montreal, QC, Canada (2010).</p>	<p>Dr. Jodoin and Dr. Rankin provided supervisory and advisory role in preparing the manuscript.</p>	<p>Abstract and poster. Authors hold copyright.</p>

I certify that I have obtained written permission from the copyright holders to include the above published materials in my dissertation. An image of these written permissions is included in Appendix A. I certify that the above material describes work completed during my registration as a graduate student at the University of Windsor.

I declare that to the best of my knowledge, my dissertation does not infringe upon anyone's copyright nor violate any proprietary rights and that any ideas, techniques, quotations, or any other material from the work of other people included in my

dissertation, published or otherwise, are fully acknowledged in accordance with standard referencing practices. Furthermore, to the extent that I have included copyrighted material that surpasses the bounds of fair dealing within the meaning of the Canada Copyright Act, I certify that I have obtained a written permission from the copyright owners to include such material(s) in my dissertation.

I declare that this is a true copy of my dissertation, including any final revisions, as approved by my defense committee and the Office of Graduate Studies, and that this dissertation has not been submitted for a higher degree to any other university or institution.

Abstract

This research advances the knowledge of the working principles of the Shock-wave Induced Spraying Process (SISP), a thermal spray material deposition technique. Pulses created by a fast acting valve pass through a heated line increasing energy content and interacting with metered batches of heated or non-heated powder introduced into the line. The powder is accelerated to high velocities before bonding to the substrate upon impact.

Advantages over other cold spray processes include cost savings and a more effective transfer of thermal energy to the powder. The shock-wave occurring near the substrate in other cold spray processes is avoided.

The SISP flow field is resolved by using a computational model. The two-dimensional model accounts for the valve, gas heater, a tapered nozzle at the tip of the device, and pre-heating of the powder. It is implemented with a commercial computational fluid dynamics code. Comparisons are made with one-dimensional predictions, and measurements of pressure and temperature. Particle flow predictions are validated using particle velocity and adhesion measurements.

A flow region of both high temperature and velocity gas, favorable to material deposition, forms which is not present in comparable steady-state cold spray processes. Increasing gas pressure increases the gas speed, while increasing temperature increases

speed and temperature of this region. Using helium results in greater energy levels but for shorter periods of time. This indicates the need for a powder feeder which places particles in the flow at correct instants and durations of time.

The effects of particle flow parameters on system performance are examined. It is found that the device must be operated at very high main heater and powder heater temperatures: 900 °C and 700 °C respectively to achieve a coating with stainless steel using nitrogen as the driving gas. It is also shown that a heater length range of 0.9 m to 1.4 m results in the greatest likelihood of achieving a coating. A higher spray frequency yields more uniform coating at the expense of performance. Powder heating becomes effective at temperatures above 300 °C, especially with aluminum compared to copper and stainless steel.

Dedication

To my family.

Acknowledgements

I hereby extend my warm thanks to Dr. Rankin and Dr. Jodoin for their continual guidance, support and advice during the period of this project. This was essential to the completion of this work. My sincere thanks also goes to Dr. Villafuerte who was my industrial advisor and provided invaluable input.

I also acknowledge support and advice from Dr. Barron. He provided technical guidance through his two courses in computational fluid dynamics as well as his coaching of a course project that created the basis for this study. More importantly, he has set a golden standard in professionalism and passion to his work and his students, which has been a source of aspiration to me.

I also acknowledge motivation and encouragement that I received from Dr. Zamani when making important professional decisions. Additionally, Eric Michaud and Doug Matton of CenterLine Windsor Limited provided valuable technical input and support in the form of equipment when needed. My thanks go to Michael Beneteau of CenterLine Windsor Limited for allowing me the flexibility to pursue my academic aspiration while still staying affiliated with the company, affording me a unique opportunity to enhance my abilities in both academia and industry, and helping me meet my family responsibilities.

The research presented here is funded by NSERC through a few different grants, namely, a ‘Alexander Graham Bell’ scholarship held by me at University of Windsor, NSERC Discovery grants held by Dr. Rankin and Dr. Jodoin, as well as a NSERC - Idea to Innovation (I2I) grant held by Dr. Jodoin. The authors gratefully acknowledge this support.

Last but not least, I give my best regards and heartfelt thanks to my wife Hoda. She has been patient with me while I was working long hours each day, and encouraging me to pursue my wildest dreams fearlessly.

Table of Contents

Declaration of Co-Authorship / Previous Publication	iii
Abstract	ix
Dedication	xi
Acknowledgements	xii
List of Tables	xviii
List of Figures	xix
Nomenclature: List of Symbols and Subscripts	xxv
Chapter 1. Introduction	1
1.1 Technology Background	1
1.2 Shock-wave Induced Spray Process	10
1.3 Bonding Mechanism in Kinetic Spraying	12
Chapter 2. Literature Review and Objectives	15
2.1 Previous Studies	15
2.2 Overview of Flow Physics	19
2.3 Objectives	24
2.4 Contents of Dissertation	25
Chapter 3. Numerical Methodology	27

3.1 Computational Gas Dynamic Model.....	27
3.1.1 Problem Statement.....	28
3.1.2 Assumptions	28
3.1.3 Governing Equations	33
3.1.4 Grid Considerations.....	35
3.1.5 Boundary Conditions.....	39
3.1.6 Initial Conditions	40
3.2 Discrete Phase Model.....	40
3.3 Solver Settings.....	43
Chapter 4. Numerical Experiments, Verification and Validation	47
4.1 Stage One: Generic Gas Flow	47
4.1.1 Model Conditions	48
4.1.2 Model Verification	50
4.1.3 Presentation of Results	55
4.1.4 Model Validation.....	58
4.2 Stage Two: Representative Gas Flow	62
4.2.1 Model Conditions	63
4.2.2 Model Validation.....	64
4.3 Stage Three: Discrete Phase.....	67
4.3.1 Model Conditions	68

4.3.2 Model Validations	68
Chapter 5. Results and Discussion	71
5.1 Stage One: Gas Phase - Simplified Model	71
5.1.1 Effect of Gas Supply Pressure and Temperature	72
5.1.2 Effect of Gas Type.....	80
5.1.3 Summary of Stage One: Gas Phase - Simplified Model	85
5.2 Stage Two: Gas Phase - Representative Geometry	87
5.2.1 Results of Stage Two: Gas Phase - Representative Geometry	88
5.2.2 Summary of Stage Two: Gas Phase - Representative Geometry	92
5.3 Stage Three: Discrete Phase	92
5.3.1 Presentation of Results	93
5.3.2 Experimental Work and Comparison with Discrete Phase Predictions	97
5.3.3 Summary of Stage Three: Discrete Phase Model in Representative Geometry	100
Chapter 6. Case Studies	102
6.1 Coating with Stainless Steel Powder.....	102
6.2 Effect of Heater Length.....	103
6.3 Effect of Process Frequency.....	108
6.4 Effect of Powder Heating Temperature	110
6.5 Effect of Powder Loading	113

Chapter 7.	Conclusion	116
Chapter 8.	Recommendation for Future Work	121
References.....		123
Appendix A	Written Permission from the Copyright Holders	130
Appendix B	Profile for Valve Motion and Heater Temperature	138
Appendix C	User-Defined Function to Model Heat Transfer under High-Mach- Number Gas-Particle Relative Flow	144
Appendix D	Effect of Radial Location of Particle Injection	147
Appendix E	Journal File for Extracting Data on the Centerline	153
Appendix F	MATLAB Codes to Generate x-t Contours of Flow Variables	155
Appendix G	MATLAB Codes to Generate Time History Plots of Flow Variables ..	159
Appendix H	MATLAB Code to Generate x-t Contours and Extract Time History Data of Particle Variables.....	164
Vita Auctoris.....		169

List of Tables

Table 1: Different categories of thermal spraying and their main properties.	10
Table 2: Geometrical features of the device modeled.	47
Table 3: Simulation conditions considered in the Stage One of the study.	49
Table 4: Combinations of interest for simulation conditions for this study.	50
Table 5: Summary of various grids used in the grid sensitivity study.	51
Table 6: Comparison of simulation results with one-dimensional solution.	59
Table 7: Parameters used to calculate critical velocity.	95
Table 8: Maximum value of V/V_{cr} and time per cycle during which this value falls between 1.0 and 2.0, in comparison with experimental values of deposition efficiency, for various particle materials and sizes.	98
Table 9: Minimum and maximum values of V/V_{cr} , and the percentage of a cycle during which this value falls above unity, as a function of heater length, for particles of aluminum, copper and stainless steel.	106

List of Figures

Figure 1: Schematic of the plasma spray process (top) and a plasma spray torch (bottom) during a spray process - courtesy of Gordon England [8].	3
Figure 2: Schematic of the arc spray process (top) and an arc spray device (bottom) during a spray process - courtesy of Gordon England [8].	4
Figure 3: Schematic of the HVOF process (top) and a HVOF device (bottom) during a spray process - courtesy of Gordon England [8].	5
Figure 4: A schematic diagram of the cold spray process - courtesy of Gordon England [8].	7
Figure 5: Schematic of the Shock-wave Induced Spraying Process Device	11
Figure 6: Beta version of the first SISP device, named Waverider™. Picture courtesy of SST, a division of CenterLine (Windsor) Limited [48].	17
Figure 7: Consecutive images depicting the intended working principle in the Shock-wave Induced Spraying Process.	20
Figure 8: Schematic of the SISP spray device through one pulse spray cycle. Reproduced with permission [39].	21
Figure 9: Schematic of the one-dimensional model.	22
Figure 10: Theoretical instantaneous values of gas speed and temperature just prior to the departure of the shock-wave from the spray device. Reproduced with permission [39]. ..	23
Figure 11: A generic schematic of the flow region.	28
Figure 12: Picture and a CAD representation of the rotary-style valve used in the SISP device	30

Figure 13: Left: a heating tube (in coiled form) during a heating process with gas flow, Right: comparison of measured temperature values along the heater tube with a linear approximation proposed for use as boundary condition in the simulation.	32
Figure 14: Mesh, near the valve ball (left) and near the tube exit and substrate (right). ..	35
Figure 15: Adapted grid superimposed on contours of static pressure (Pa) at $t = 0.2$ m. A 14-mm-long portion of the tube, 110 mm downstream of valve.	37
Figure 16: Dynamic meshing - layering method	38
Figure 17: Mesh near the valve ball (left), zoomed in with the valve closed (center) and in the process of opening (right).	39
Figure 18: Schematic of the flow region used at Stage One.	48
Figure 19: Values of static temperature and axial velocity along the centerline of the device at two time instants using grids with 3, 5 and 7 cells along the radius	52
Figure 20: Values of static temperature (top) and axial velocity (bottom) at three solution times using three different time step values.	54
Figure 21: Values of velocity magnitude (left) and static temperature (right) along the spray device centerline at the beginning of the first four pulses.	55
Figure 22: Sequential contours of static temperature at 0 ms to 4 ms. Air, 2 MPa, room temperature.	56
Figure 23: Contours of static temperature (K) in space-time domain – Air, 2 MPa, no heat.	57
Figure 24: Comparison of density values (in kg/m^3) obtained from current CFD simulation (left) with validated one-dimensional model (right). Air, 2 MPa supply pressure, no heat.	60

Figure 25: Schematic of the flow region used at Stage Two.	63
Figure 26: Comparison of time-history of wall pressure at two locations along the spray tube between the experiment and the simulation: 1- immediately after the valve, 2- at the powder injection location.....	65
Figure 27: Effect of stroke length on prediction of pressure, and comparison with experimentally measured pressure values.....	66
Figure 28: Experimentally measured temperature values overlaid on predictions from the simulation.....	67
Figure 29: Typical location of particle injection site with reference to the valve and nozzle exit.	68
Figure 30: DPV-2000 particle analysis device by Tecnar Inc.	69
Figure 31: Comparison of measured and calculated particle speed at the exit of the SISP device for aluminum (top), copper (center) and stainless steel 316 (bottom) particles....	70
Figure 32: Effect of supply pressure and temperature on static pressure (Pa). Supply temperature and pressure values of ambient and 1 MPa (left), ambient and 2 MPa (middle) and 300 °C and 2 MPa (right).	73
Figure 33: Effect of supply pressure and temperature on Mach number. Supply temperature and pressure values of ambient and 1 MPa (left), ambient and 2 MPa (middle) and 300 °C and 2 MPa (right).	73
Figure 34: Effect of supply pressure (top) and temperature (bottom) on gas speed and Mach number in zone 2, with the assumption of fully-recovered temperature and no temperature recovery in the tube after the passage of the shock-wave.....	74

Figure 35: Effect of supply pressure and temperature on axial velocity (m/s). Supply temperature and pressure values of ambient and 1 MPa (left), ambient and 2 MPa (middle) and 300 °C and 2 MPa (right).	76
Figure 36: Effect of supply pressure and temperature on static temperature (K). Supply temperature and pressure values of ambient and 1 MPa (left), ambient and 2 MPa (middle) and 300 °C and 2 MPa (right).	78
Figure 37: Effect of supply pressure and temperature on total temperature (K). Supply temperature and pressure values of ambient and 1 MPa (left), ambient and 2 MPa (middle) and 300 °C and 2 MPa (right).	80
Figure 38: Effect of gas type on static pressure (Pa). Gas type of air (left) and helium (right).	81
Figure 39: Effect of gas type on axial velocity (m/s). Gas type of air (left) and helium (right).	82
Figure 40: Effect of gas type on Mach number. Gas type of air (left) and helium (right).	83
Figure 41: Effect of gas type on static temperature (K). Gas type of air (left) and helium (right).	84
Figure 42: Effect of gas type on total temperature (K). Gas type of air (left) and helium (right).	85
Figure 43: Contours of (a) pressure (Pa), (b) axial velocity (m/s), (c) temperature (K) and (d) total temperature (K) for a typical spray device.	89
Figure 44: Contours of (a) pressure (Pa), (b) axial velocity (m/s), (c) temperature (K) and (d) total temperature (K) from Stage Two (left) and Stage One (right).	90

Figure 45: Contours of particle characteristics upon impacting on the substrate for 20-micron stainless steel 316 particles initiated at various locations and times in the domain: (a) speed (m/s), (b) temperature (K), (c) critical velocity (m/s) and (d) critical velocity ratio V/V_{cr} .	94
Figure 46: Calculated values of V/V_{cr} for particles of various sizes and materials injected at typical location and various times.	96
Figure 47: Effect of increased heater temperature setting and powder preheating on the fate of powder particles upon reaching the substrate.	103
Figure 48: Values of V/V_{cr} as a function of injection time for aluminum (top), copper (middle) and stainless steel (bottom) powder particles.	105
Figure 49: Effect of frequency on values of V/V_{cr} for aluminum (top), copper (middle) and stainless steel (bottom) powder feedstock.	109
Figure 50: Effect of powder preheat temperature setting on the value of V/V_{cr} for particles of (top) aluminum, (middle) copper, and (bottom) stainless steel.	111
Figure 51: Effect of powder preheat temperature setting on the value of V/V_{cr} for particles of (top) aluminum, (middle) copper, and (bottom) stainless steel.	112
Figure 52: Effect of powder loading on the value of V/V_{cr} for particles of (top) aluminum, (middle) copper, and (bottom) stainless steel.	115
Figure D1: Speed (left) and temperature (right) of 20-micron aluminum particles upon impacting on substrate, initiated at 0.0R (top), 0.5R (center), and 0.8R (bottom).	147
Figure D2: Speed (left) and temperature (right) of 20-micron copper particles upon impacting on substrate, initiated at 0.0R (top), 0.5R (center), and 0.8R (bottom).	148

Figure D3: Speed (left) and temperature (right) of 20-micron stainless steel particles upon impacting on substrate, initiated at 0.0R (top), 0.5R (center), and 0.8R (bottom) 149

Figure D4: V/V_{cr} values for 20-micron aluminum particles upon impacting on substrate, initiated at 0.0R (top), 0.5R (middle), and 0.8R (bottom) 150

Figure D5: V/V_{cr} values for 20-micron copper particles upon impacting on substrate, initiated at 0.0R (top), 0.5R (middle), and 0.8R (bottom) 151

Figure D6: V/V_{cr} values for 20-micron stainless steel particles upon impacting on substrate, initiated at 0.0R (top), 0.5R (middle), and 0.8R (bottom) 152

Nomenclature: List of Symbols and Subscripts

Symbols

Bi	Biot Number
c	Speed of Sound
C_D	Drag Coefficient
c_p	Specific Heat
d	Diameter
E	Energy
F_1	Empirical Factor 1 for Critical Velocity Correlation
F_2	Empirical Factor 2 for Critical Velocity Correlation
h	Cell Height
h	Heat Transfer Coefficient
k	Thermal Conductivity
M_p	Particle Mach Number
M_w	Molecular Weight of the Gas
Nu	Nusselt Number
p	Pressure
Pr	Prandtl Number
R	Universal Gas Constant
R	Radius of nozzle tube
r	Radial Position
Re_p	Particle Reynolds Number
T	Temperature
t	Time
u	Velocity Component
\vec{u}	Velocity Vector
V	Gas Speed in One-dimensional Model
V	Particle Velocity

x	Axial Position
α_c	Collapse Factor
α_s	Split Factor
μ	Flow Viscosity
ρ	Gas Density
$\vec{\tau}$	Stress Tensor
γ	Gas Constant

Subscripts

1	Relating to zone 1
2	Relating to zone 2
3	Relating to zone 3
4	Relating to zone 4
cr	Critical Value
g	Relating to Gas
i	Relating to Impact
M	Relating to Melting
p	Relating to Particle
R	Reference Value
r	Radial Component
x	Axial Component

Chapter 1. Introduction

In this chapter the background of the technology is first established. This includes a review of all categories of thermal spray processes, with a view of the balance between kinetic and thermal energy. This discussion then leads to the introduction of processes with greater influence of kinetic energy, ending with the introduction of Shock-wave Induced Spraying Process, that is the subject of this dissertation.

1.1 Technology Background

Thermal spray processes are widely used in many industrial sectors to enhance surface properties by depositing melted droplets or semi-molten particles on a substrate [1]. These droplets, or semi-molten particles, will then solidify upon landing on the substrate in order to form a coating. A useful analogy for the process can be precipitation landing on the pavement in a very cold day. Under certain conditions the pavement can be at slightly below freezing temperature while precipitation can be slightly above, in a molten or semi-molten state. Under this scenario the precipitation will quickly solidify upon landing on the pavement and gradually form a solid layer of ice coating the pavement.

In order to heat the deposited material to at or near its melting temperature, various energy sources can be used. As such, thermal spray processes are typically classified into four groups based on the type of energy source used to heat the material

and achieve deposition: plasma spraying, wire arc spraying, combustion spraying and kinetic spraying.

Plasma spraying relies on the thermal energy of a high-temperature plasma jet generated by running a direct electrical current between a cathode and an annular anode nozzle [1-3]. The plasma jet typically exits the nozzle with temperatures ranging between 5000 °C and 20000 °C, depending on the gas mixtures and power settings used [2]. The feedstock particles are then melted, outside the nozzle and in the plasma jet, and projected at velocities ranging from 80 m/s to 300 m/s onto the substrate where they rapidly solidify and form a coating. This solidification process occurs so rapidly that it frequently leads to amorphous microstructures.

A schematic of the plasma spraying process, as well as a plasma spray torch during a spray process, is shown in Figure 1. Due to the very high temperatures achieved in the process, a wide range of feedstock materials can be used in this process, ranging from low to high melting temperature metals to ceramics [4, 5]. In recent years work on improving equipment from a performance [6] and control [7] stand-point continues. Although the high temperature achieved in the process allows for a wide range of spray materials, it has many detrimental effects. The substrate undergoes severe heating, has unfavorable residual stresses, and the feedstock material undergoes phase transformation where its original structure usually cannot be completely retained.

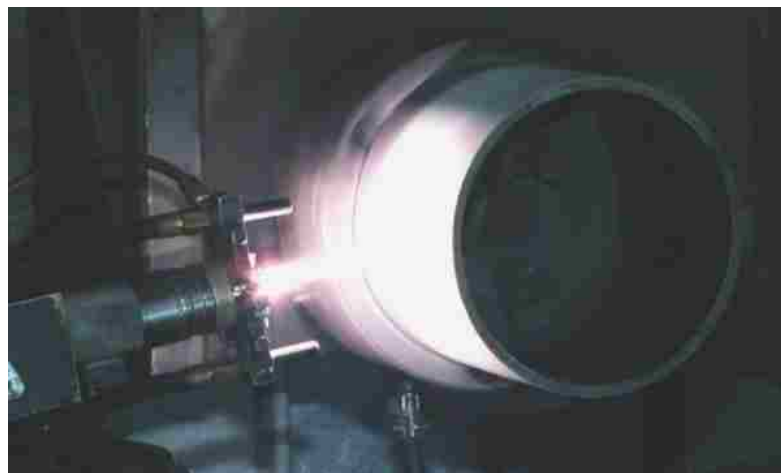
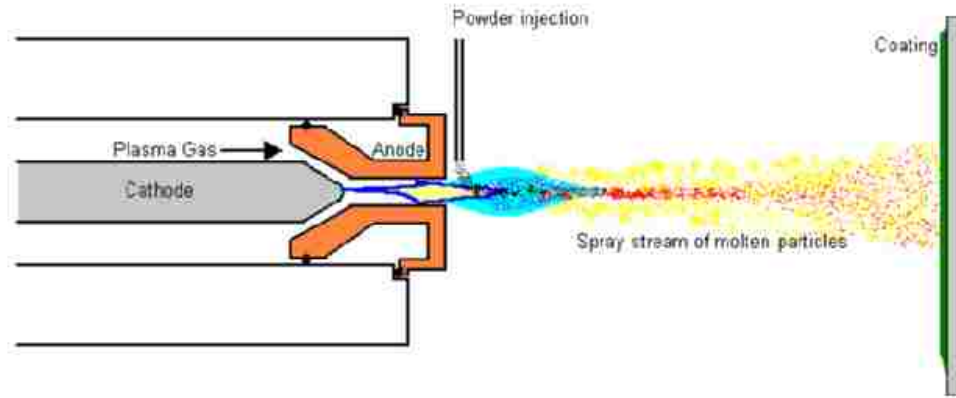


Figure 1: Schematic of the plasma spray process (top) and a plasma spray torch (bottom) during a spray process - courtesy of Gordon England [8].

In the wire arc spraying process (also referred to as twin-wire arc spray) a pair of electrically conductive wires are melted by an electric arc [9, 10]. The molten material is then atomised by compressed air and propelled towards the substrate surface [11, 12]. The molten particles impacting on the substrate rapidly solidify to form a coating.

A schematic of the wire arc spraying process, as well as a working device, are shown in Figure 2. The equipment used in this process is rather simple in construction [8], as the feedstock is in the form of wire and powder handling provisions are not required. Additionally, the wire arc also acts as the source of heat eliminating the

need for an additional heat source. This has found technology applications in various fields, from metallic membranes [13] to internal combustion engines [14]. The major limitation of the process is that its feedstock can only be selected from electrically conductive materials [8].

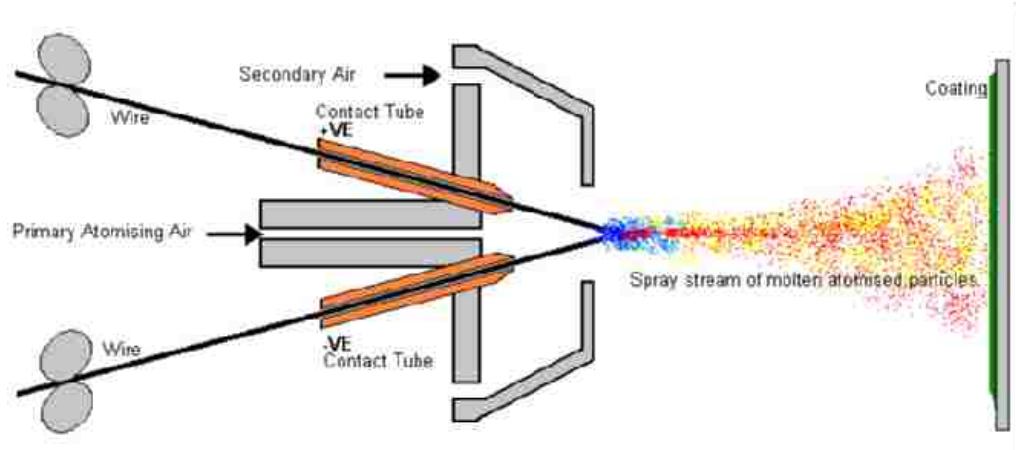


Figure 2: Schematic of the arc spray process (top) and an arc spray device (bottom) during a spray process - courtesy of Gordon England [8].

High Velocity Oxygen-Fuel (HVOF) [15] and High Velocity Air-Fuel (HVOF) [16] technologies are two variations of the combustion thermal spray process [1]. A schematic of a typical combustion spray device, and a HVOF device during a spray process, are shown in Figure 3. These processes rely on the chemical

reaction between a fuel and oxygen or air as a source of thermal energy for coating deposition. Typically, kerosene, acetylene, propylene or hydrogen can be used for fuel [8]. The resulting flame is then fed into a converging-diverging nozzle where the gases are accelerated at supersonic velocities, leading to jet temperatures of approximately 3000 °C and velocity range from 1525 m/s to 1825 m/s. Upon exposure to the high temperature and high velocity flame, the feedstock particles experience a significant increase in thermal and kinetic energy, resulting in partially melted and/or softened high-velocity particles. Coating formation is therefore attributed to the combined effect of splat formation and plastic deformation of the particles upon impact with the substrate [17].

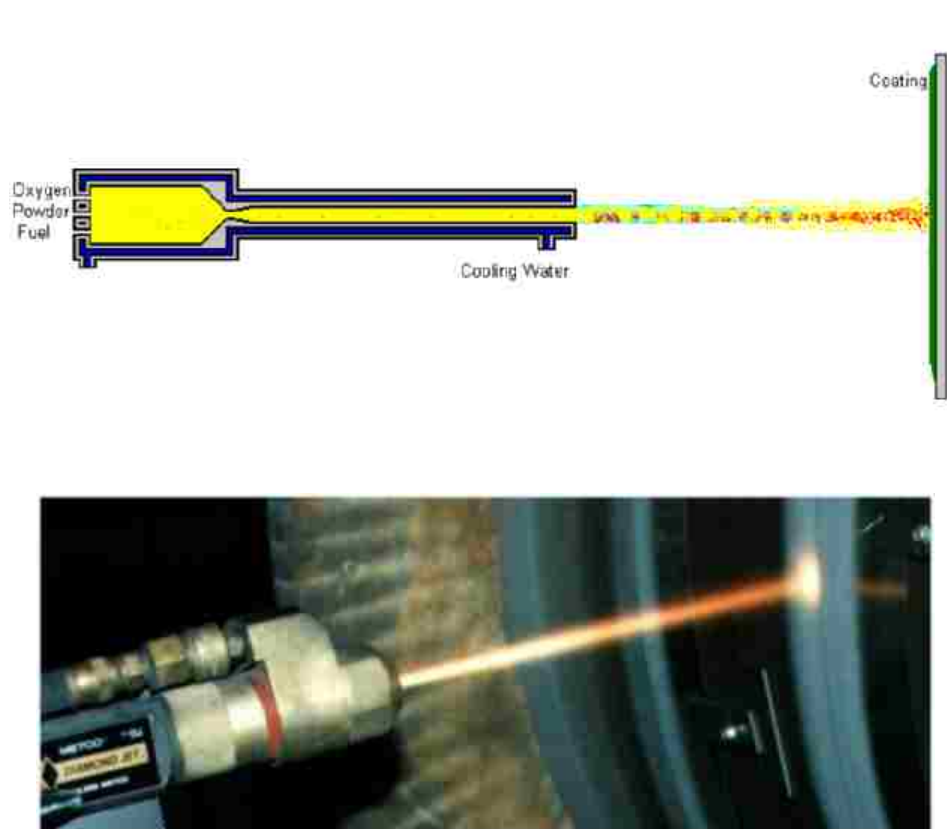


Figure 3: Schematic of the HVOF process (top) and a HVOF device (bottom) during a spray process - courtesy of Gordon England [8].

The main advantage of combustion spray processes lies in the very high content of energy available to the process. A combination of combustion gases at a very high temperature and a high-speed gas flow can allow successful deposition of many hard [18] and high-melting-point [19] metals. In addition, coatings of many cermets and ceramics are also possible using this technology [20, 21].

Another kind of thermal spray process exists, called the detonation spray process, which relies on an interrupted gas flow. In this process a precisely measured quantity of a combustion mixture is fed into a straight barrel along with a pulse of powder. The explosive mixture is ignited using a spark plug. The resulting detonation wave travels down the barrel while accelerating and heating the powder. The powder particle exits at a velocity as high as 700 m/s and at a temperature near or above its melting point [22]. The coatings generated by the process are shown to demonstrate excellent density, bond characteristics and wear properties [23].

These thermal spray techniques offer many possibilities for creating coatings of a wide range of materials. However, they also have limitations and disadvantages [1]. These stem from the very high temperatures involved with these processes. These high temperatures have many detrimental effects on the feedstock material, the substrate, and the final coating products. These include oxidation or other chemical reactions, possible melting of the substrate, changes in the microstructure of the feedstock in flight or the substrate, as well as adverse residual stresses in the final product.

Cold spray (also referred to as Cold Gas Dynamic Spraying - CGDS) is a subcategory of thermal spray processes that offers an alternative to other thermal spraying processes by operating at significantly lower temperatures. In this process kinetic energy is used to manufacture coatings: solid powder particles are accelerated at high velocities (typically 300 m/s to 1200 m/s) in a supersonic inert gas flow in order to be projected onto the substrate [24].

A schematic of the cold spray process is shown in Figure 4. The supersonic gas flow is generated by passing the main carrier gas through a converging-diverging nozzle. The carrying gas is usually heated prior to being introduced to the nozzle, however this heating action is usually far less than that required to melt the powder particles. Although cold spraying relies mainly on kinetic energy for the bonding to occur, some heating is often required in order to enable this bonding.

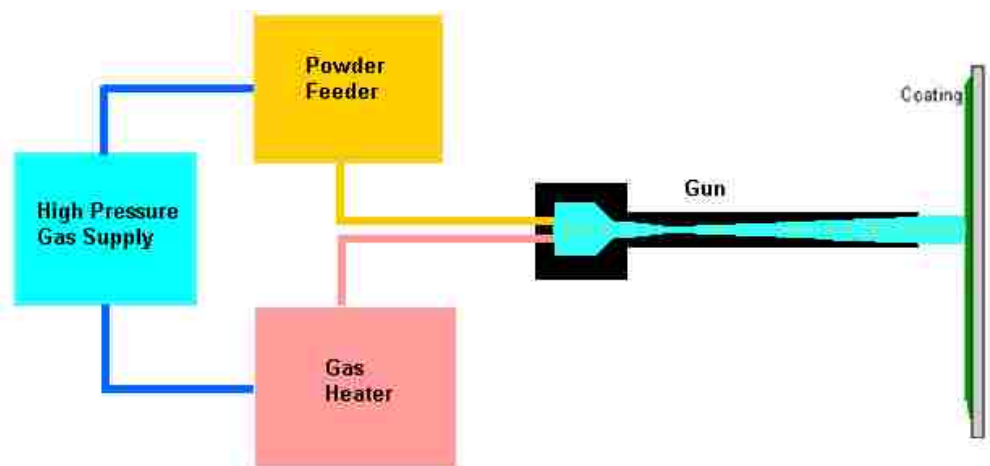


Figure 4: A schematic diagram of the cold spray process - courtesy of Gordon England [8].

The main distinction between commercial cold spray systems lies in the location where the feedstock particle stream is added to the main gas flow: downstream or

upstream of the nozzle throat. Due to the pressure ranges at which they commonly operate, downstream and upstream injection types are commonly referred to as low-pressure [25, 26] (for downstream injection) and high-pressure [27] cold spray systems, respectively.

Although this distinction has some impact on equipment design and manufacturing as well as their capabilities, all cold spray equipment remain principally the same. The gas dynamic principles of both processes are the same, and the adhesion and bonding mechanisms are also the same. Heating temperatures are generally far less than the melting point of the feedstock material, however it is found that localized melting, due to transformation of kinetic to thermal energy, is possible in some interface areas between the deformed particles and the substrate [28]. Bonding is shown to be associated with adiabatic shear instabilities that occur primarily in the perimeter of the impact zone [29].

Due to tight control over the process temperature in cold spray, negative implications of excessive heat present in other thermal spray processes can be largely avoided. Bonding is mostly a result of kinetic energy rather than thermal energy. While it is shown there is a gas-dynamic limit to how far this kinetic energy can increase [30], it is widely understood that this increase in energy comes at the cost of thermal energy reduction [31]. In steady-state transonic flow, under ideal assumptions, total energy of the gas is principally conserved as gas travels along the device, and any increase in the kinetic energy of the gas comes at the expense of thermal energy. This is an inherent

consequence of using a steady-state flow regime in a spraying device. In a transient flow regime, such as that of a shock tube [32-35], however, it is possible to have a region in the flow where increased speed *and* temperature can co-exist [36, 37]. The Shock-wave Induced Spray Process was developed as a spray process based on this shock tube flow characteristic [38, 39].

The only other thermal spray process that relies on an interrupted gas flow is the detonation spray process. In this process, a precisely measured quantity of a combustion mixture is fed into a straight barrel along with a pulse of powder. The explosive mixture is ignited using a spark plug. The resulting detonation wave travels down the barrel while accelerating and heating the powder. The powder particle exits at a velocity as high as 700 m/s and at a temperature near or above its melting point [22]. The coatings generated by the process are often compared with plasma-sprayed coatings and are shown to demonstrate excellent density, bond characteristics, and wear properties [23].

A summary of the categories of thermal spray processes is included in Table 1.

Table 1: Different categories of thermal spraying and their main properties.

Process Category	Source of Energy	Feedstock	Variations
Plasma Spraying	A plasma jet generated by an electrical current between a permanent cathode and anode	Powder, liquid suspension, or wire	Ar, H ₂ , N ₂ , He, air, vacuum
Wire Arc Spraying	Compressed gas and an electric arc between two consumable wires	Consumable wire that takes part in arc formation	
Combustion Spraying	Compressed gas and heat from combustion of fuel	Powder injected downstream of the torch	HVOF, HVOF
Kinetic Spraying	Compressed gas and thermal energy from an electric heater	Powder injected within the nozzle system	Downstream and upstream injection, steady or transient

1.2 Shock-wave Induced Spray Process

The Shock-wave Induced Spray Process (SISP) is a method of applying coatings onto a wide range of substrates [38-40]. It utilizes the kinetic and thermal energy induced by a moving shock-wave to accelerate and heat metallic powders. This process is a

variant of CGDS material deposition technique and utilizes a train of gas pulses in an unsteady interrupted flow.

The SISP process, illustrated in Figure 5, uses moving shock-waves at its core. Each shock-wave is created by the fast opening and closing of a valve; up to 30 Hz frequency is presently realisable. When the valve is rapidly opened, and subsequently closed shortly after, a shock-wave is generated that propagates into the spraying gun, accelerating and heating the powder present in the gun. Similar to the CGDS process, the particles then impact on the substrate and deform plastically to produce a coating [29]. SISP, however, differs from CGDS in that it is possible to achieve higher particle impact temperature due to the unsteady nature of the process.

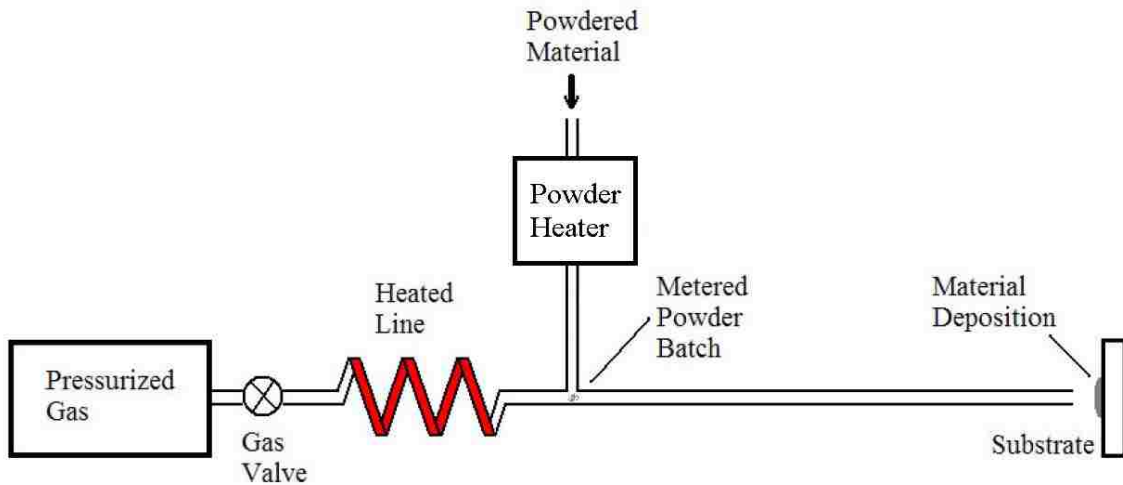


Figure 5: Schematic of the Shock-wave Induced Spraying Process Device

During each cycle, or pulse, a controlled feedstock powder quantity is placed into the tube. Correct timing of this action is of paramount importance to the process performance in that the powder must be present prior to the passage of the shock-wave. The process also involves an electrical heater allowing preheating of the gas.

1.3 Bonding Mechanism in Kinetic Spraying

In kinetic spraying, bonding occurs when the impact velocity of a particle exceeds a threshold velocity, commonly referred to as Critical Velocity, V_{cr} . This critical velocity depends on several factors, including the spray material and size, impact temperature, and surface and grain properties of particles and substrate surface.

Upon impact, the particle and the substrate both start to deform at the impact interface. Beyond critical velocity, this deformation results in such high strain rates that adiabatic shear instabilities occur, and in this region bonding occurs. This region is a peripheral slit around the impact circle when impact velocity is just above critical velocity, and it grows to the center of the impact circle as impact velocity further increases [29]. Although melting temperatures may be reached locally at the impact interface, melting is not regarded as the cause for bonding.

Bonding mechanisms for specific particle/substrate combinations have been examined by a number of researchers. Goldbaum et al [41] studied deposition of titanium particles on a titanium substrate. They conducted a 'splat' test, where the spray device is moved over the substrate at a fast enough speed to achieve single particle splats. Microstructural examination of the cross-section of these splats confirm the deformation of both the particles and the substrate. It was observed that bonding is more pronounced at the particle-substrate interface when higher deposition velocity is used.

Nakano et al [42] used an aluminum-nitride (AlN) substrate coated with a 100-nm layer of sputtered titanium and a 100-nm layer of sputtered copper. Copper particles of 5 micron size were then cold sprayed onto this substrate. An observation of the cross-section of the coated substrate confirms deformation of the particles as well as the deposited substrate. A wavy boundary was observed between the sputtered titanium and the sputtered copper, due to shear instabilities. No oxidation layer was observed between the cold-sprayed copper particles. This indicates that the plastic deformation of the copper particles lead to formation of a new surface on the boundary of the particles.

Irissou et al. [43] investigated the bonding behavior of pure aluminum, and blends of pure aluminum and aluminum-oxide (Al_2O_3) particles. A small and a large particle size distribution of aluminum, with mean particle diameters of 36.2 microns and 81.5 microns respectively, were considered. The aluminum oxide has a mean diameter of 25.5 microns. The large aluminum particles are sprayed under conditions that result in low particle deformation levels and high porosity levels. It is then observed that under the same spraying conditions, adding only 7% weight of aluminum oxide to the powder will result in a high level of deformation of the aluminum particles, and a significantly improved coating density. This observation suggests that coating properties can be improved by modifying the powder blend composition and using hard particle additives that can act as a catalyst in the bonding process.

Plastic deformation, shear instabilities and mechanical interlocking are found to be the dominant mechanism of bonding in cold spray, and under many conditions it is

found that no melting occurs at the bonding interface [28]. However, for the case of zinc coatings, it is found that spraying conditions can lead to local melting at the bonding interface. When this occurs, bonding is significantly enhanced due to the formation of a metallurgical bond.

Chapter 2. Literature Review and Objectives

The aim of this chapter is to first introduce the current state of the technology by summarizing the available literature. The present knowledge of the working principles of the process is presented. The objectives of the current work are then introduced. The literature pertaining to the background of technology, and its relation to other similar and competing technologies, is presented in Chapter 1.

2.1 Previous Studies

The SISP process was developed at the University of Ottawa Cold Spray Laboratory in 2005. Applications for a patent were filed shortly thereafter [38]. The first comprehensive description of this process was published in 2007 [39]. It involves analysis of the process through the use of a one-dimensional model based on shock tube theory. Experimental examination of the process was conducted using pressure data obtained from a high-frequency pressure transducer. Selected examples of coatings produced with the system are presented, illustrating the potential of the process to deposit various materials. It is shown that this process allows the feedstock particles to be accelerated to high impact velocities and intermediate temperatures (below melting temperature). This leads to a lower required critical velocity compared to traditional cold spraying.

In another study, an analysis of productivity and cost associated with the new process was presented [40] where a comparison is made of SISP with other thermal spray

processes in regard to commercial feasibility. It is explained that this technology presents more efficient management of thermal energy. As a result, high levels of performance can be achieved at lower capital and operational costs than possible with the high-pressure variation of CGDS. It is concluded that the process is most suitable for OEM production applications in which high productivity and low operating costs are paramount. This is in contrast with niche high-value technologies where operation costs are not of great significance.

A number of studies have also focused on various applications of the process. Some of these applications include WC-based coatings [44, 45], metallic coating of aerospace carbon/epoxy composites [46], SiC particulate reinforced Al-12Si alloy composite coatings [47], as well as various traditional materials sprayed by CGDS (Cu, Zn, Al) and new ones (amorphous Fe-based) [39]. The technology is presently commercialized to a beta-stage by the SST Division of CenterLine (Windsor) Limited [48] under the name WaveRider™ [49]. A picture of a beta-version unit of the device is shown in Figure 6.



Figure 6: Beta version of the first SISP device, named Waverider™. Picture courtesy of SST, a division of CenterLine (Windsor) Limited [48].

From an analytical standpoint, prior to the current dissertation the main source of knowledge available to explain the governing physics of the process was a one-dimensional model [39]. This approach is based on well-established compressible flow and shock-wave theory. Although the model is able to provide fundamental understanding of the process, many details of the flow features remain unresolved. This is due to many limitations of the model. For example, the model divides the flow field into a few sub-fields, called zones, and predicts a single value for flow properties for the entirety of each of these zones. This poses a limitation on spatial resolution considering there are only four of these zones in the solution scheme. Additionally, effects of turbulence and wall friction are ignored. Both of these effects are expected to be important considering the high flow speed as well as the very small size of the flow channel compared to its length.

The fundamental flow physics of SISP is closest in nature to that of detonation spraying process. The physics of the detonation spray process involves a greater level of complexity due to presence of combustion and chemical reaction. Therefore prior attempts at modeling of the detonation spray process can serve as a source of knowledge for the modeling of SISP.

A one-dimensional model of the detonation spray process is presented by Kadyrov [50]. This model describes the governing equations of gas and particle flows in a general one-dimensional transient domain. The model accounts for frictional effects as well as cooling of gas along the tube. However, radial variations of gas properties are neglected. Due to the inclusion of friction and viscosity, the equations do not have an analytical solution and therefore are solved numerically. These effects present an incremental improvement over a more basic one-dimensional analysis presented earlier, however still falls short of a two-dimensional CFD solution. The model, if applied to SISP, cannot account for the opening and closing of a valve. It does not model boundary layer effects, nor is it capable of representing the tapered tip of the SISP spray device.

Another study is reported where a two-dimensional analysis of the gas flow is considered [51]. Particle behavior in the gas flow is also modeled. However, in this work gas flow is considered inviscid. A high-resolution shock capturing numerical method, in conjunction with a Runge-Kutta scheme, are used for solving the system of partial differential equations. This work adds the second spatial dimension to the problem, however this comes at the expense of losing viscous effects. The work falls short of

presenting the physics of gas flow and concentrates mainly of the properties of particle behavior. A more enhanced version of this model has also been reported [52], that presents model validation and some explanation of flow physics. However, viscous and turbulence effects are still lacking.

2.2 Overview of Flow Physics

SISP relies on consecutive travelling shock-waves, rather than a steady gas flow, to carry the powder particles towards a substrate. A simplified sequence of images, to visualize the process progression, is shown in Figure 7. A metered batch of powder particles is placed in the spray barrel, which is subsequently carried by the flow induced by the passage of a travelling shock-wave towards a substrate. The batch of powder is shown in Figure 7 (a) and Figure 7 (b) to come from the powder feeder and enter in the device. In Figure 7 (c) and Figure 7 (d), the red line represents the shock-wave passing through the device. The shock-wave picks up, accelerates and directs the powder batch to the substrate in its wake, as illustrated in Figure 7 (e) and Figure 7 (f).

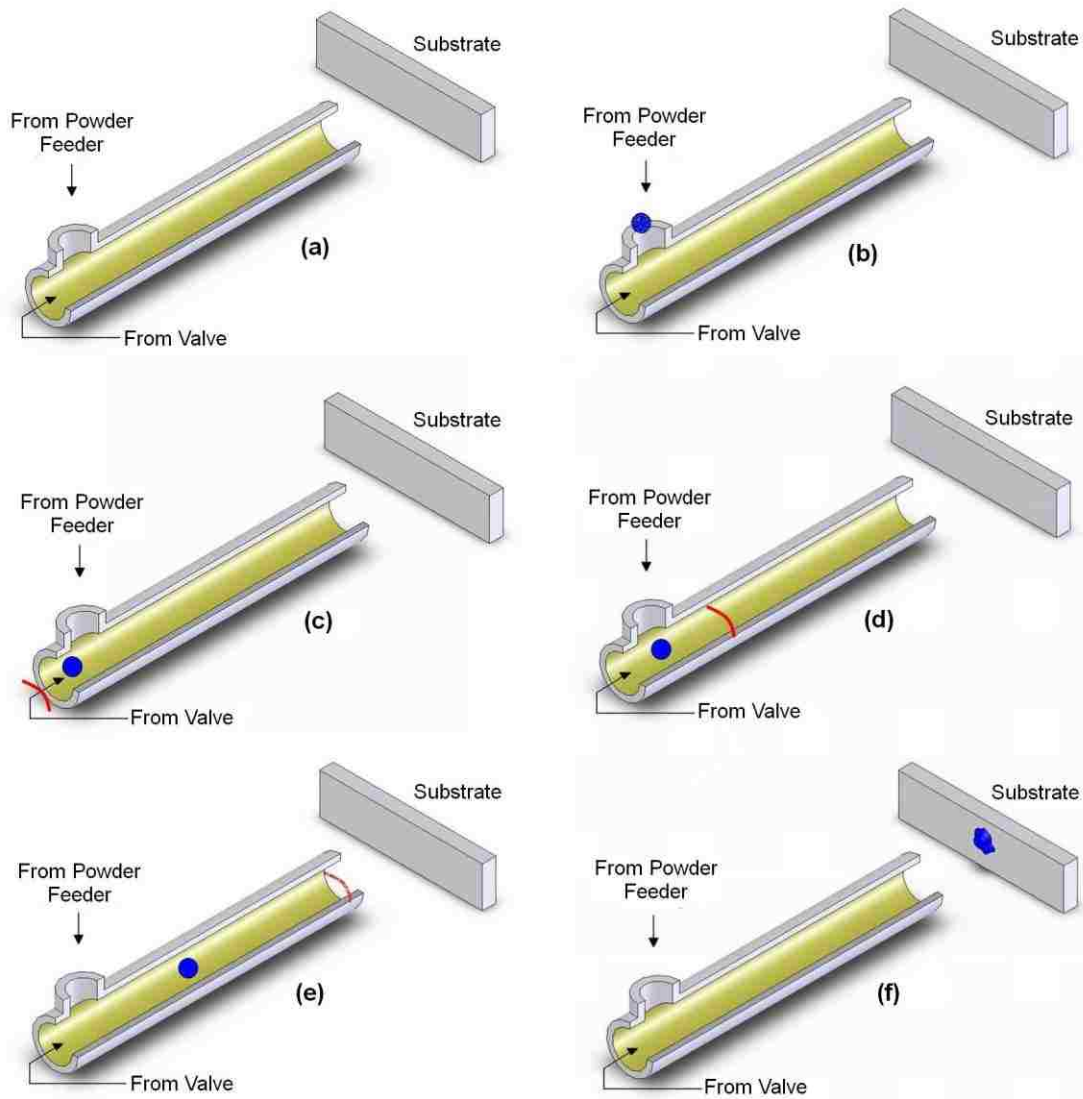


Figure 7: Consecutive images depicting the intended working principle in the Shock-wave Induced Spraying Process.

The travelling shock-wave is a result of the coalescence of compression waves downstream of the valve due to a large pressure difference between the pressure reservoir and the spray tube [53] (Figure 8 b). The valve closes shortly after this shock-wave is formed. The passage of this shock-wave creates a zone of high speed and intermediate temperature in the gas. This induced flow accelerates and heats the powder feedstock material towards a substrate (Figure 8 b' and Figure 8 b'') in order to form a coating,

similar to the cold spray process. The cycle is repeated after the complete passage of a shock-wave when the pressure inside the gun drops and reaches the ambient atmospheric pressure.

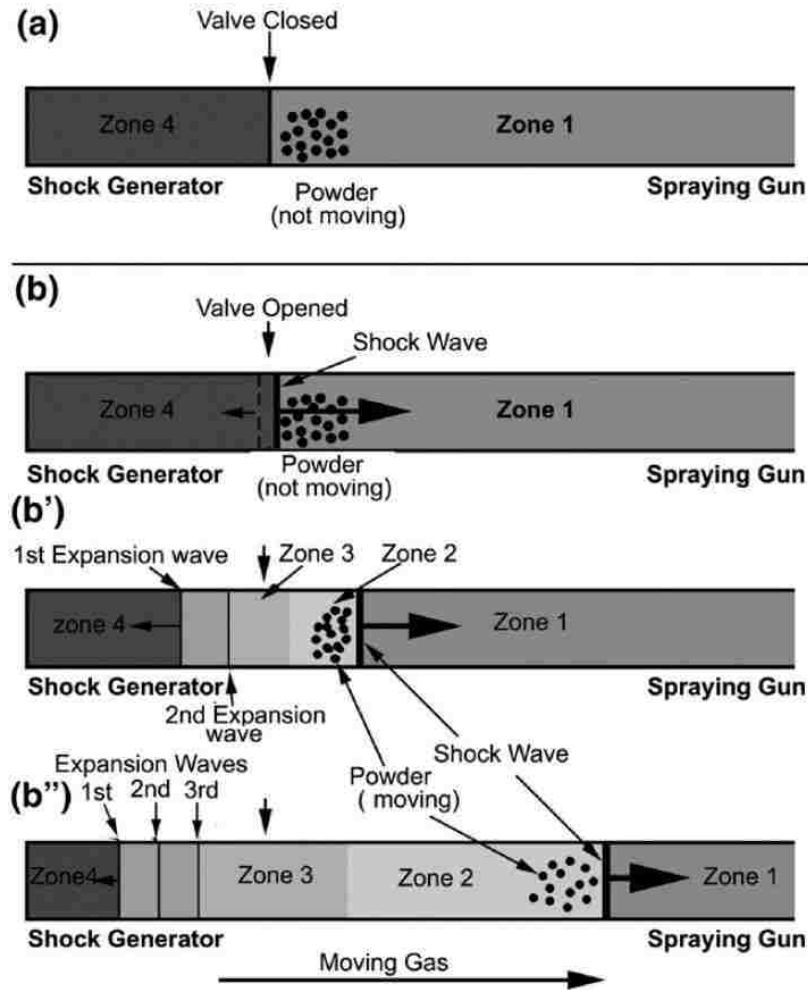


Figure 8: Schematic of the SISP spray device through one pulse spray cycle. Reproduced with permission [39].

The different zones in the flow can be mathematically represented using the one-dimensional transient model of the flow that was previously mentioned in Section 2.1. The one-dimensional model predicts the four distinct zones in the physical space, separated by three specific surfaces as shown in Figure 9. It estimates a single value for

different flow variables in zones one through three, and predicts how these zones evolve in time.

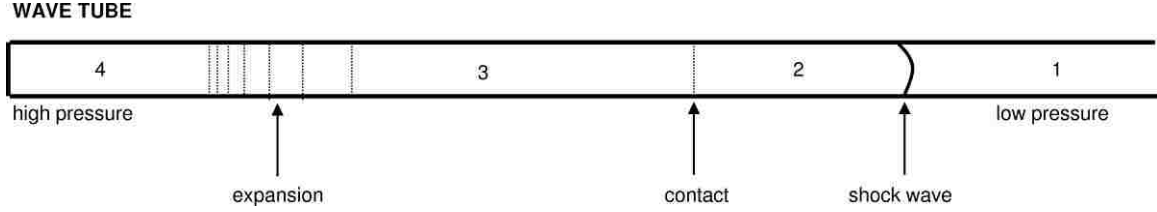


Figure 9: Schematic of the one-dimensional model.

The problem considered in the one-dimensional model is concerned with estimating the flow properties in zone 2 based on those in zones 1 and 4. Zone 1 represents the tube when empty from the flow of the preceding pulse, and zone 4 is the high-pressure region in the valve prior to its opening. The value of pressure in zone 2, based on the known conditions in zones 1 and 4, can be obtained using [39, 53]:

$$\frac{p_4}{p_1} = \frac{p_2}{p_1} \left\{ 1 - \frac{(\gamma_4 - 1)(c_1/c_4)(p_2/p_1 - 1)}{\sqrt{2\gamma_1[2\gamma_1 + (\gamma_1 + 1)(p_2/p_1 - 1)]}} \right\}^{-2\gamma_4/(\gamma_4 - 1)} \quad (1)$$

where c is the speed of sound and γ is the specific heat ratio. Values of temperature, density and the induced gas velocity in zone 2 can then be found using [39, 53]:

$$\frac{T_2}{T_1} = \frac{p_2}{p_1} \left(\frac{\frac{\gamma + 1}{\gamma - 1} + \frac{p_2}{p_1}}{1 + \frac{\gamma + 1}{\gamma - 1} \frac{p_2}{p_1}} \right) \quad (2)$$

$$\frac{\rho_2}{\rho_1} = \frac{1 + \frac{\gamma + 1}{\gamma - 1} \frac{p_2}{p_1}}{\frac{\gamma + 1}{\gamma - 1} + \frac{p_2}{p_1}} \quad (3)$$

$$V_2 = \frac{c_1}{\gamma} \left(\frac{p_2}{p_1} - 1 \right) \left(\frac{\frac{2\gamma}{\gamma+1}}{\frac{p_2}{p_1} + \frac{\gamma-1}{\gamma+1}} \right)^{1/2} \quad (4)$$

Solving these equations indicates that zone 2 will possess an elevated temperature and increased velocity concurrently. The promise of the technology mainly lies in this fact. Theoretical instantaneous values of gas speed and temperature just prior to the departure of the shock-wave from the spray tube are shown in Figure 10. This is the unique feature of SISP due to the unsteady nature of the flow. In steady-state cold spray processes increased gas velocity is always accompanied by a drop in gas temperature.

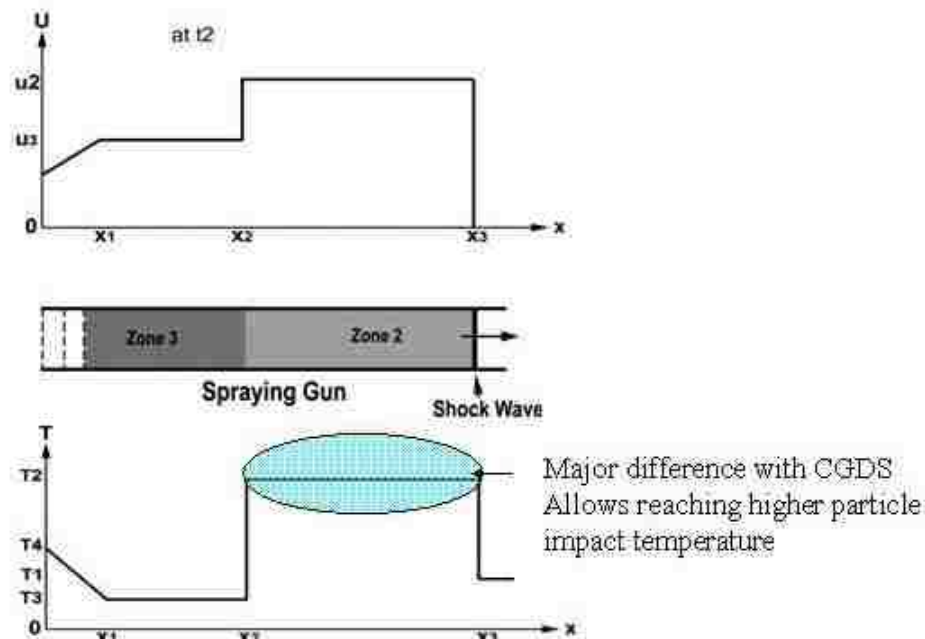


Figure 10: Theoretical instantaneous values of gas speed and temperature just prior to the departure of the shock-wave from the spray device. Reproduced with permission [39].

2.3 Objectives

This dissertation aims to advance the knowledge of the working principles of the Shock-wave Induced Spraying Process (SISP) through a systematic approach and use of advanced modeling tools. The specific objectives of this work are listed below:

1. To create a Computational Fluid Dynamics (CFD) model of a generic version of the spray device. This includes a reservoir, a valve, a tube, a representative substrate as well as a portion of the adjacent surroundings. Using this model it is desired to study various flow properties during the travel of a single shock-wave, in order to explain the underlying physics of the spray process. The model is to be general in nature, allowing investigation of the effect of various parameters on the resulting flow. This will include an accurate model of the in-line heater and a realistic model of the valve. This model will be validated through measurement and comparison of flow pressure and temperature where possible.

2. To use the model to examine effects of the important fundamental parameters on the flow properties of the device. These parameters will include the temperature and pressure of supply gas as well as the type of the carrier gas.

3. To model the behavior of particles traveling in the flow field. The goal is to examine the kinetic and thermal energies of the particles upon their impact on the substrate. This model will be validated independent of the gas phase.

4. To use this enhanced model to investigate the effect that particle injection location and timing has on the particle impact velocity and temperature.

5. To derive an estimation of the particle critical velocity [54] using available correlations [29] and make a comparison of particle velocity upon impact with corresponding critical velocity to determine the ability of obtaining a coating under a specific set of conditions.

6. To examine the influence of various operating parameters on the final outcome of the coating process using this model. These parameters include the spray frequency, main heater and powder heater set-point, particle material and size, length of the main gas heater as well as powder loading ratio.

2.4 Contents of Dissertation

The dissertation consists of five chapters. Chapter 1 introduced the working principles of thermal spray processes, and how SISP fits into this picture. In Chapter 2, a survey of the current state of the art of the SISP process was presented, and the general physics of the flow was described. The objectives of this undertaking were laid out in this chapter in light of where the technology currently stands. The remainder of the dissertation gives the details of how these are achieved.

Chapter 3 focuses on the details of the modeling technique, flow equations and assumptions, and how the model is constructed. In Chapter 4 the detailed scope of the

simulation work is laid out, and various stages of the work are explained. Methods used to validate the numerical model are also presented. Chapter 5 presents the results of the gas flow and the particle flow separately. The effects that many parameters have on the potential outcome of the spray process are investigated. Finally, the conclusions are drawn in the final chapter

Chapter 3. Numerical Methodology

Several details of the gas dynamics model, including the geometry and assumptions, governing equations, grid considerations as well as boundary and initial conditions are described in this chapter. The particle flow simulation is then described, in which the Discrete Phase Model is used.

3.1 Computational Gas Dynamic Model

The modeling presented in this study is conducted in three distinct stages, to incrementally increase the model complexity level while ensuring some level of validation at each stage. First, a simplified model is developed in Stage One focusing on the basic flow features resulting from the fast opening and closing of a valve. Due to the fundamental nature of this stage of the study and emphasis on understanding the flow physics, the geometry used at this stage is not an exact representation of the actual spray device.

Once the flow physics have been modeled, properly validated, and fully explained, the model is expanded to more closely represent the working device in Stage Two. A representative geometry is used at this stage and important process features such as gas heating and valve behavior are modeled. In Stage Three of the study, particle flow is also included and analyzed. A more completely representative model of the process is used at this stage to investigate effect of various working parameters of the device.

3.1.1 Problem Statement

The main elements of the system, shown schematically in Figure 11, include a high-pressure gas reservoir and a valve connected through a gas line, a spray tube, and a flat substrate. Different stages of the study use different values for the device length and therefore only the other geometrical parameter values are shown in this figure.

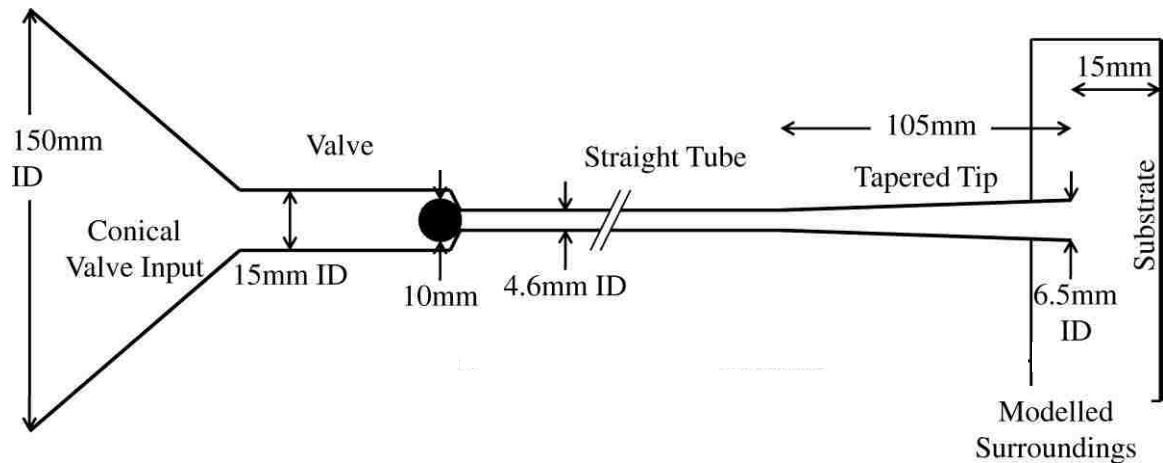


Figure 11: A generic schematic of the flow region.

The spray tube considered in this study is a standard $\frac{1}{4}$ " tubing (6.35 mm OD) with 0.035" (0.89 mm) wall thickness, resulting in a spray tube internal diameter of approximately 4.6 mm. The tube total length varies in different stages of the study. The tube has a tapered end which is 105 mm in length that leads to the end which has an internal diameter of 6.3 mm and is open to ambient air. The purpose of this tube taper is two-fold; it increases the spray pattern footprint while it increases the gas speed.

3.1.2 Assumptions

The main component, or heart, of the SISF system is its valve. A picture as well as a CAD representation of the valve are shown in Figure 12. The rendered CAD images

are generated using ICEM CFD (ANSYS, Canonsburg, Pennsylvania, USA) after extracting fluid volumes from the native CAD model. The model was imported to ICEM CFD using IGS Wireframe format. The native CAD model was generated in Autodesk Inventor (Autodesk, San Rafael, California, USA) for the purpose of manufacturing. The channels shown in Figure 12 (b) are formed in a stationary seat shown in Figure 12 (c). The volume shown in Figure 12 (d) rotates and gas passage is formed as the openings of this rotating volume align with the openings of the stationary seat. These openings are extended along the radial direction in order to ensure rapid opening and closing.

The flow is solved in an axisymmetric domain shown in Figure 11. Although the physical valve is of the rotary type, a ball-seat type valve is found to be a good representation as long as the model appropriately represents the kinematics of the real valve. The surface area of the model when fully open is initially equated to that of the real valve opening, leading to a stroke value of 0.6 mm. When the flow is modeled using this value for stroke, it is shown (in Section 4.2.2) that pressure peaks predicted by the model are lower than those measured by pressure transducers along the device tube, by approximately 20%. It is speculated that this is due to a difference in the discharge coefficient between the real and the modeled valve. Although the two valves have equal cross-sections when fully open, the modeled valve is more resistive to flow due to boundary layer formation along a very long surface compared to the real valve. The stroke was therefore increased by 20%, to approximately 0.72 mm. With this change the measured and calculated pressure peaks match very well. The valve opening and closing

behavior varies among the various stages of the study that will be explained in the next chapter.

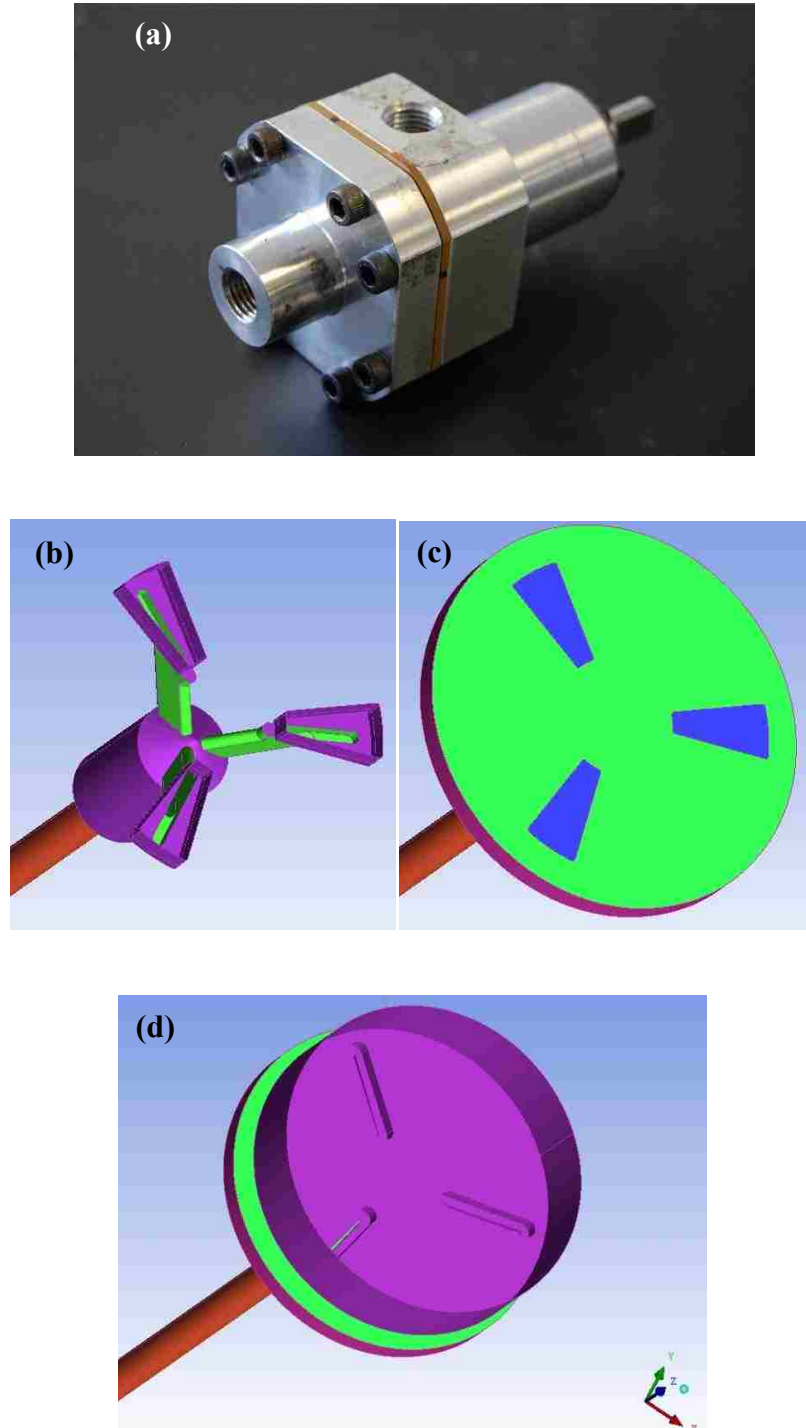


Figure 12: Picture and a CAD representation of the rotary-style valve used in the SISP device

The pressurized gas source is replaced in the model by a conical-shaped chamber attached to the valve entrance. The inlet to this chamber has a diameter of 150 mm, resulting in an area ratio between this section and the spray tube greater than 1000. This section can accurately represent the flow from a constant-pressure chamber. Based on the area ratio and using isentropic equations this assumption can be in error by a maximum of 0.01%.

In the physical device, gas heating is achieved by resistively heating a section of the spray tube. It is modeled using empirical information from the experiments. In the experiments an electrical control system ensures that the tube surface temperature at the end of this heating section reaches the desired input value. In order to model this effect, the actual temperature distribution along the length of the heating portion of the tube was measured using K-type thermocouples at certain intervals on the exterior of the heating tube. As shown in Figure 13, this temperature distribution can be closely approximated by a linear relation whose initial value is room temperature and final value is the set input temperature. Simulations were performed using the measured temperature profile and using the linear approximation. It was found that the linear approximation did not change the resulting predicted flow field, gas speed as well as gas temperature considerably (that is less than 5% compared to a case where the measured temperature profile was used). Consequently, the linear approximation is used as it allows for an easy change of the heater temperature setting.

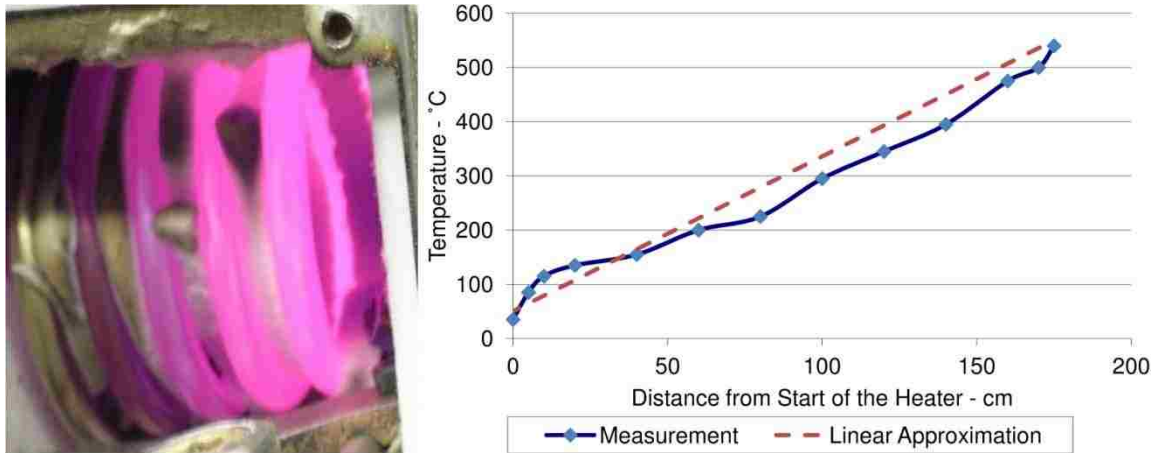


Figure 13: Left: a heating tube (in coiled form) during a heating process with gas flow, Right: comparison of measured temperature values along the heater tube with a linear approximation proposed for use as boundary condition in the simulation.

A moving shock-wave, travelling at transonic-supersonic speeds, is the central feature of the SISP process and hence the solution must account for compressibility effects. This is achieved by using a variable gas density in the numerical procedure. Additionally, the flow is expected to reach high speeds, suggesting the presence of high Reynolds numbers (in the order of 10^5 to 10^6). Moreover, it is desired to include effects of wall friction which have been neglected in previous one-dimensional models. Therefore viscous and turbulence effects need to be included.

The Spalart-Allmaras model is used to account for turbulence effects. This is a relatively simple one-equation turbulence model that solves a modeled transport equation for the kinematic eddy (turbulent) viscosity. It was designed specifically for aerospace applications involving wall-bounded flows and has been shown to give good results for boundary layers subjected to compressible flows and adverse pressure gradients [55]. Compared to other turbulence models which involve two or more equations, this model has the added benefit of greater simplicity and better efficiency.

3.1.3 Governing Equations

The mathematical model of fluid flow and heat transfer in general is developed from the laws of physics: conservation of mass, momentum equation, and conservation of energy. These laws are presented in Equations 5-7.

Conservation of mass (Continuity equation)

$$\frac{\partial \rho}{\partial t} + \nabla \cdot (\rho \vec{u}) = 0 \quad (5)$$

Momentum equation

$$\frac{\partial}{\partial t} (\rho \vec{u}) + \nabla \cdot (\rho \vec{u} \vec{u}) = -\nabla p + \nabla \cdot \vec{\tau} \quad (6)$$

Conservation of energy

$$\frac{\partial}{\partial t} (\rho E) + \nabla \cdot (\rho E \vec{u}) = -\nabla \cdot (p \vec{u}) + \nabla \cdot (k \text{ grad } T) + \nabla \cdot (\vec{u} \cdot \vec{\tau}) \quad (7)$$

The mass conservation equation and the momentum equations are given in the unsteady axisymmetric (no swirl) form for a Newtonian fluid with constant viscosity in Equations 8-10. These equations relate the values of axial and radial components of velocity to pressure and density as a function of time.

Conservation of mass (Continuity equation):

$$\frac{\partial \rho}{\partial t} + \frac{1}{r} \frac{\partial}{\partial r} (\rho r u_r) + \frac{\partial (\rho u_x)}{\partial x} = 0 \quad (8)$$

Momentum equation in the radial directions:

$$\begin{aligned} \text{r: } & \frac{\partial}{\partial t} (\rho u_r) + \frac{1}{r} \frac{\partial}{\partial x} (r \rho u_x u_r) + \frac{1}{r} \frac{\partial}{\partial r} (r \rho u_r u_r) \\ & = -\frac{\partial p}{\partial r} + \frac{1}{r} \frac{\partial}{\partial x} \left[r \mu \left(\frac{\partial u_r}{\partial x} + \frac{\partial u_x}{\partial r} \right) \right] \\ & + \frac{1}{r} \frac{\partial}{\partial r} \left[r \mu \left(2 \frac{\partial u_r}{\partial r} - \frac{2}{3} (\nabla \cdot \vec{u}) \right) \right] - 2\mu \frac{u_r}{r^2} \\ & + \frac{2}{3} \frac{\mu}{r} (\nabla \cdot \vec{u}) \end{aligned} \quad (9)$$

Momentum equation in the axial directions:

$$\begin{aligned} \text{x: } & \frac{\partial}{\partial t} (\rho u_x) + \frac{1}{r} \frac{\partial}{\partial x} (r \rho u_x u_x) + \frac{1}{r} \frac{\partial}{\partial r} (r \rho u_r u_x) \\ & = -\frac{\partial p}{\partial x} + \frac{1}{r} \frac{\partial}{\partial x} \left[r \mu \left(2 \frac{\partial u_x}{\partial x} - \frac{2}{3} (\nabla \cdot \vec{u}) \right) \right] \\ & + \frac{1}{r} \frac{\partial}{\partial r} \left[r \mu \left(\frac{\partial u_x}{\partial r} + \frac{\partial u_r}{\partial x} \right) \right] \end{aligned} \quad (10)$$

In Equations 4-6, gas mass density is treated as a variable due to compressibility effects. This quantity is related to pressure and temperature through the ideal-gas law given by Equation 11 (constant heat capacities are assumed).

$$\rho = \frac{p}{\frac{R}{M_w} T} \quad (11)$$

where R is the universal gas constant, M_w is the molecular weight of the gas, and p is the static pressure.

3.1.4 Grid Considerations

In general, for a two-dimensional domain, a quadrilateral block mesh is the most efficient type of mesh. It allows for a more accurate solution near walls and less computational effort for the same spatial resolution when compared to other schemes. For the problem in hand, quadrilateral block grid generation is used to mesh the entire domain, except for a small region near the valve ball (see Figure 14). The grid is clustered close to walls, especially inside the tube where boundary layer effects are expected to be predominant.

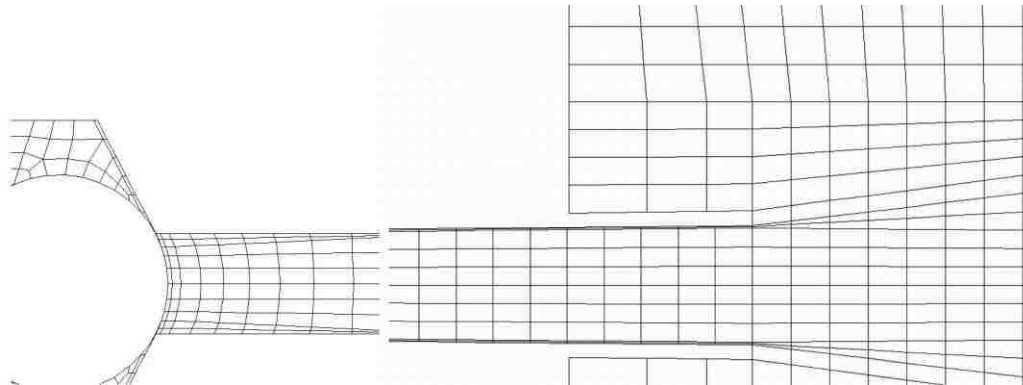


Figure 14: Mesh, near the valve ball (left) and near the tube exit and substrate (right).

The grid system that is used contains a total of 3775 cells. This grid is used to initiate the solution process. The number of cells, however, will increase due to grid

adaption as well as addition of cells as the valve ball moves, and finally reaches close to 6000 cells.

As the flow field solution evolves with time, it is expected that areas of high gradients of flow properties will form. In such regions a grid resolution higher than the original grid is required in order to fully resolve the flow. However, the location of these regions is difficult to predict beforehand, and will likely move as the solution evolves in time and the shock-wave moves. In order to minimize computational time, the grid is updated at each time step. This technique allows using the original grid, shown in Figure 14, across the domain while refining it in the areas where needed.

In a high-speed transonic flow such as the one being studied, shock-waves, compression waves and expansion waves result in regions of high pressure gradients. This quantity is used to determine regions of grid refinement. It is expected that pressure gradients and velocity values inside the majority of the valve and in the reservoir are small. The areas of the valve close to its opening are likely subject to high gradients, however this region already has a very fine grid system. Therefore grid adaption is used only downstream of the valve. A maximum of two levels of refinement is allowed. An image of an area of the tube where the grid has been refined is shown in Figure 15. The grid is shown superimposed on the contours of static pressure. Areas of no refinement, one level of refinement, and two levels of refinement can be identified.

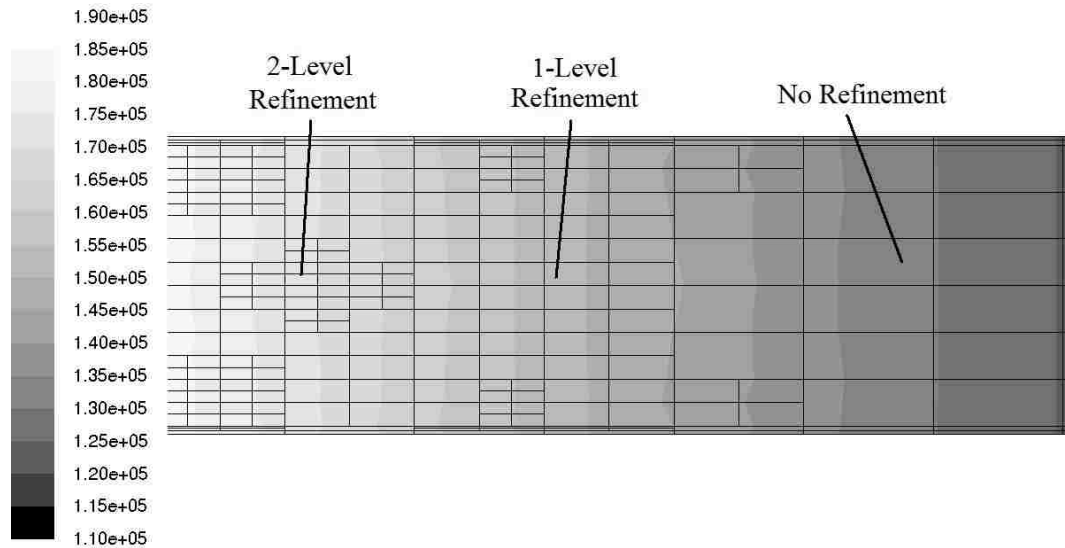


Figure 15: Adapted grid superimposed on contours of static pressure (Pa) at $t = 0.2$ m. A 14-mm-long portion of the tube, 110 mm downstream of valve.

Another important consideration for the grid system is the treatment of the ball motion. This motion will affect the grid geometry around it: behind the ball near the valve seat, in front of it in the valve region, as well as in the area between the ball and the valve cylindrical walls. The latter is the simplest to handle by creating a fluid zone in this region and defining the same movement profile as the valve ball itself using dynamic meshing. A similar approach is used in the valve region. However, special treatment is required at the interface of the fluid region and the inlet surface of the cylindrical valve. A similar situation exists between the ball and the seat. A zone is created for each of these two regions that moves along with the ball. This movement, during the opening of the valve, pushes some cells out of the inlet surface of the reservoir and creates a void in the region between the valve ball and the valve seat. The situation is reverse while the valve is closing.

The motion is implemented through dynamic meshing. Dynamic meshing allows the deformation of cells affected by the motion of moving boundaries to be adapted. Several dynamic mesh methods are available: smoothing, layering and re-meshing. For the application in hand layering is the most appropriate method.

The layering method splits and merges layers by a factor of height or by a ratio specified in the dynamic mesh zone when a moving boundary reaches the neighbouring nodes. Figure 16 shows an example of the method. For instance, let height be h and the collapse factor be specified as 0.5 (Figure 16 center). When a moving boundary moves inwards to the domain (Figure 16 center) the last layer is modified until the boundary crosses the line at a distance of $0.5 \cdot h$ (Figure 16 right). At this point, Layer 1 will be merged into the moving boundary. The equations for handling the split and collapse cases are given as:

$$\text{Split:} \quad h > (1 + \alpha_s) \cdot h_{min}$$

$$\text{Collapse:} \quad h < \alpha_c \cdot h_{min}$$

where α_s is split factor, α_c is collapse factor and h_{min} is the ideal size of cell height. Note that the layering method only works with a structured mesh.

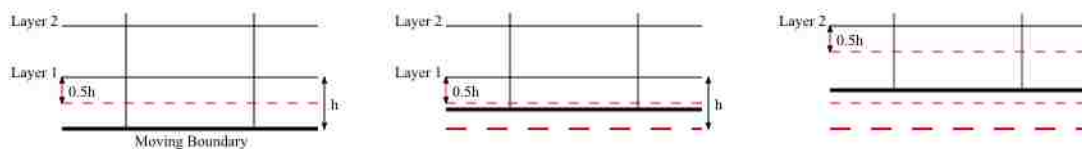


Figure 16: Dynamic meshing - layering method

Images demonstrating how this process works near the contact area on the seat of the ball valve are shown in Figure 17. The original mesh is shown on the left, with a magnified image shown in the center. The image to the right is 0.2 ms after the start of the simulation, with the row of cells adjacent to the ball showing some expansion and three new rows of cells added.

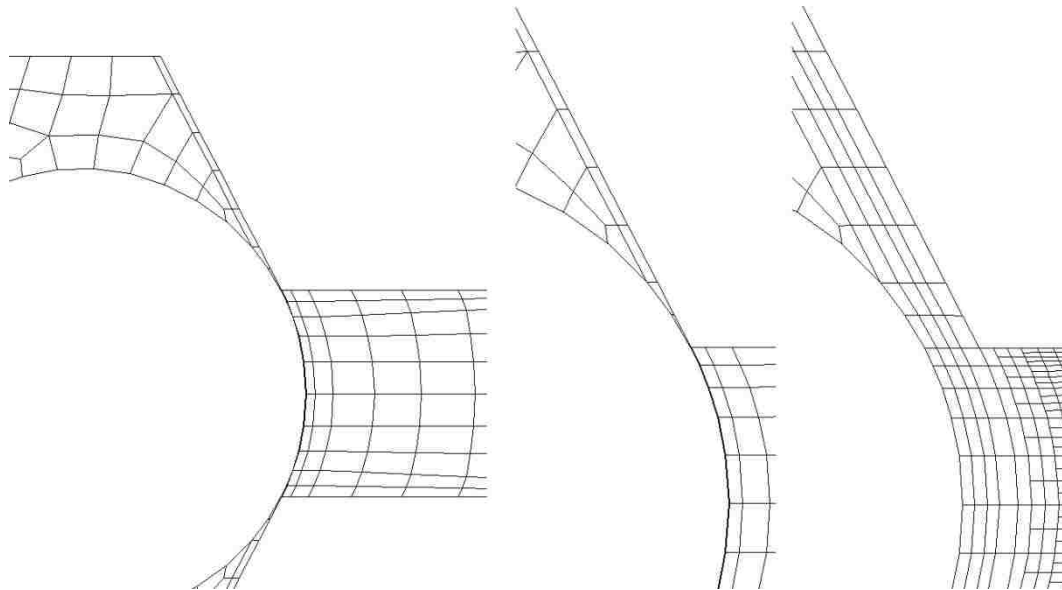


Figure 17: Mesh near the valve ball (left), zoomed in with the valve closed (center) and in the process of opening (right).

3.1.5 Boundary Conditions

At the entrance of the conical valve input, which represents a large reservoir, a pressure inlet with uniform pressure is defined. The no-slip condition as well as zero heat transfer condition are used on each wall of the tube and the substrate. The zero heat transfer assumption is a good representation of the actual device since the barrel is thermally insulated in the physical device in both the heater area as well as the tube extension. When the heater is in operation, temperature values are imposed along its wall to account for this. This is implemented through a Profile, which assigns temperature

values as a function of axial location, as included in Appendix B. At all boundaries within the surrounding air a pressure outlet with uniform atmospheric pressure value is applied.

3.1.6 Initial Conditions

The initial condition for the transient solution is the steady state solution to the problem, given the boundary conditions, at zero time. This is a solution with the valve closed. In this state the valve should fully obstruct the flow. This means the sub-domains upstream and downstream of the valve are fully separated and disconnected, which cannot be handled by the solver used for this study. As a result, when the valve is closed a minimal gap between the valve ball and its seat is left open in order to maintain the integrity of the domain. It is determined that a gap of 0.01 mm is suitable for this purpose, resulting in a leak by as much as 0.4% of the fully open / choked flow. The effect of a leak is an increase in the pressure of the empty tube after the closure of the valve following each pulse. This leads to a lowering of the pressure ratio between the valve and the tube prior to the next pulse, and consequently a weakening of the pulse. This is expected to be negligible in the case of this simulation due to the very low magnitude of the leak.

3.2 Discrete Phase Model

A Lagrangian formulation, with no particle-particle interaction and no effect of the particles on the flow is assumed. This so-called 'dilute' assumption is a good representation of the device under actual operating conditions. An increase in powder

concentration causes a drop in the velocity and temperature of the gas flow [56]. This adversely affects the performance of the process. However the device is normally charged for each pulse with a quantity of powder that will not affect its performance, satisfying the dilute assumption.

Additionally, in order to maintain the axial symmetry of the model, the gas flow carrying particles into the main flow is neglected, and particles are injected at zero initial speed. The gas flow through the powder feed line is not expected to influence the main flow significantly as the magnitude of the powder feeder flow on average is normally about two orders of magnitude less than the main gas flow.

The particle motion is caused by the drag force exerted on the particles by the flow field and determined based on the drag coefficient, C_D . Empirical correlations for this coefficient involve the relative values of particle Reynolds and Mach numbers, Re_p and M_p . Data presented by Clift et al. [57] gives the dependence of drag coefficient on M_p for several values of Re_p . It accounts for a wide range of flow-particle Mach numbers and Reynolds numbers ($0.1 < M_p < 10$ and $0.2 < Re_p < 104$). This range covers the conditions encountered in the SISP process and is used in this study. This same relationship has been successfully used previously in simulations of cold spray processes [26, 31, 58].

Heat transfer between the particles and flow is important as the critical velocity of a particle depends heavily on its temperature at the time of impact [29]. It is assumed that there is negligible internal resistance to heat transfer within a particle and hence the

particle is at a uniform temperature at any given time which has previously been demonstrated and used in the literature [26, 31]. The validity of this assumption can be assessed by estimating the value of the Biot number, Bi , as introduced in Equation 12, where h denotes the coefficient of heat transfer, and d_p and k_p represent the diameter and thermal conductivity of the particle respectively. Biot number represents the ratio of convective heat transfer from the surface of an object to the conductive heat transfer through the object. If this quantity has a value less than 0.1 the constant-temperature assumption is valid. This quantity is maximum at the greatest heat transfer coefficient (maximum $250 \text{ W/m}^2\cdot\text{k}$ for forced convection in gases), and largest particle size (40 microns) and the lowest thermal conductivity ($16 \text{ W/m}^2\cdot\text{k}$ for stainless steel). This combination results in a Biot number that is more than two orders of magnitude less than the threshold Bi value of 0.1.

$$Bi = h \cdot d_p / k_p \quad (12)$$

All thermodynamic properties required for calculating heat transfer rate are known and assumed constant except for the flow-particle convective heat transfer coefficient. This coefficient appears in the definition of the flow-particle Nusselt number, Nu . A simple correlation exists [59] that links Nu with particle Reynolds number, Re_p , and the Prandtl number, Pr , both of which are known or can be calculated from Equation 13.

$$Nu = 2 + 0.6Re_p^{1/2}Pr^{1/3} \quad \text{for } M_p < 0.24 \text{ or } T_g < T_p \quad (13)$$

This relationship has been used in modeling the cold spray process [26]. However, the limitation of this correlation regarding M_p and T_g makes it inapplicable over much of the cycle in the case of SISP. These conditions are met in cold spray processes during the majority of particle travel, mainly as relative particle Mach number drops quickly as particles accelerate in the flow stream. In the unsteady case of SISP, however, these conditions may not be valid depending on whether the particle falls in the expansion or compression zone of the flow regime. A more general correlation, with dependence on particle Mach number, must be used to handle the ranges not covered by the simple correlation above and is given by Equation 14 [26, 31].

$$\text{Nu} = 2 + 0.44\text{Re}_p^{1/2}\text{Pr}^{1/3}\exp(0.1+0.872M_p) \quad \text{for} \quad (14)$$

$$M_p > 0.24 \quad \text{and} \quad T_g > T_p$$

3.3 Solver Settings

In order to conduct the simulation, Fluent software (ANSYS, Canonsburg, Pennsylvania, USA) [60] is used as the solver. Two general categories of solvers are available; namely density-based and pressure-based. The pressure-based solver uses a solution algorithm where the governing equations are solved sequentially (i.e., segregated from one another) [55]. Density-based solvers simultaneously solve the governing equations of continuity, momentum and energy as a set, or vector, of equations. As the degree of coupling increases, so does the computational burden of an algorithm. However, this also improves the rate of convergence as well as the stability of the algorithm. The density-based solver is more computationally intensive and more stable than the pressure-based solver. It is the solver of choice for compressible, transonic flows

without significant regions of low-speed flow. In cases with significant low-speed flow regions, the pressure-based solver is preferred [55]. The problem in hand is a combination of both. It is expected that the flow is predominantly transonic while the valve is open but will have significant low-speed regions when it is closed. The density-based solver is selected due to solution stability issues with the pressure-based solver.

The density-based solver is available with either an implicit or an explicit formulation in space domain. In general, the implicit formulation is more memory-intensive, however results in better convergence. For transient cases with traveling shocks, the density-based explicit solver (with explicit time stepping) may be the most efficient [55]. Nevertheless, in order to ensure better solution stability, the implicit formulation in space is used. In summary, the coupled (density-based) implicit approach is used, which solves all equations (conservation of mass, momentum equations, as well as energy equation) in all cells simultaneously.

The density-based solver with implicit formulation in space offers three choices for transient formulation; explicit, first-order implicit and second-order implicit. Due to stability concerns as a result of high velocities and flow gradients, the explicit solver (in time) may cause issues with solution stabilities and is not a good choice. Normally, the second-order implicit transient formulation is preferred because it potentially results in better solution accuracy at a larger time step. However, dynamic mesh simulation which is required to model valve motion currently is available only with first-order time advancement, leaving this as the only option for transient formulation. In order to ensure

that this choice of transient formulation will yield an accurate time-resolved solution, a study of the magnitude of time step is required as explained later.

In order to enable automatic updates to the grid at each time step, grid adaption is utilized. As explained previously, pressure gradients are used in order to determine which areas of the mesh need refinement. A maximum of two levels of refinement is allowed. Valve motion is implemented by the use of a Profile, as included in Appendix B. The change in geometry and grid as a result of this motion is accommodated through dynamic meshing. Layering is the best method for handling the case in hand. Values of the split factor, α_s , and collapse factor, α_c , are left to the default values of 0.4 and 0.04 respectively.

For the discrete phase, placing particles at several radial locations will add a major dimension to the complexity of the problem, and will be very computationally expensive. It is therefore desired to investigate if variations in the initial radial location will have a significant effect on the fate of the particles. Powder particles are initiated at a radial location very close to the central axis of the device. This central location ($r/R = 0.0$) is compared with a location close to the wall ($r/R = 0.8$) and an intermediate location ($r/R = 0.5$), where R denotes the radius of the spray tube. It is found that the thermal and kinetic components of particle energies upon impacting a substrate are varied slightly when their radial injection location is varied. As injection location gets closer to the tube wall particle temperatures tend to rise slightly while their speed decreases also slightly. The results supporting these findings are presented in Appendix D. The central location,

therefore, offers a good representation for the entire spectrum of radial locations of the initial injection.

The particles are introduced every 5 mm along the length of the spray gun, and at every 10th time step. Particle tracking is conducted at every gas iteration. The initial temperature, size and material of the injected particles are set according to the specific conditions of each simulation.

The heat transfer model that was previously described takes into account the effect of relative particle Mach number. This model is not readily available in Fluent, and therefore a User-Defined Function (UDF) is developed in order to account for this. This UDF is included in Appendix C.

Chapter 4. Numerical Experiments, Verification and Validation

The three stages of the study are aimed to serve different purposes. Stage One is conducted to explain the flow physics in the device. A shortened device length is used for this study as the device length will introduce no additional flow physics. Details are added to the model and subsequent stages provide a more realistic representation of the actual device. Geometrical properties of the device are similar in different stages except for the device length. These geometrical parameters of the spray device are summarized in Table 2.

Table 2: Geometrical features of the device modeled.

Item	Value - Stage One	Value - Stage Two and Three
Spray Tube	Standard 6.35 mm ($\frac{1}{4}$ " OD, 4.6 mm (0.18" ID	
Total Length	1240 mm	2250 mm
Tip Configuration	Tapered, 105 mm long, 6.5 mm ID	

The specifics details of the model set-up for each stage are explained below while the next chapter reports the results of these stages.

4.1 Stage One: Generic Gas Flow

The goal of Stage One of this work is to simulate the unsteady transonic gas flow through the SISP device in order to explain the overall flow physics. Therefore a shorter

device length than the real case is adopted. Moreover some details such as gas heater behavior and actual temporal behavior of the valve are ignored.

4.1.1 Model Conditions

A schematic depiction of the spray device used in this stage of the study is shown in Figure 18. The spray tube considered in this stage of the study is based on the real device which is a standard $\frac{1}{4}$ " (6.35 mm OD) tubing with 0.035" (0.89 mm) wall thickness, resulting in a spray tube internal diameter of approximately 4.6 mm. The total length of the tube however, is 1240 mm at this stage. The remaining geometrical details are summarized in Table 2.

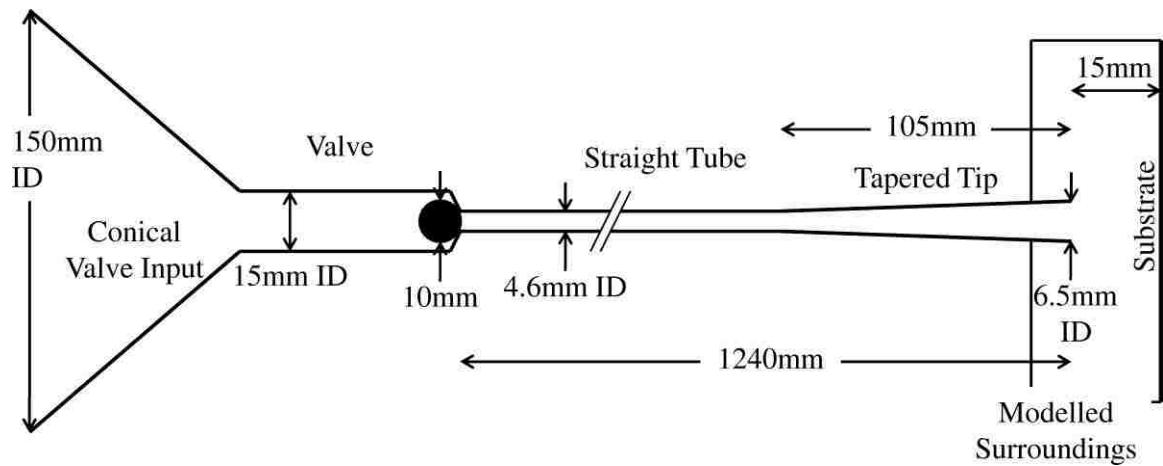


Figure 18: Schematic of the flow region used at Stage One.

For this stage, the valve comes to a fully opened state in 1ms and immediately closes over a period of 2 ms. These motion characteristics were determined based on open-close electric commands sent to a ball-seat valve at the early stages of the prototype development. The approximation used at this stage will not change the flow physics and

therefore emphasis is not placed on a more accurate representation of the real ball-seat valve.

In Stage One the gas heater effect is included through introduction of preheated gas at the valve inlet. This simplifies the modelling effort and allows a better understanding of the contribution of the travelling shock-wave within the process.

The key parameters for the operation of the spray device are the supply gas pressure, the heat input to the system, as well as the gas medium that is used. The typical values for these parameters which are considered in this study, are summarized in Table 3.

Table 3: Simulation conditions considered in the Stage One of the study.

Parameter	Value	Comment
Reservoir Pressure	1 MPa, 2 MPa	Can be varied as a boundary condition.
Driver Gas Temperature (Supplied to the Valve)	Ambient (23 °C), 300 °C	Can be varied as a boundary condition.
Media	Air, He	This is for both the flow gas and ambient. Ideal gas law is used.

Of all possible combinations of these parameters, four combinations are chosen that will show the effect that the three parameters of interest have on the flow field. These combinations are indicated in Table 4.

Table 4: Combinations of interest for simulation conditions for this study.

Simulation Condition	Air 1MPa No Heat	Air 2MPa No Heat	Air 2MPa 300°C	He 2MPa No Heat
Pressure	Included	Included		
Heat		Included	Included	
Gas Type		Included		Included

4.1.2 Model Verification

Model verification is conducted to ensure the equations for the simulation task are solved properly. This concerns the details of the modeling process, for example the grid geometry and size as well as the time step size for transient problems. These considerations are addressed in Stage One and apply to the simulations conducted in the following stages of the work.

The grid size and refinement level is verified through a grid sensitivity study. This process was started by utilizing a grid with seven cells across the radius of the tube, with three layers of cells in the boundary layer zone. Finer and coarser grids were then studied

as summarized in columns one through four in Table 5. Number of cells along the radius of the tube is used as a reference, and the cell size along the axial direction also varied accordingly.

Table 5: Summary of various grids used in the grid sensitivity study.

Grid #	Total Cells along Radius	Boundary Layer Cells	Total Cells	Observation Regarding Solution
1	15	3	33940	This solution is identical to solution from Grid #2.
2	7	3	7197	This is the original grid. The solution is identical to that of Grid #1 and similar that of Grid #3.
3	5	2	3775	This solution is different from that of Grid #4 but similar to that of Grid #2.
4	3	1	1365	This solution is different from that of Grid #3, and shows slight divergence.

The solutions obtained from these grids are compared in order to determine the best grid for the study. For this purpose values of static temperature and axial velocity along the centerline are plotted in Figure 19 at select time steps. These time steps are selected during the first 4 ms of the solution, when the shock-wave is passing through the device. It is found that grids with 5 and 7 cells along the radius result in a similar solution. With the coarsest grid, however, it is found to be difficult to generate a stable solution. Once this solution is achieved, however, it shows a maximum of 3% difference

in the values of peak temperature and local differences of 10% in the values of peak velocity. It is, therefore, concluded that grid #3 with 5 cells along the tube radius is most appropriate and therefore is used for this study. This grid size presents the optimum balance of accuracy and computational efficiency. The results of this study are summarized in the last column of Table 5.

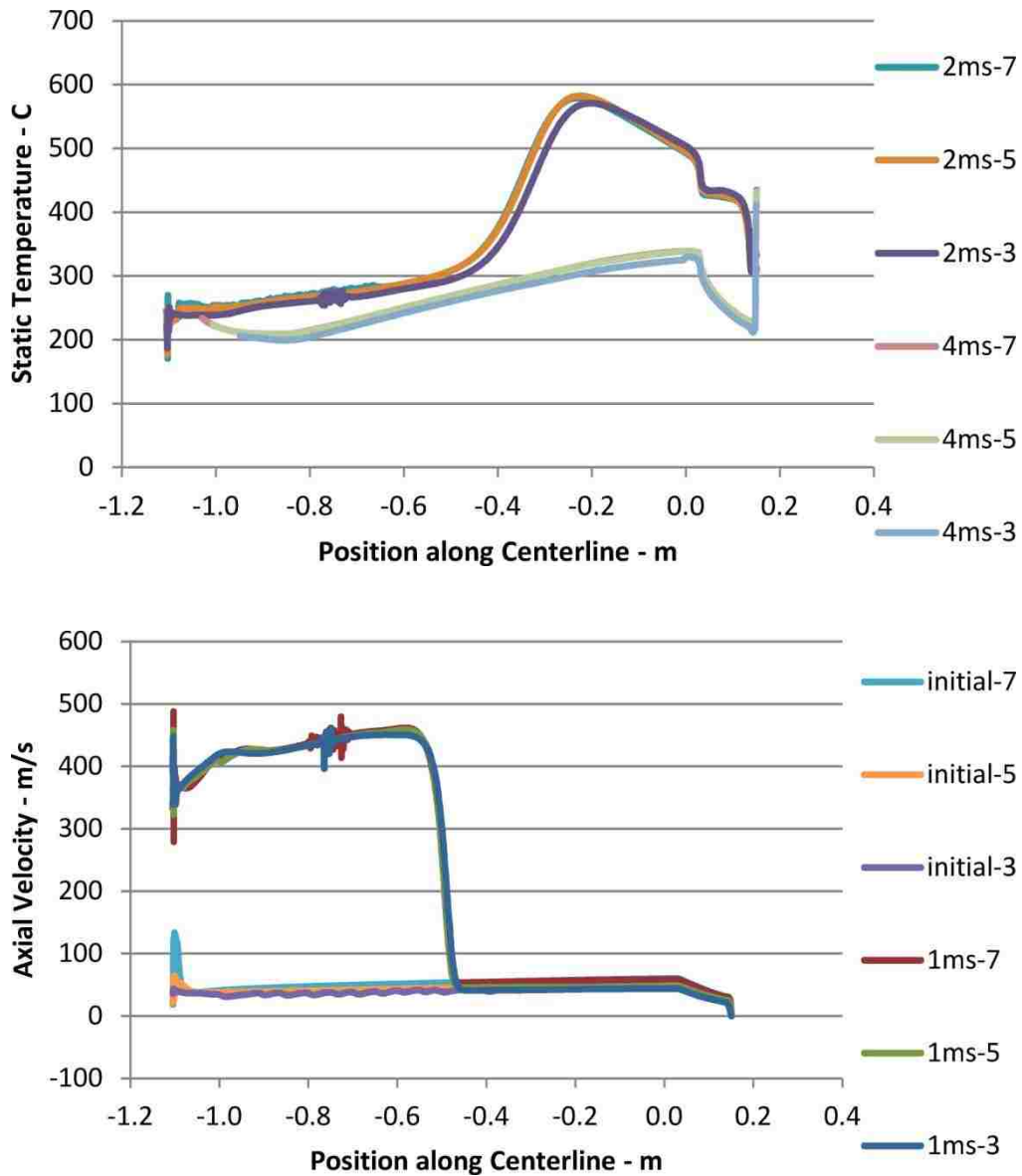


Figure 19: Values of static temperature and axial velocity along the centerline of the device at two time instants using grids with 3, 5 and 7 cells along the radius

In order to determine the optimum time step value, three different time steps are considered, namely 0.02 (double), 0.01 (current) and 0.005 ms (half). For the application of interest the important flow variables are the gas velocity and static temperature. Therefore the effect of time step on these two flow properties is investigated by plotting the values along the centerline at three times in the cycle for the three time steps, as depicted in Figure 20. Axial velocity, which is the most dominant velocity component in this flow, remains mostly unchanged as time step changes. At the instant of the valve closure, a dip in this variable is observed at the two larger time step values that is more pronounced at 0.02 ms. This feature is therefore only a numerical anomaly. However, this anomaly can result in solution stability issues at higher pressure ratios, which renders the largest time step unsuitable. Although the solution with the finest time step is closer to reality from the point of view of this feature, since its occurrence does not influence the accuracy of the solution in other locations it can be ignored and the time step of 0.01 ms is deemed to be most suitable.

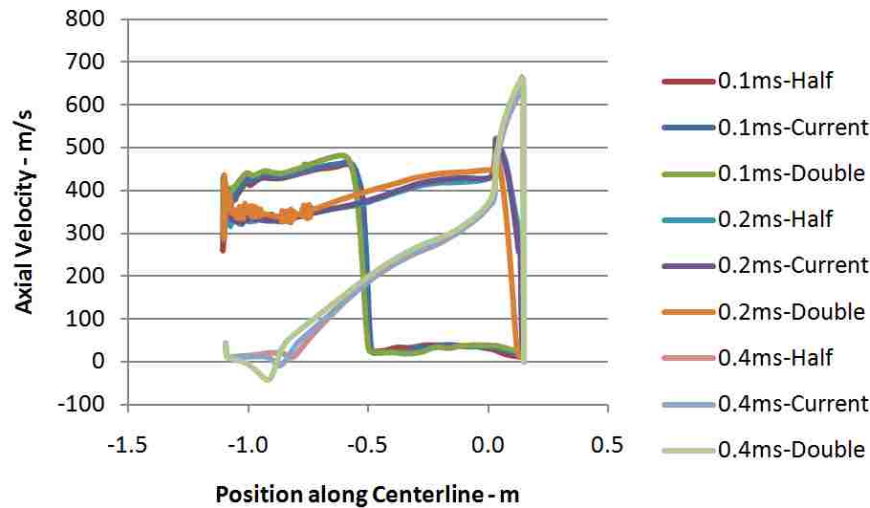
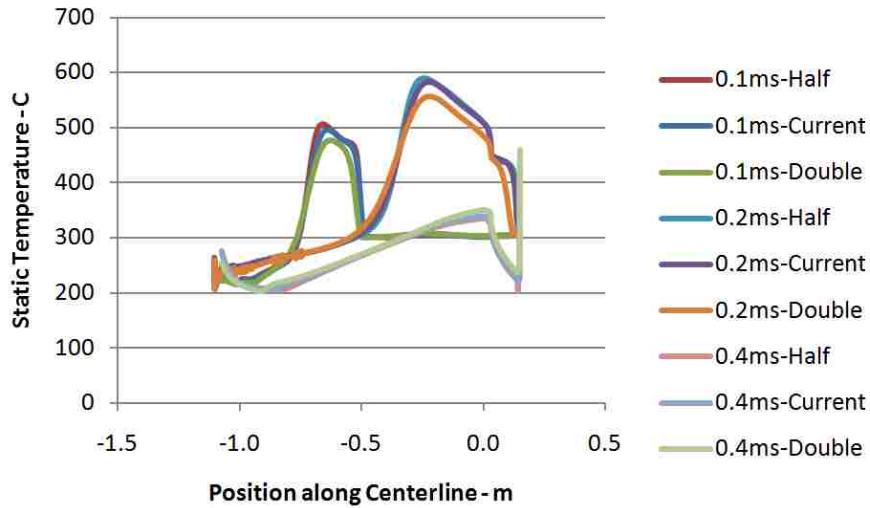


Figure 20: Values of static temperature (top) and axial velocity (bottom) at three solution times using three different time step values.

When considering values of static temperature it appears that all three solutions generate similar trends and close values. However, especially at 1 ms and 2 ms, the coarsest time step of 0.02 ms seems to slightly underestimate these values. To this end, a time step of 0.01 ms is the optimal choice for the problem in hand. The maximum number of iterations per time step is set to 100 for all solutions considered.

Another important aspect of the simulation work is how similar consecutive pulses are to one another, and how many pulses it takes to reach a repeatable pattern. The result of the pulses that are not similar to future ones should be dismissed, and the pulse that is similar to the rest must be used to conduct the analysis. If the flow field in the tube prior to the start of two pulses is similar to one another, the two pulses will be similar to one another. Therefore plots of velocity magnitude and static temperature, along the axis of the spray device at the start of four consecutive pulses, are plotted in the left and right portions of Figure 21 respectively. It is evident that plots at the start of pulse one and two are radically different, but the plot at the start of pulse two is nearly identical to all future plots. Therefore pulse two is taken for analysis through the rest of this study.

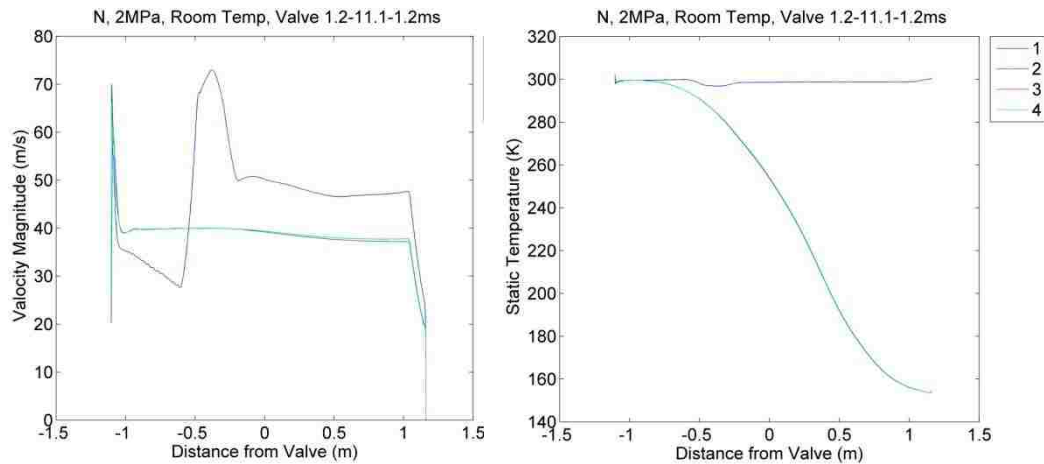


Figure 21: Values of velocity magnitude (left) and static temperature (right) along the spray device centerline at the beginning of the first four pulses.

4.1.3 Presentation of Results

In an attempt to study the results of these simulations it is important to establish a method to effectively present them. A simple approach is to create contour images of the flow field at different time steps and present them in sequence. An example of this is

shown in Figure 22. Each horizontal region in this diagram represents the contour plot of static temperature throughout the solution domain at one instant of time. The upper-most region corresponds to the solution at 0.0 ms, and each subsequent one is the solution at 0.4 ms time intervals. For all the simulations included in this stage, the valve opens in 1ms and immediately closes in 2 ms. These opening/closing times are somewhat arbitrary but deemed short enough to result in the formation of a shock-wave in the spray gun.

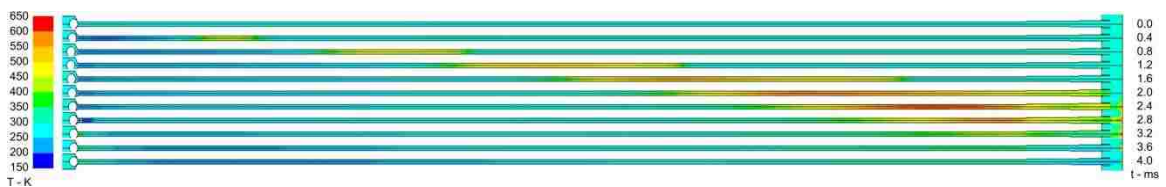


Figure 22: Sequential contours of static temperature at 0 ms to 4 ms. Air, 2 MPa, room temperature.

It is possible to develop a more effective technique for presenting the important results. In this technique, values of each specific flow variable of interest are extracted at a specific radius (on the centerline in this case) of the flow field at every time step. A Journal file that was created to extract these data is shown in Appendix E. In doing this it is assumed that these values are a good representative of the flow variables at all other radial locations. A close examination of Figure 22 confirms that this is a reasonable assumption; the value of static temperature at the centerline, at each time and axial location, extend well to the walls of the tube. This information can then be processed to create a two-dimensional graph where the horizontal axis represents the axial position in the spray apparatus and the vertical axis represents solution time. The Matlab (Mathworks, Natick, Massachusetts, USA) program and relevant functions that were developed for this purpose are included in Appendix F. An example of implementing this

technique to present the results is shown in Figure 23. This image pertains to the same operating conditions as those shown in Figure 22.

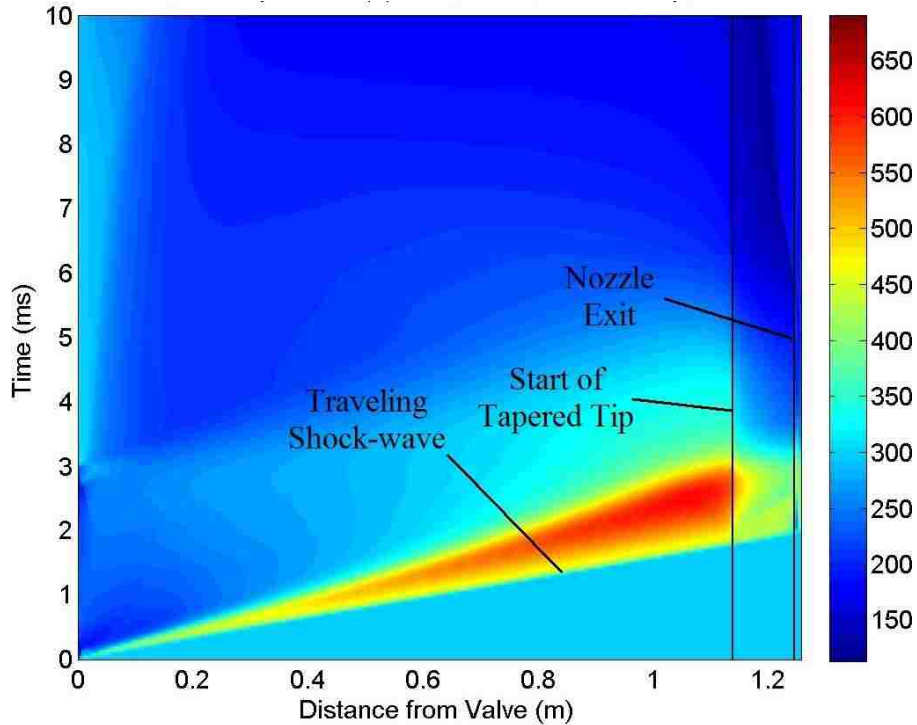


Figure 23: Contours of static temperature (K) in space-time domain – Air, 2 MPa, no heat.

This image is a typical representation of the results used throughout this section. The extent of the space domain starts from the valve exit and stretches to the substrate. The locations of the start of the tapered section as well as the nozzle exit are shown by two vertical lines in Figure 23. It is important to note how close the nozzle exit is located with respect to the substrate when compared to the total length of the tube; this distance is only 15mm compared to the overall tube length of 1240 mm, which is about two orders of magnitude shorter.

The location of a traveling shock-wave that occurs as a result of fast opening and closing of the valve is also identified. The slope of this line represents the shock-wave velocity, the closer this line to the horizontal direction the faster the shock-wave travels. It is concluded that this technique for presenting the results is very effective in understanding and explaining various characteristics of the flow. A similar technique, however executed predominantly in black-and-white coloring and utilizing plain lines to create zones of different values, is typically seen in research aimed at studying shock tubes and other one-dimensional transient problems.

4.1.4 Model Validation

The problem of discharging gas from a reservoir to ambient through a channel can be simplified to a one-dimensional unsteady problem. This type of problem is commonly encountered in the analysis of shock tubes. If wall friction and viscous effects are ignored, simple models exist based on compressible flow theory that can predict flow properties in such situations [53]. These models have been previously applied to the shock tube problem [33]. They can therefore be used as a base for validating this CFD solution. This model has been previously incorporated into a calculator for the purpose of predicting the SISP performance [39]. The one-dimensional results used here for the purpose of comparison are based on this flow calculator.

Ideally, model validation should be performed using experimental measurements. This has been done at the Stage Two of the study, however comparison with simplified one-dimensional model results is deemed useful in showing that the current results are

reasonable. A comprehensive account of this one-dimensional analysis is available in the literature [39].

The valve parameters used at this stage are an approximation of the reality. Therefore the result, although qualitatively valid, may be quantitatively different in some aspects from the real case. Nevertheless, the process fundamentals will be similar between the real case and those predicted in this model and hence it is deemed reasonable to use this approach of comparing with simplified theory.

In this case gas pressure and temperature are used for the comparison. The value considered is the time it takes for the front-most pressure spike, called the ‘Shock Front’ in the one-dimensional solution, to reach the tube exit. The second is the temperature of the gas immediately trailing the shock front, called the ‘Hot Zone’ in the one-dimensional solution. A summary of these values for both the one-dimensional and the current simulation at supply pressure values of 1 MPa and 2 MPa are summarized in Table 6.

Table 6: Comparison of simulation results with one-dimensional solution.

P _{supply} (MPa)	Time-to-Exit of the Shock Front (ms)		Temperature of Hot Zone (°C)	
	Current	One-dimensional	Current	One-dimensional
1	25	25	175 - 250	135
2	20	23	275 - 475	182

It is evident that the current simulation follows the same trends as the one-dimensional solution among all values. While the values of time-to-exit match very closely, there is some discrepancy between hot zone temperature values. The one-dimensional model seems to underestimate all of these values when compared with the one-dimensional model. This can be attributed to the fact that viscous effects are ignored in the one-dimensional model, both of which are contributing factors to heat generation.

A more comprehensive picture of the flow field can be obtained by comparing the simulation results with the one-dimensional solution in a time-space domain. This one-dimensional solution is obtained using the model previously presented in Section 2.2. The case of air as the gas medium with a supply pressure of 2 MPa is selected for this comparison. The results obtained from the current model and the one-dimensional model are shown in Figure 24. Values of gas density are selected for the purpose of comparison since this variable undergoes significant variations.

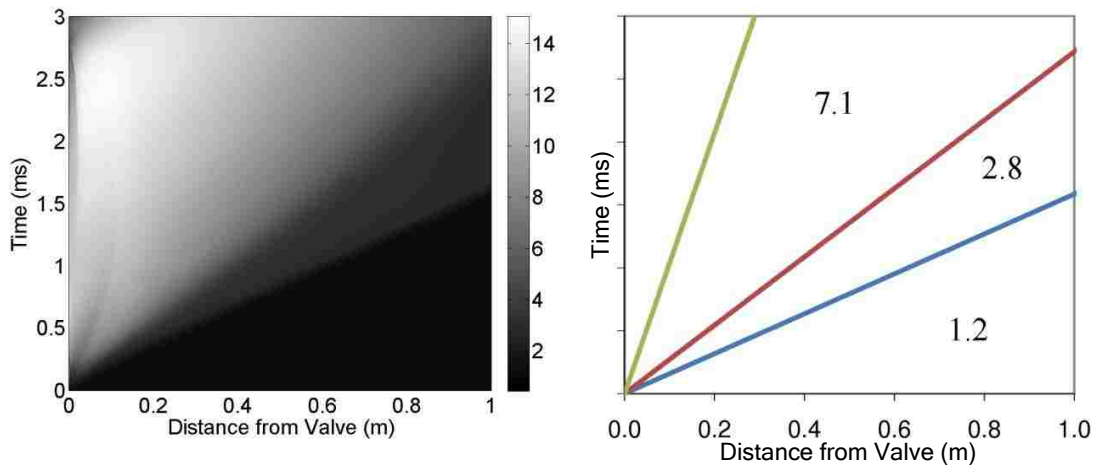


Figure 24: Comparison of density values (in kg/m^3) obtained from current CFD simulation (left) with validated one-dimensional model (right). Air, 2 MPa supply pressure, no heat.

The location of the first line from the bottom in the time-space domain, obtained from the one-dimensional model (in blue), is very closely matched by the CFD simulation. This line represents the shock-wave location. In addition, the values of the fluid density on the two sides of this line (predicted as a constant value of 1.2 and 2.8 before and after the shock-wave passage by the one-dimensional model) closely match in the two solutions.

The second line obtained from the one-dimensional model (in red) represents the contact surface, i.e. the surface that separates the fluid that was initially in the high-pressure zone (that travels as a result of gas expansion) from the one that was in the low-pressure zone (that travels as a result of compression). Between this first line and the second apparent line in the CFD solution the density values are more or less constant. The location of the second line as well as the actual fluid density values on the two sides of this line (predicted as constant values of 2.8 and 7.1 before and after the contact surface respectively) also match between the two solutions. Above this line, however, there is a clear density gradient in the CFD simulation, as opposed to the constant value predicted in the one-dimensional solution. This makes it very difficult to identify the third line (the expansion zone) on the CFD simulation result.

A third line also exists in the image for the one-dimensional solution in Figure 24 (right), that separates zone 3 and zone 4 of the flow shown in Figure 9. This line represents several expansion waves that originate from the valve and are responsible for adjusting flow conditions from zone 4 to zone 3. These waves span over a large area in

space, starting from the contact surface and spreading into the high-pressure reservoir. In effect, these series of expansion waves are the one-dimensional equivalent of a gradual adjustment in flow properties. This gradual adjustment is apparent in Figure 24 (left). Density in the stationary portion of flow in the valve is 23 kg/m^3 .

It is speculated that this discrepancy between the two solutions is due to the 2D effects included in the CFD model. Moreover, the one-dimensional model assumes an abrupt change in properties across an expansion wave, which in reality is not the case. All other identifiable characteristics, however, closely agree between the two solutions. Based on these results, it is hypothesized that the present two-dimensional model reasonably well predicts the flow field inside the spray apparatus and it will be assumed that one can be confident that the two-dimensional model is accurate.

4.2 Stage Two: Representative Gas Flow

The goal of the Stage One of this work was to develop a model to capture basic properties of the flow in a simplified version of the SISP device. This model is verified through numerical experimentation to ensure the flow equations are solved properly. It is also validated, using established one-dimensional results in the literature, to ensure the model is sufficiently capable of predicting the flow. At Stage Two, this model is expanded to model a representative geometry of the device, with complexities added to more accurately represent the device.

4.2.1 Model Conditions

A schematic depiction of the spray device modeled in this stage of the study is shown in Figure 25. The spray tube considered in this stage of the study is generally similar to the previous stage, that is a standard ¼” (6.35 mm) tubing with 0.035” (0.89 mm) wall thickness, resulting in a spray tube internal diameter of approximately 4.6 mm. The total length of this tube is now 2250 mm (compared to 1240 mm at Stage One), which represents the real spray device. Other details of the geometry remain the same. These geometrical parameters of the spray device have already been summarized in Table 2.

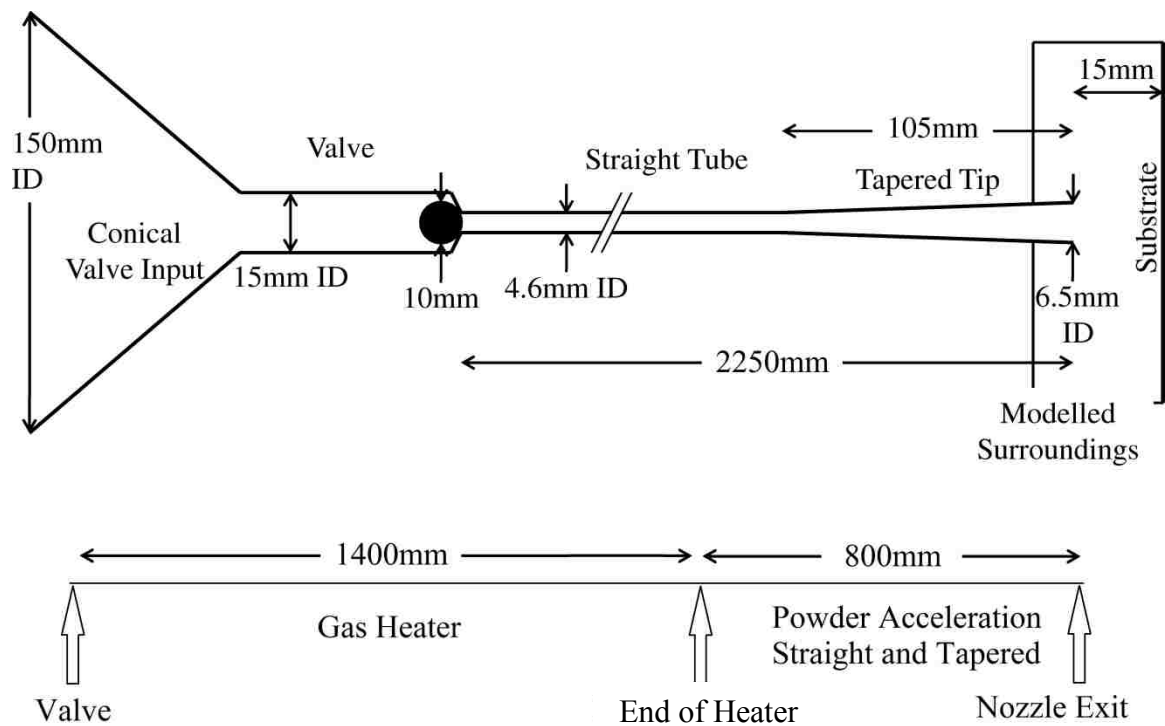


Figure 25: Schematic of the flow region used at Stage Two.

The valve model at this stage represents the rotary type valve used in the spray device today. The design of this rotary valve allows for more accurate estimation of the

motion profile. Based on the motion conditions of the valve, an open and close time of 1.2 ms each, and a fully open duration of 11.1 ms, is used, reflecting the valve motion conditions encountered in the typical spray process.

Additionally, the effect of the gas heater is accounted for in accordance to the physical device, whereby gas heating is achieved by resistively heating a section of the spray tube. A linear profile of temperature variations between the start and the end of the gas heater is imposed as temperature boundary condition on the wall of the heater. The temperature value at the start of the heater is set to room temperature, and to the heater set-point of 550 °C at the exit of the heater.

4.2.2 Model Validation

At this stage a comparison between measurements and model results of the time-history of pressure inside the spray gun is made. These measurements are conducted at two locations along the spray device: immediately downstream of the valve and at the powder feeding location. A piezoelectric pressure transducer, PCB model 113B24, with a rise time of under 1micro-second, is used for capturing pressure values. Data acquisition equipment from National Instruments is utilized in connection with LabView software on a computer workstation. Sampling time for the pressure measurement is 0.1 ms. A Matlab program that was developed for the purpose of extracting and processing time-history data are included in Appendix G. The results of this comparison are shown in Figure 26. One set of experimental measurements is indicated; however, repetition of the experiment yielded indistinguishable curves at the scale presented.

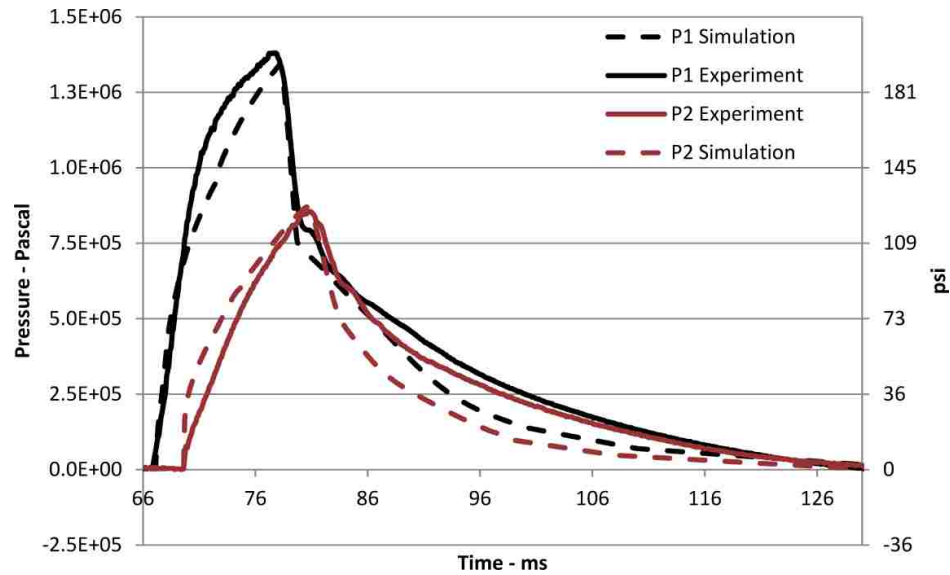


Figure 26: Comparison of time-history of wall pressure at two locations along the spray tube between the experiment and the simulation: 1- immediately after the valve, 2- at the powder injection location.

It appears that many features of the flow are well captured. This includes the time difference between the start of the two occurrences, the value of pressure peak, as well as the rise time to reach the peak. The most pronounced difference between measured and calculated pressure values lies in the rate of pressure decay, where the measured values demonstrate a slower trend. This can be associated with the nature of piezoelectric sensors; while they are very quick to react to a pressure rise their response to decay is slower [61].

A similar plot is shown in Figure 27 where time-history of experimentally measured pressure values is compared with two simulation cases of different valve stroke lengths. One simulation case, denoted 'Initial', represents an initial simulation where valve stroke was 6mm, and the case denoted 'Long Stroke' represents a stroke of 7.2 mm. The details are explained in Section 3.1.2; the plot confirms that the longer valve stroke gives better agreement with measurements.

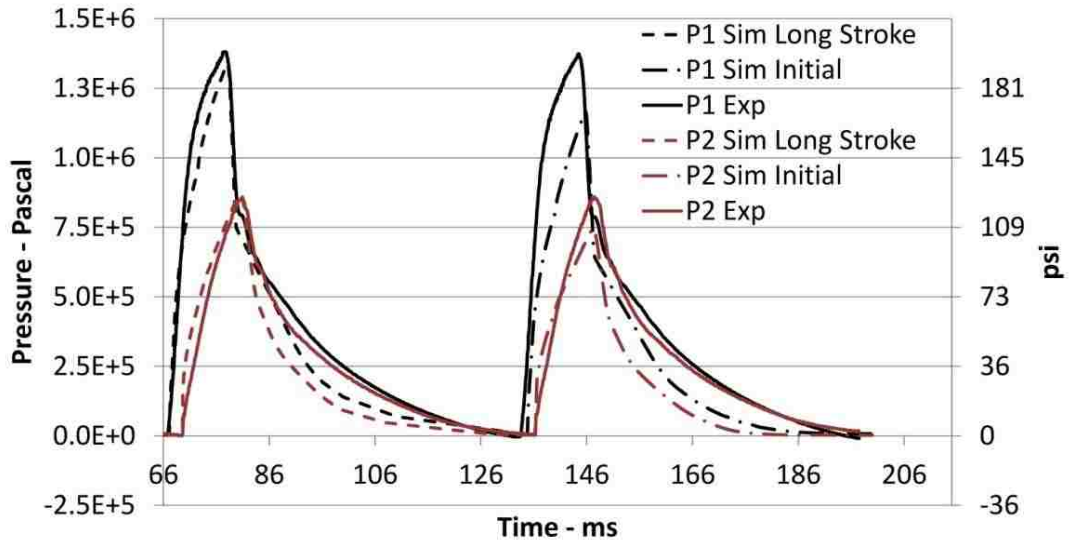


Figure 27: Effect of stroke length on prediction of pressure, and comparison with experimentally measured pressure values.

An attempt was made at measuring temporal variations of temperature at a location of the spray device; the particle feeding location was selected for this purpose. The smallest k-type thermocouple available on the market is one from Omega [62] that is 0.01 mm in diameter. This thermocouple, due to its small size, is extremely difficult to handle. The thermocouple was mounted inside the spray tube and the signal was collected. The resulting measurement, overlaid on predicted temperature values, is shown in Figure 28.

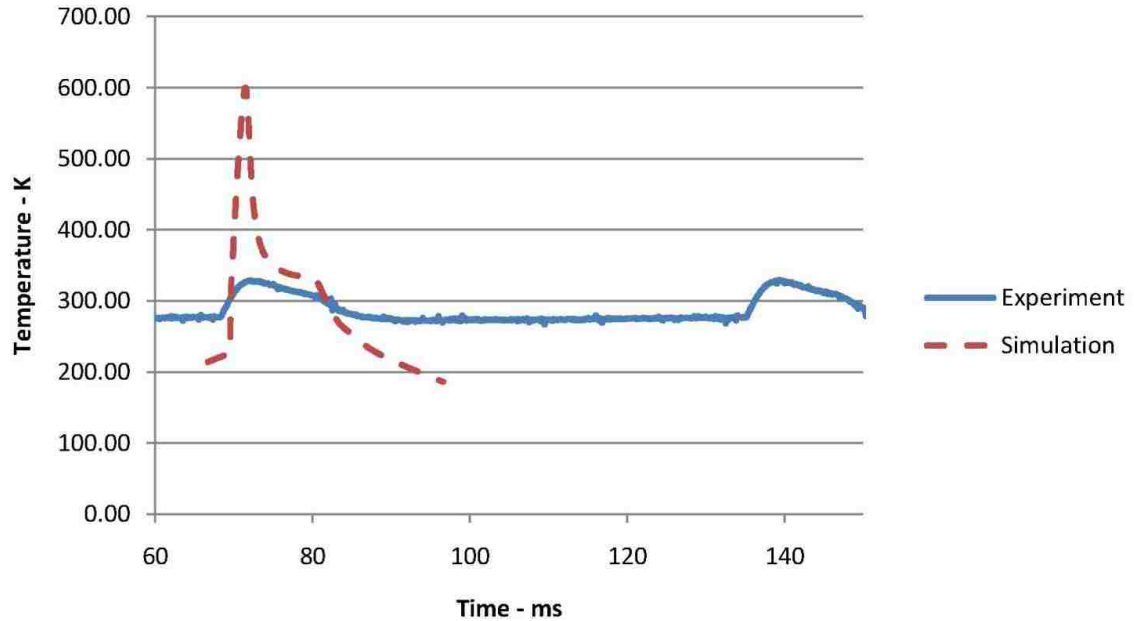


Figure 28: Experimentally measured temperature values overlaid on predictions from the simulation.

Based on relations provided by the manufacturer, and considering the gas speed over the thermocouple, a time constant of approximately 1-4 ms is expected for the thermocouple during the fast temperature rise, and 1-50 ms during the gradual temperature drop. The event takes about 3 ms to the peak, and 40 ms for the gradual drop. Evidently, in both cases the time constant of the thermocouple is in the same order of magnitude as the duration of the event. This indicates that the measurement system is not fast enough to fully capture the details of the signal. However, the fact that a temperature rise is detected upon the passage of the shock-wave validates the basic principle behind the traveling shock-wave phenomenon.

4.3 Stage Three: Discrete Phase

The purpose of this stage of the work is to study the behavior of particulate material in the gas flow. This will enable prediction of particle fate upon impacting the

substrate, that is whether it will adhere and form a coating or not. A mechanism to introduce powder particles into the spray tube is also essential to the process. Using the particle modeling technique it is possible to examine the effect of powder injection scheme on the performance of the device.

4.3.1 Model Conditions

The geometry and flow conditions for the particle simulation study are those used in Stage Two (Figure 25). These reflect working conditions typically used in the operation of the device. The typical injection site is located 1.4 m downstream of the valve as depicted in Figure 29.

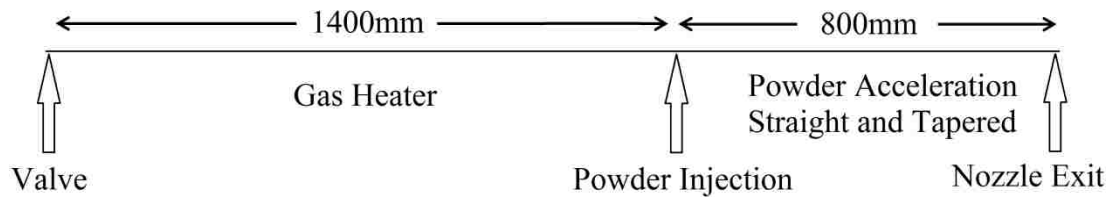


Figure 29: Typical location of particle injection site with reference to the valve and nozzle exit.

4.3.2 Model Validations

In order to validate the discrete phase model, particle velocities at the exit of the device tube are compared between the prediction of the model and measurements. For the purpose of particle velocity measurements, a particle analysis system called DPV2000, developed by Tecnar Inc. (St-Bruno, Quebec, Canada), is used. The device, as shown in Figure 30, is capable of measuring and diagnosing in-flight particles.



Figure 30: DPV-2000 particle analysis device by Tecnar Inc.

The device works based on a photo detector that is covered by two consecutive slits of a distance of 210 microns apart [63]. In thermal spray processes the device detects the radiation emitted from hot particles. For processes where particles are not hot enough to emit sufficient radiation, such as cold spray and SISP, a laser is used to illuminate the particles and generate sufficient scattered radiation. As a particle passes in front of the photo detector, the sensor detects two radiation spikes, one for each slit that sees the particle. The time difference between these two spike events, and the precisely known distance between the two slits of the photo-mask, enable calculation of the particle speed.

The particle speeds for three different types of powder, of spherical shape, are measured by the device. For each case, the mean velocity and the standard deviation of the measurement are calculated, and plotted in Figure 31 for aluminum (top), copper (center) and stainless steel (bottom) particles. Time variations of particle velocities with respect to their injection time is illustrated. A Matlab program and relevant functions that were developed for this purpose are included in Appendix H. For the measurements, a

particle size distribution narrowed to a range of 25-38 microns is used. Numerical results pertaining to the particle sizes of 20 microns and 40 microns are plotted. It is evident in all three cases of materials that the calculated values fall well within, or in a close range of those measured in the experiments.

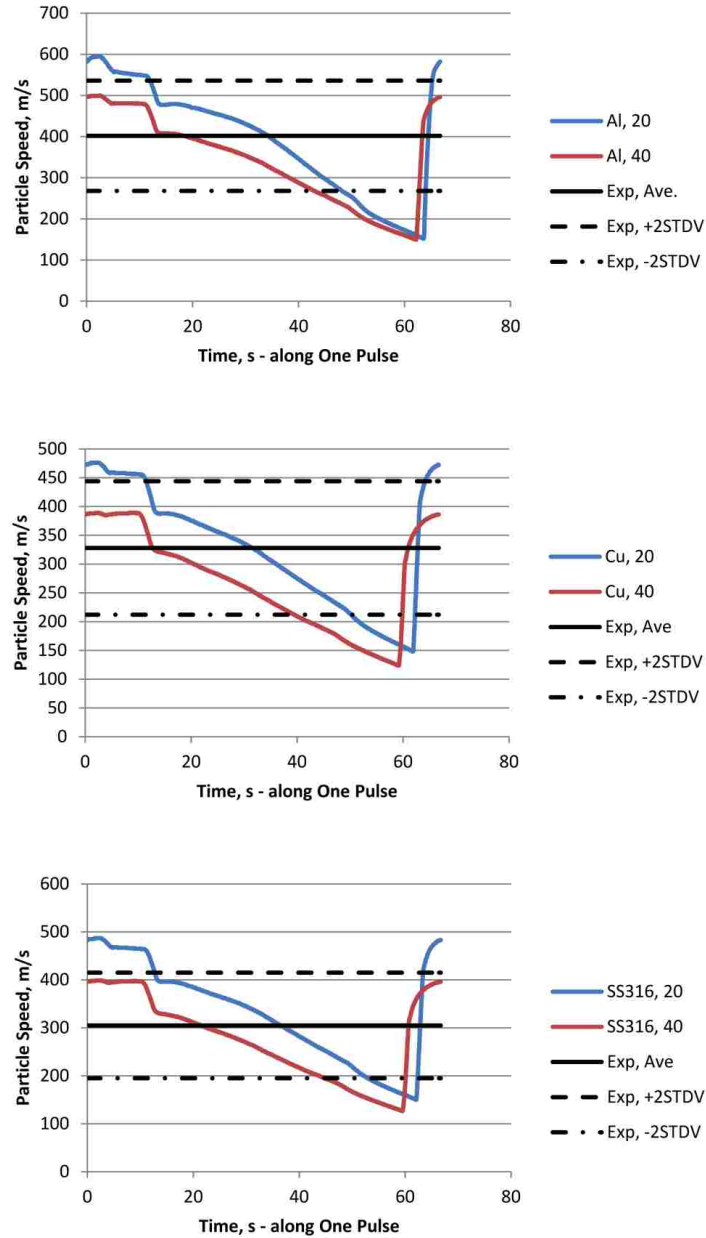


Figure 31: Comparison of measured and calculated particle speed at the exit of the SISF device for aluminum (top), copper (center) and stainless steel 316 (bottom) particles.

Chapter 5. Results and Discussion

The results of the study are presented in this chapter. The chapter is divided into three sections to present the results from the three stages of the study. First, the results of ‘Stage One: Generic Gas Flow’ as described in Section 4.1, are presented. In this case a simplified model is used to study the general effects of pressure, temperature and gas type on the flow field. In the next section results of gas flow for a set of realistic operating conditions as described in Section 4.2, ‘Stage 2: Representative Gas Flow’, are presented. Differences with the results of Stage One due to improved simulation conditions are highlighted. In the third section of this chapter results of the discrete phase modeling as described in Section 4.3, ‘Stage Three: Discrete Phase’, are presented.

5.1 Stage One: Gas Phase - Simplified Model

The quantities of particular interest to this study are the flow local temperature and velocity. The total temperature, which is essentially a representation of the kinetic as well as internal energy of the flow, is also of interest. This is due to the fact that it is important to simultaneously bring the powder particles to an elevated level of thermal and kinetic energy for a successful spray process. Finally, in order to fully understand the flow behaviour and the effect of the parameters of interest on the flow regime, local pressure and the Mach number are also studied in detail.

5.1.1 Effect of Gas Supply Pressure and Temperature

The effects of the gas supply pressure and preheating temperature are considered first. In all of these simulations the gas media is air. Each set of results consists of three images; the first image corresponds to the conditions of 1 MPa and 23 °C supply gas, followed by 2 MPa and 23 °C for the second image and 2 MPa and 300 °C for the last image.

The effect of supply pressure and temperature on the pressure field is shown in Figure 32. Note the inclined line near the bottom of each figure that separates the initial stagnant flow from the accelerated flow with a sharp change in color on its two sides. This line represents the location of the travelling shock-wave in the space-time domain, and its slope represents the speed of this feature (the closer to the horizontal direction the faster the shock-wave is travelling). It is observed that increasing the supply gas pressure from 1 MPa (left) to 2 MPa (middle) will slightly increase the travelling shock-wave speed. By operating the device at an elevated temperature of 300 °C (right) versus ambient temperature (middle), the most important visible effect is an increase in the propagation speed of the shock-wave and of the resulting flow pressure throughout the space-time domain.

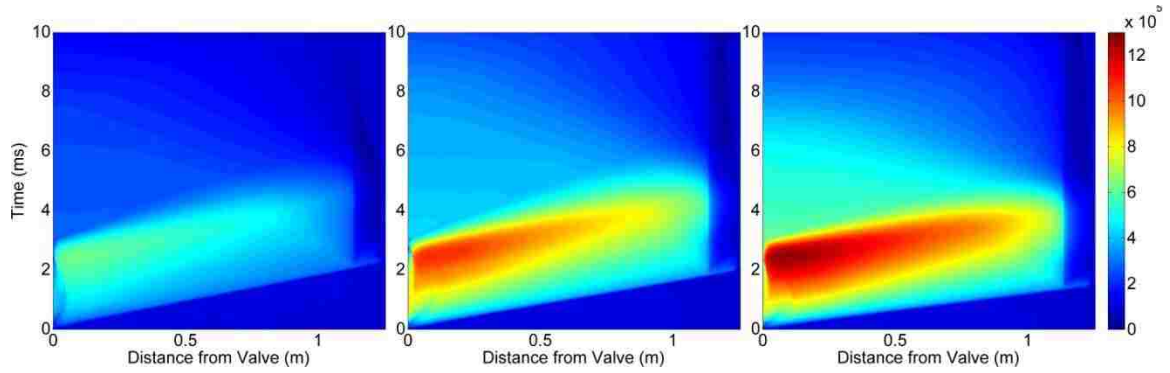


Figure 32: Effect of supply pressure and temperature on static pressure (Pa). Supply temperature and pressure values of ambient and 1 MPa (left), ambient and 2 MPa (middle) and 300 °C and 2 MPa (right).

Contours of Mach number are examined next, as shown in Figure 33. The contours of Mach number look quite similar, in appearance and magnitude, when gas supply temperature is varied. These observations are in very good agreement with the simplified one-dimensional theory [21].

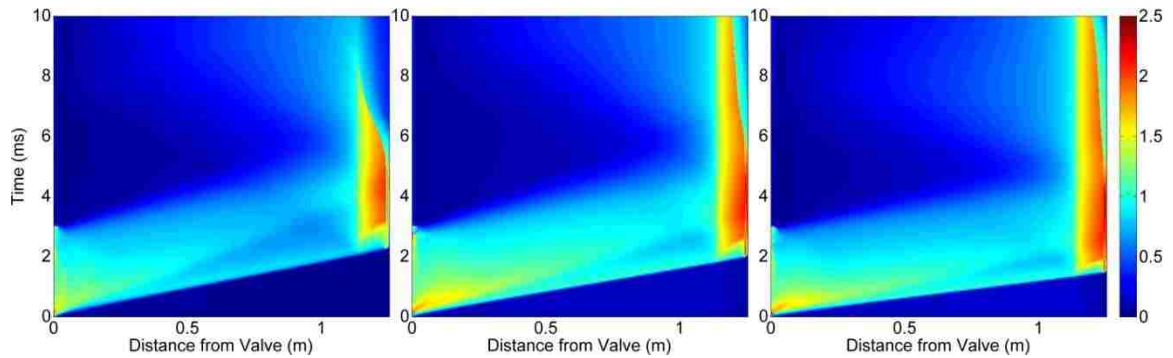


Figure 33: Effect of supply pressure and temperature on Mach number. Supply temperature and pressure values of ambient and 1 MPa (left), ambient and 2 MPa (middle) and 300 °C and 2 MPa (right).

In fact, in the one-dimensional formulation (presented in Equations 1-4), the value of the flow Mach number immediately trailing the travelling shock-wave is a strong function of pressure ratio, and a weak function of process temperature. If temperature in zone 4 is assumed to be equal to zone 1, which is a realistic assumption, according to

Equation 1 the pressure in zone 2 will only be a function of supply pressure. Subsequently, according to Equations 2 and 3, temperature and density in zone 2 will also only be a function of supply pressure. If both sides of Equation 4 are divided by c_2 one can see that Mach number in zone 2 is also independent of supply temperature and only depends on supply pressure. These relations are utilized to investigate the effect of supply pressure and temperature on gas speed and Mach number in zone 2, and the results are shown in Figure 34.

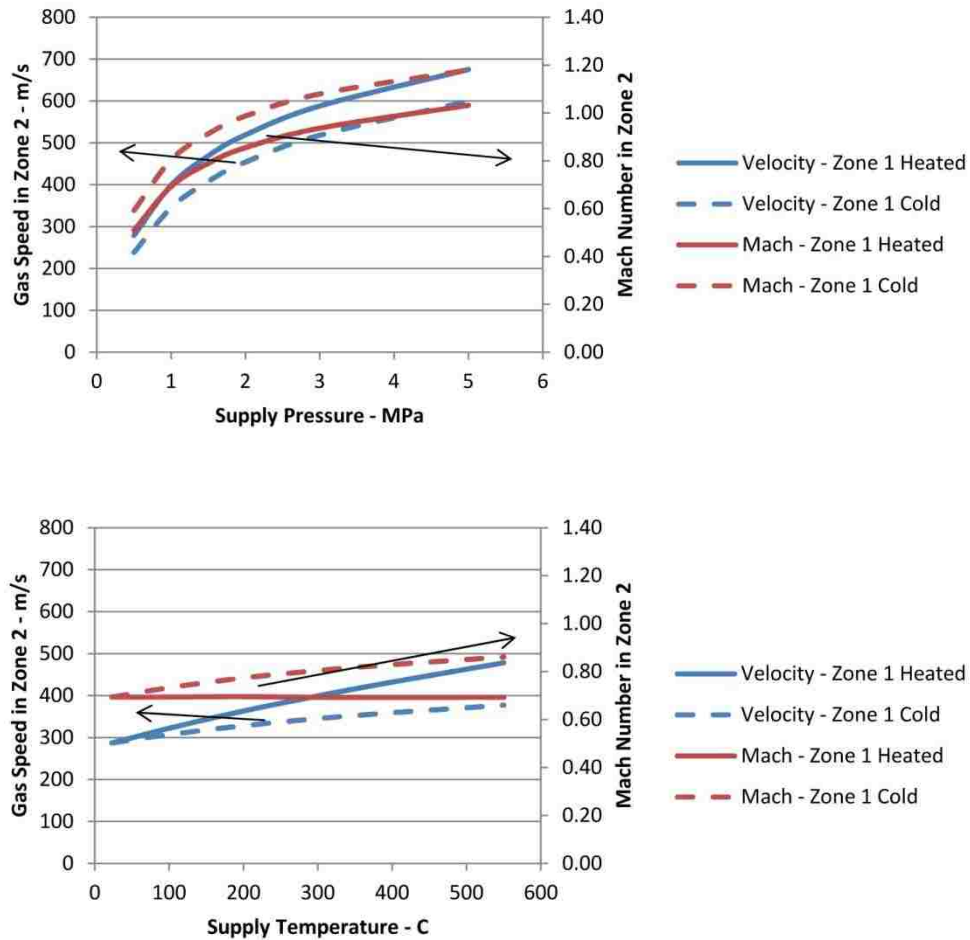


Figure 34: Effect of supply pressure (top) and temperature (bottom) on gas speed and Mach number in zone 2, with the assumption of fully-recovered temperature and no temperature recovery in the tube after the passage of the shock-wave.

For the case of air, if an infinitely large pressure ratio is used, the one-dimensional theory predicts that Mach number would approach a value of 1.9. As shown in Figure 33 and Figure 34, Mach number in zone 2 remains below this level over a range of supply pressures and temperatures. Near the valve (Figure 33) Mach number holds its maximum value, and in the case of the simulation results this high value of Mach number quickly diminishes due to frictional effects as the wave travels along the tube, which is not accounted for in the one-dimensional model. Another interesting attribute of these contours is when higher pressure is used, this diminishing effect occurs at a much slower pace than when lower pressure is used. This indicates that it is possible to sustain a higher Mach number over a longer portion of the tube by increasing the supply pressure.

The next important flow feature to be considered is the axial velocity. Particle velocity is directly related to this quantity, which along with particle impact temperature are the two major factors determining the success of the spray process. Contours of axial velocity of the gas under the three conditions specified previously are shown in Figure 35. The location of the traveling shock-wave in the space-time domain is visible as an inclined line at the bottom of each contour and demonstrates a sharp change in color on its two sides. This location is the same between these contours (all the three) and contours of pressure as shown previously in Figure 32.

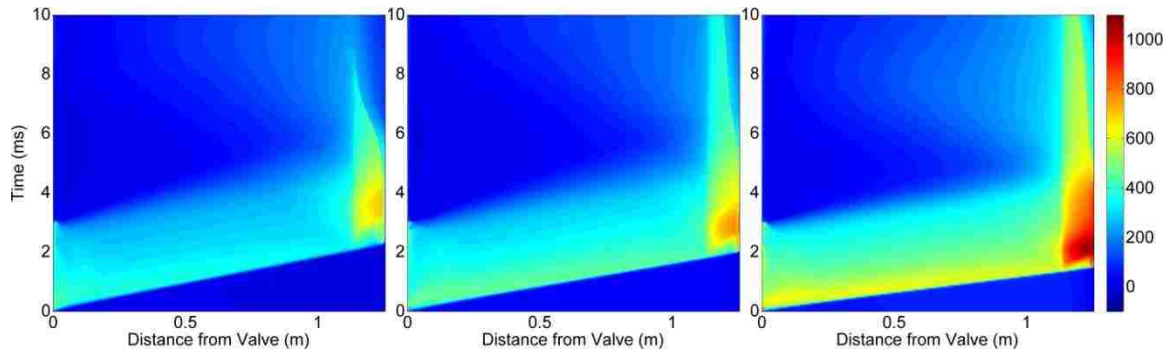


Figure 35: Effect of supply pressure and temperature on axial velocity (m/s). Supply temperature and pressure values of ambient and 1 MPa (left), ambient and 2 MPa (middle) and 300 °C and 2 MPa (right).

Beyond a certain length it is expected that the kinetic energy of the shock-wave, reflected in the flow axial velocity behind the shock-wave, will start to deteriorate as a result of wall friction and viscous dissipation effects. This phenomenon is most visible in Figure 35 (left). Moreover, in all cases, at each location (for example take the contour to the right at location 0.5 m on x-axis), as time passes ($4\text{ms} < t < 10\text{ms}$) some oscillation in the value of axial velocity is observed. There is a sharp rise when the shock-wave arrives, to a value of approximately 700 m/s, then it settles to a value of approximately 400 m/s. As a result of the valve closing, this value suddenly drops to levels near zero; however this is followed by another slight increase in velocity, which is a result of the reflection of the expansion wave from the end of the nozzle.

The trend shows a slight increase in maximum flow speed due to increased pressure (approximately 710 m/s and 790 m/s at 1 MPa and 2 MPa respectively), however a high-speed zone forming in the tapered nozzle tip and in the surroundings lasts a significantly longer time in the case of increased supply pressure. When a higher pressure is used, a greater mass of gas will enter the tube initially. However, since flow

speed remains the same, it takes a longer time to discharge all of the gas from the tube when higher pressure is used.

An increase in the temperature of supply gas, on the other hand, is accompanied by a more significant increase in gas velocity. This is evident both inside the straight nozzle tube as well as in the tapered portion and surroundings. This is because an increase in temperature makes more energy available to the gas stream that can be translated into kinetic energy. Additionally, the dependence of the speed of sound on temperature contributes to this. An increase in temperature results in an increase value of speed of sound, and even under equal Mach regimes a gas of higher temperature will demonstrate higher gas speed. The portion of the high-speed flow that occurs in the tapered nozzle tip and surroundings lasts nearly as long in time as that observed in the no-heat arrangement.

Contours of static temperature for the three cases studied are shown in Figure 36. The location of the traveling shock-wave and the effect of the two parameters on the speed of this feature can again be clearly seen and the same conclusion drawn. The main significance of these contours, however, lies in the formation of a high-temperature zone in all cases trailing immediately after the traveling shock-wave. A rise in temperature of approximately 300 °C is observed in this zone compared to the temperature of the supply gas. As time passes and the fluid travels along the tube, this region demonstrates two interesting attributes. Firstly, the maximum gas temperature in this region tends to increase, and this increased temperature zone tends to stretch in space. This hints that by

using a longer tube it is possible to achieve a zone of elevated temperature that is longer. Practically, it is not possible to extend the tube indefinitely.

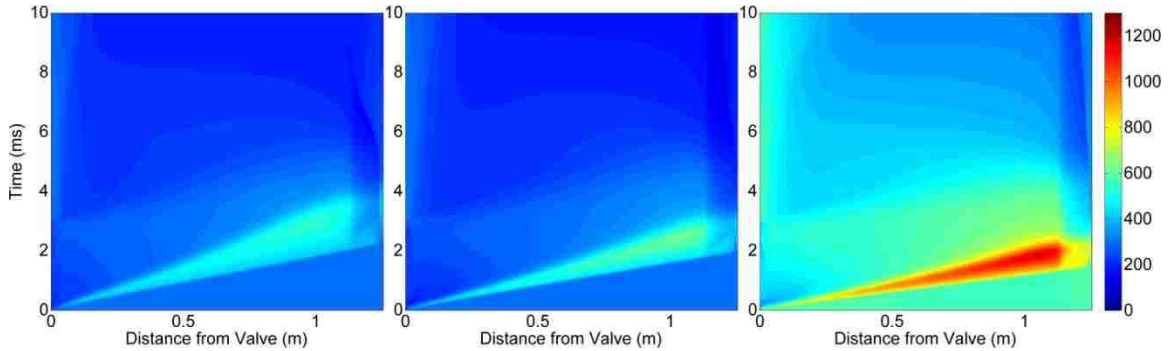


Figure 36: Effect of supply pressure and temperature on static temperature (K). Supply temperature and pressure values of ambient and 1 MPa (left), ambient and 2 MPa (middle) and 300 °C and 2 MPa (right).

In these contours, gas temperature in the device prior to the advent of the shock-wave is not at ambient room conditions. Neither this initial value is a reflection of the evolution of the flow conditions towards the end of the pulse. In fact, the results at this stage are calculated for a single isolated pulse, therefore the conditions at time zero are the initial solution used to start the transient solution. This solution is arrived at through solving the flow field with the valve closed. In obtaining the initial steady-state solution, the valve presents a small leak. As a result, hot gas leaks from the valve into the ambient after passing through the tube. This small flow travels very slowly and results in negligible change in gas velocity or pressure. However, it is of a high temperature and causes a temperature increase in the tube. This is reflected in the temperature of the gas in the tube prior to advent of the shock-wave being equal to the reservoir inlet temperature boundary condition. This phenomenon is in fact an accurate representation of reality. A leaking valve connected to a tube open to atmosphere will transmit the temperature to the tube, however will not cause a considerable pressure or velocity rise in the tube.

A comparison with the contours of axial velocity shows that this region also experiences a high speed. This is the feature that sets this spray method apart from its steady counterparts. In steady-state cold spray methods, the main focus is on the velocity of the gas medium, and a rise in gas velocity is always accompanied by a drop in flow temperature according to the basic principles of energy conservation in steady-state processes. In this situation, however, as a result of the unsteady nature of the flow, an opportunity arises where elevated levels of temperature and velocity co-exist in the flow. The region in the flow that attains this elevated level of temperature and velocity is bound by the shock-wave and the contact surface. Prior to the exit of the high-pressure gas from the reservoir, this region was stationary in the tube. The initiation of the gas pulse compresses this stationary gas, which causes it to heat. The approaching gas pulse also accelerates the previously stationary gas to high velocities at the same time. The energy required for these simultaneous actions originates from the energy stored in the pressurized gas reservoir. Although this opportunity lasts a short time (only a few milliseconds), it can be enough to bring powder particles of proper size and shape to internal energy levels that are not achievable in traditional cold spray methods.

The unique feature of this process can be further explored by examining contours of total temperature. This quantity is defined as the temperature of the flow when it is brought to a zero velocity with no heat transfer. Contours of total temperature under the three conditions studied are shown in Figure 37. It is observed from these contours that a

zone of elevated energy content forms just after the traveling shock-wave. This unique feature of the pulsing flow is ideal for use in a kinetic spray process.

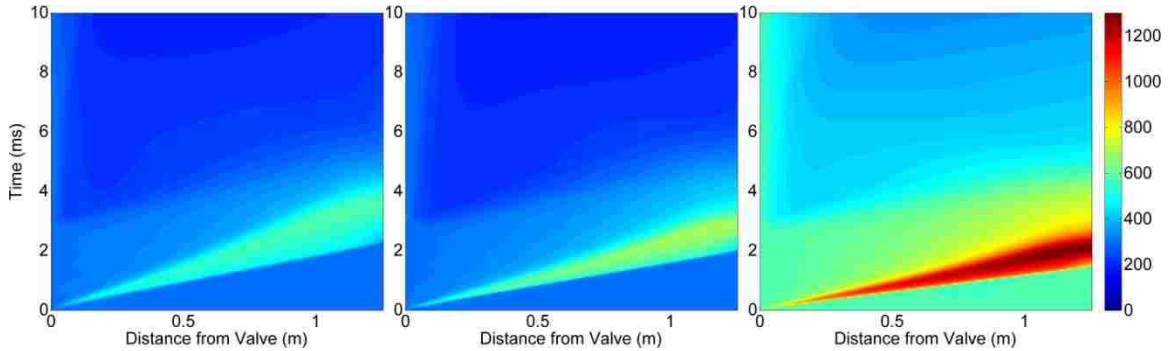


Figure 37: Effect of supply pressure and temperature on total temperature (K). Supply temperature and pressure values of ambient and 1 MPa (left), ambient and 2 MPa (middle) and 300 °C and 2 MPa (right).

5.1.2 Effect of Gas Type

A similar comparison is conducted to observe the effect of gas type on various flow characteristics. The case of air at 2 MPa and 300 °C for supply conditions is compared with helium as the medium at the same supply conditions.

Contours of static pressure are shown in Figure 38 for the two cases. It is observed that flow features (for example the moving shock-wave) propagate faster in a helium environment. The traveling shock-wave has a significantly higher speed in helium than in air (1520 m/s and 610 m/s for helium and air respectively). This is reflected in the slope of the line that represents the location of the shock-wave in space-time domain. Additionally, time variations of pressure in the area near the valve during the period of the valve being open are significantly steeper in helium than air. All these observations are attributed to the fact that the speed of sound in helium is more than two times larger

than in air. This characteristic governs the speed at which all other flow features propagate in a medium.

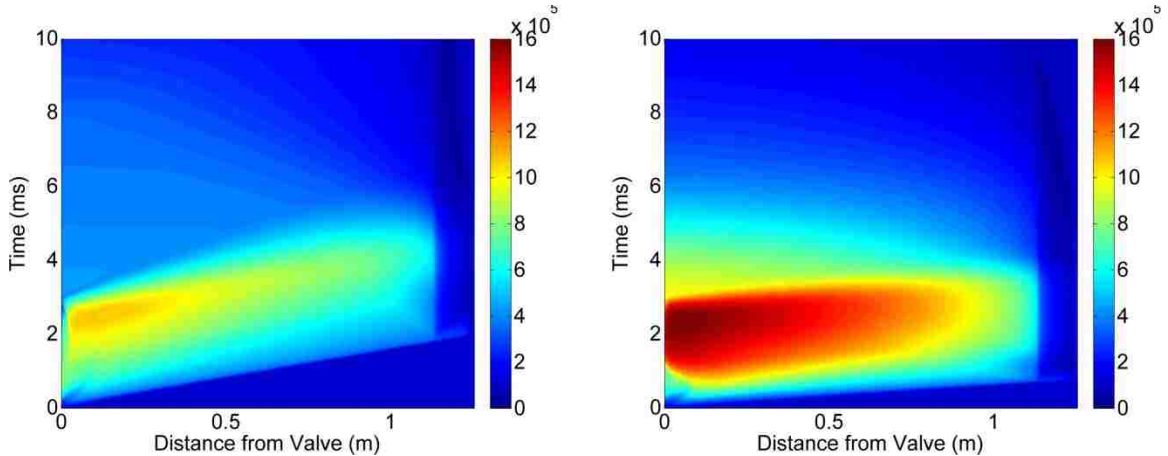


Figure 38: Effect of gas type on static pressure (Pa). Gas type of air (left) and helium (right).

Another interesting observation from a comparison of these two contours is the fact that pressure in the spray tube reaches significantly higher values when helium is used compared to air. This is directly related to the propagation speed of features in the two media as a result of a difference in the sound speed. In helium, speed of sound is nearly three times that of air, and subsequently pressure increase in the tube occurs at a rate nearly three times faster than in helium. Therefore within the same given valve open time, pressure in helium reaches greater values than that in air. For a more direct comparison, one may visually compare pressure value in the helium tube at 1 ms with that of the air tube at 3 ms; they are quite comparable.

Contours of axial velocity are shown in Figure 39. These images present the fact that flow speed is significantly greater when helium is used. Throughout the straight spray section, a significant difference in shock-induced velocity is observed between the

two cases, showing a velocity of approximately 460m/s for air versus 1130m/s in the case of helium. A similar ratio holds for the maximum value of the axial velocity, with that of helium reaching approximately 2400m/s versus 770m/s for air. This is in agreement with one-dimensional predictions, as expressed in Equation 4.

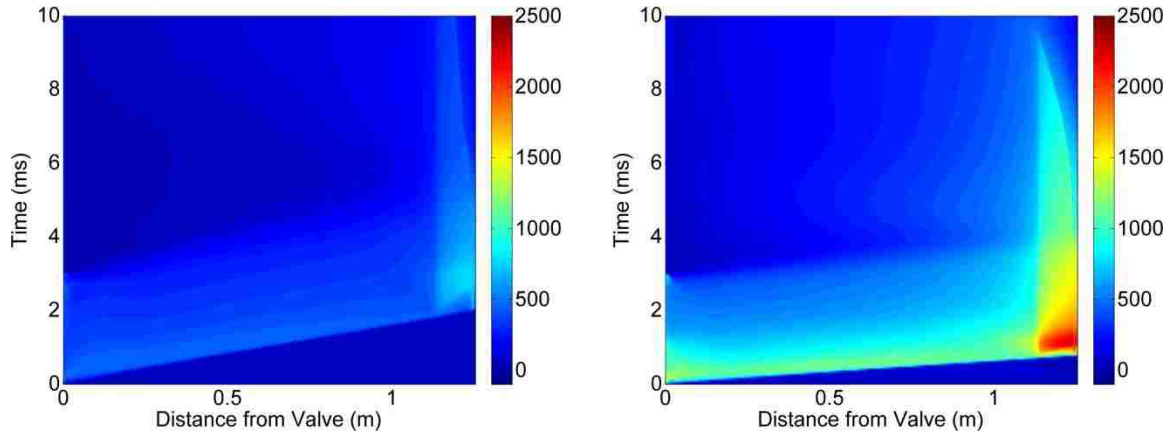


Figure 39: Effect of gas type on axial velocity (m/s). Gas type of air (left) and helium (right).

Effect of gas type on the value of Mach number is shown in Figure 40. Interestingly, these images look more or less alike especially when the range of the values of Mach number is considered. This further verifies that the higher values of axial velocity found with helium can be attributed to the very high speed of sound in this medium. While the general trends are very similar, the image corresponding to helium looks compacted in the time domain, suggesting a faster propagation of flow features in helium.

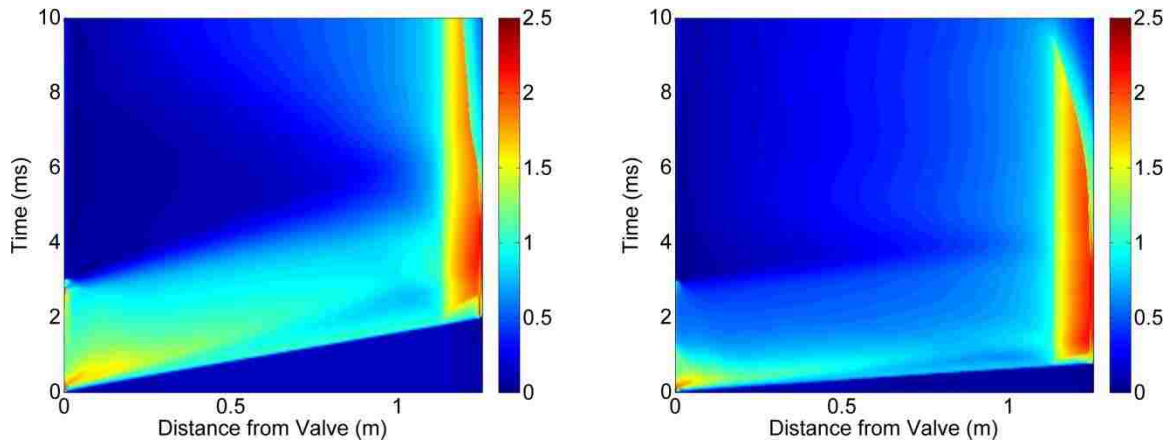


Figure 40: Effect of gas type on Mach number. Gas type of air (left) and helium (right).

Contours of static temperature are shown in Figure 41. Similar to the case of other variables, all features of this contour are also compacted in time as a result of the higher speed of sound in helium, further suggesting a faster propagation of flow features in helium. Although the two contours are generally the same, the maximum temperature in the case of helium is somewhat higher than in the case of air (900°C and 700°C in helium and air respectively). As previously observed, as the flow travels along the tube, the maximum gas temperature tends to increase. Due to a higher value of specific heat ratio, γ , for helium than air, and with reference to Equation 2, theoretical value of temperature in zone 2 for helium is greater than that of air. Moreover, similar to all other features of the flow, the increase in temperature occurs at a more rapid rate for helium than air. Therefore in the simulation results helium is observed to show a higher maximum temperature than air.

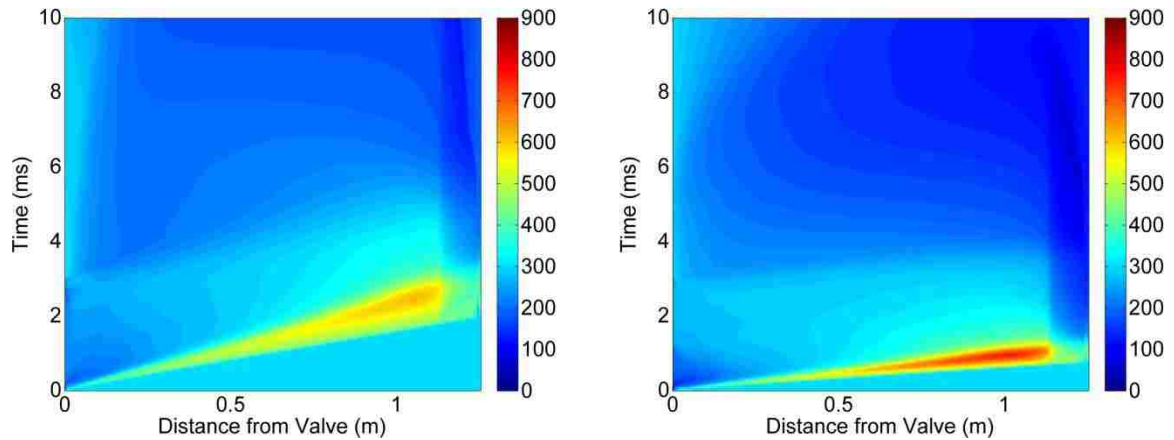


Figure 41: Effect of gas type on static temperature (K). Gas type of air (left) and helium (right).

Additionally, the region where elevated temperature is present lasts a shorter time in the case of helium (0.75ms and 1.51ms for helium and air respectively). This is due to the faster propagation of features in helium than air as a result of the difference in sound speed. This fact makes it more challenging to utilize this zone of elevated temperature for the practical purpose of spraying materials when helium is used as the propelling gas.

Finally, the effect of gas type on total temperature is presented in Figure 42. It can be concluded that a higher level of total temperature is attainable by using helium. This will potentially translate to better results with helium when this device is utilized for the purpose of applying coatings. It is notable, however, that the area of elevated energy levels is compacted in time with helium compared to air, possibly making it a bigger challenge to utilize this gas in an actual spray device.

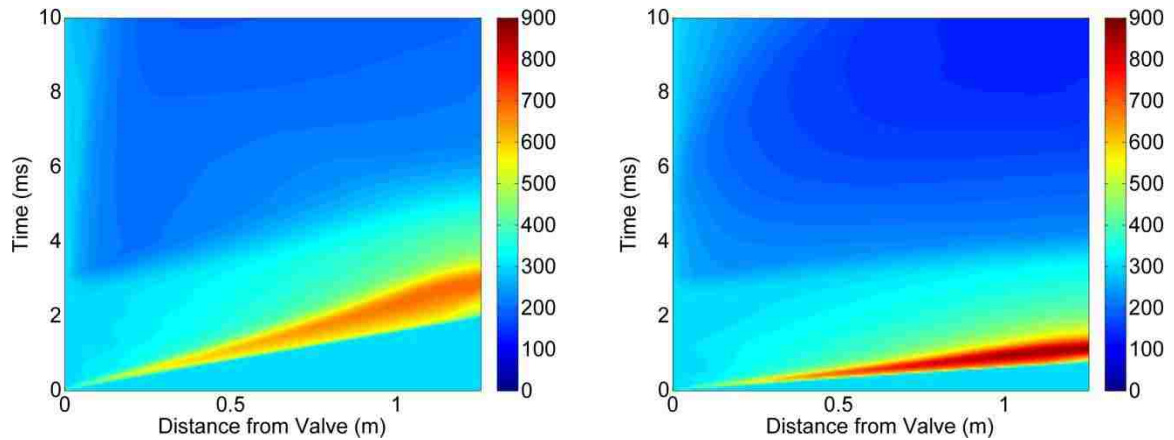


Figure 42: Effect of gas type on total temperature (K). Gas type of air (left) and helium (right).

5.1.3 Summary of Stage One: Gas Phase - Simplified Model

A CFD model was successfully developed and used in order to simulate the Shock-wave Induced Spraying Process. Considering the unsteady nature of the flow, the usual space domain that is commonly used for plotting flow variables is replaced by a space-time domain with contour colors determined by flow variable values. Using a geometry that generally resembles that proposed for the process, the underlying physical principles of the process were explored.

It was found that due to the unsteady nature of the process, it is possible to form an area in the flow where both velocity and temperature are simultaneously elevated. This is a very important feature of the flow that is unique to this process and sets it apart from its steady counterparts (traditional cold spray methods). In steady-state cold spray processes, the main focus is on the velocity of the flow as well as powder particles, which is often achieved at the expense of thermal energy. A region that simultaneously has high thermal and kinetic energy content exists in the flow field. It is envisioned that it would

be possible to utilize this unique feature by correctly injecting powder particles in a way so that they would stay in this zone for a sufficient portion of their flight period to impact on the substrate at energy levels higher than steady-state cold spray methods.

Also important is the finding that this zone of elevated energy level elongates as the flow evolves in time and distance along the tube. This means that by selecting a longer tube it is possible to increase the opportunity for the particles to stay within this zone for most of their flight. It should be noted that there is a limit to this, if the tube is extended too long the strength of the shock-wave will start to dissipate. Therefore its speed and total energy content will be diminished.

It was found that increasing process pressure causes a region of elevated gas speed to last longer in time. Increasing the process temperature, however, will result in increasing the energy content of the flow by increasing its temperature as well as velocity. The increase in velocity is a result of a higher speed of sound due to the increased temperature, since Mach number profiles remain largely unaffected.

The effect of gas type on the flow field was found to be mainly driven by the speed of sound in the medium. When helium is used, all flow features propagate significantly faster than when air is used. The pressure builds up in the tube much faster and the shock-wave reaches a higher speed. For the same reason, the region of elevated energy also tends to dissipate faster. This shows that although use of helium can result in

a higher velocity for the powder particles, realizing this potential could demand a more careful tuning of the process.

This model agrees well with an existing one-dimensional model in predicting major characteristics of the flow, however it offers several advantages. Firstly, the one-dimensional model divides the flow into a few zones and approximates all flow variables with one value in each zone. This ignores many details of the flow that are captured using this CFD model. Additionally, it only considers the propagation of features initiating from the valve. Although these are the most dominant effects, there are features that initiate elsewhere in the flow. For example, the in-line heating that occurs along the device tube prior to powder injection is not accounted for through the one-dimensional model. It is also limited in accounting for a tapered portion at the tip of the tube as well as the effects of the tube exit and a substrate. Additionally, the preceding one-dimensional model can only predict the opening of the valve, not its closing. The CFD model described here is a more accurate representation of the flow, accounting for turbulence effects, wall friction, viscous dissipation, gas heating, and complete valve opening and closing cycle. Additionally, it is capable of capturing the two-dimensional effects in the surroundings outside of the nozzle, although not of the interest of this study.

5.2 Stage Two: Gas Phase - Representative Geometry

The results of Stage Two is presented here. At this stage SISP is modeled in great detail, with the valve motion profile and heater temperature distribution implemented. This simulation is conducted in a geometry that is representative of a typical spray

device. The overall length of the tube is now 2.25 m compared to 1.24 m in Stage One. As mentioned in Section 4.2, the conditions of this simulation are at a pressure and temperature value of 2 MPa and 550 °C, a frequency of 15 Hz, valve open and close time of 1.2 ms each, and a fully open duration of 11.1 ms.

5.2.1 Results of Stage Two: Gas Phase - Representative Geometry

In order to explain the gas dynamics of the process in the representative geometry, the results of the simulation for the gas phase in a typical device are first shown in a time-space domain. As described previously, values of each flow variable at each location of the spray device centerline are plotted. The plot corresponding to pressure is shown in Figure 43 (a). This image corresponds to the operating conditions previously mentioned.

In this plot, similar to the previous ones, the extent of the space domain starts from the valve exit and stretches to the substrate. The locations of the start of the tapered section as well as the nozzle exit are shown by two arrows. One shall note how close the nozzle exit is located with respect to the substrate when compared to the total length of the tube; this distance is only 15 mm compared to the overall tube length of 2250 mm. The location of the traveling shock-wave that occurs as a result of fast opening and closing of the valve is also identified.

Contours of axial velocity, temperature and total temperature are plotted in Figure 43 (b) through (d). The locus of the travelling shock-wave can be clearly identified in all these images. Under these realistic conditions it is also evident that a region forms in the gas flow, just after the passage of the shock-wave, which possesses a high gas speed as

well as a high temperature. This is re-iterated in the contour of total temperature. For SISP to be successful, it is desired that powder particles travel in this region for as long as possible.

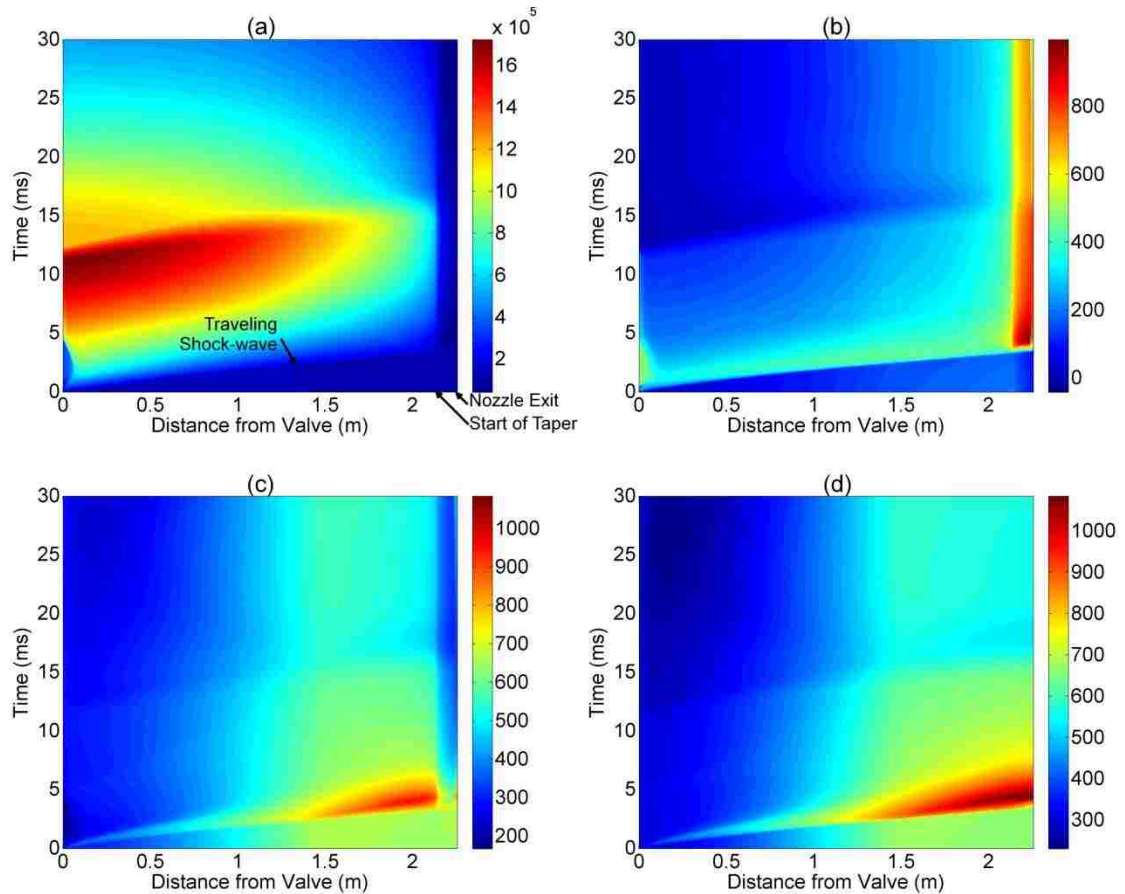


Figure 43: Contours of (a) pressure (Pa), (b) axial velocity (m/s), (c) temperature (K) and (d) total temperature (K) for a typical spray device.

A comparison between results of the Stage One and Stage Two of the study reveals noteworthy observations. In order to facilitate this comparison, the results of Stage Two and Stage One are broken down and placed side by side in Figure 44. Contours of Stage Two are placed on the left, and those of Stage One are placed on the right.

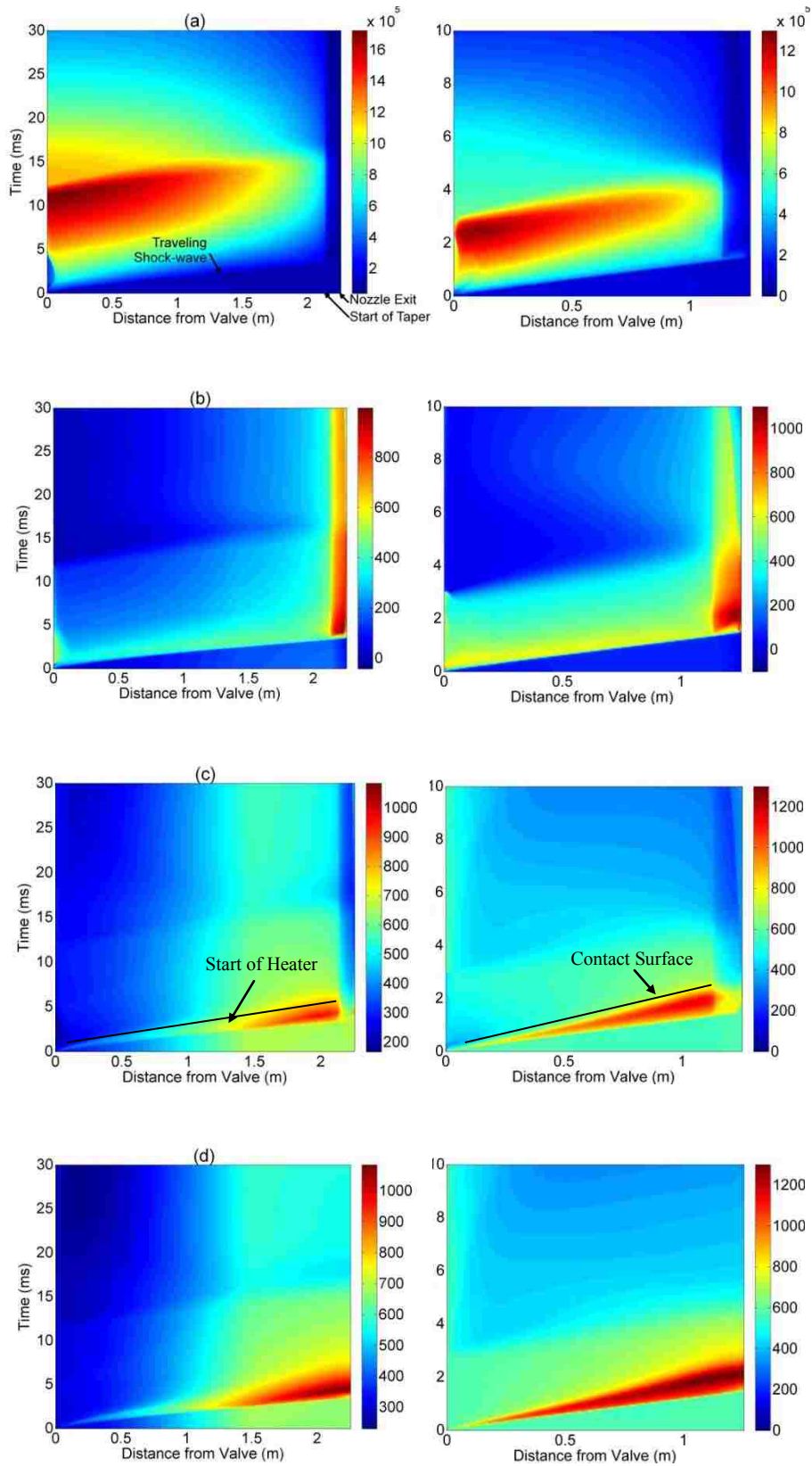


Figure 44: Contours of (a) pressure (Pa), (b) axial velocity (m/s), (c) temperature (K) and (d) total temperature (K) from Stage Two (left) and Stage One (right).

A comparison of static pressure results shows that valve opening time has a significant effect on the build-up of pressure in the spray device. In fact gas pressure continues to build up in the device while the valve remains open, for all the 12 ms open-time of the valve, in Stage Two. As soon as the valve closes an expansion wave propagates along the tube that reduces the pressure back to atmospheric level. The length of valve open time directly correlates to gas usage in the process.

From a comparison of axial velocities, it is observed that the duration of valve opening has little impact on propagation of the traveling shock-wave. In fact, per one-dimensional model, formation of various zones in the flow are predicted only by the knowledge of the valve opening. The distinct velocity gradient across the shock-wave stretches along the device well through to the exit of the device, in both Stage One and Stage Two. This suggests that the increased length of the device is not yet sufficient to lead to the deterioration of the shock-wave.

Figure 44 (c) can be used to demonstrate effect of the in-line heater on the flow behavior. Firstly, in both cases a second line can be identified crossing the origin that more-or-less bounds the region of elevated temperature. This, called the Contact Surface in one-dimensional flow theory, identified in Figure 44 (c), is the upper bound of zone 2 of the flow. In the case of an insulated device this region maintains a relatively constant temperature along the length of the device tube. For the case of an in-line heater this temperature clearly elevates when following the contour length-wise, beginning at the start of the heated portion of the tube (approximately 1.4 m).

5.2.2 Summary of Stage Two: Gas Phase - Representative Geometry

A model which can be used to simulate the SISP is developed and presented. The model deals with the transient nature of the flow and builds on the Stage One model by accounting for valve opening and closing and gas heating. Finally, presenting a realistic device geometry, it offers great flexibility for conducting subsequent particle tracking calculations throughout the domain.

It is observed from the results that a 12-ms valve on-time results in greater values of pressure in the device. A device of 2.25 m in length will not result in a significant deterioration of the traveling shock-wave, as reflected in axial velocity results. Presence of the device heater translates to a significant increase in gas temperature in the device, in the region of the device heater.

5.3 Stage Three: Discrete Phase

The next step in this work is to use the model in order to predict the behaviour of powder particles in the flow. The details of this step were previously described in Sections 3.2 and 4.3. Using this step it is possible to determine the temperature and speed of powder particles upon impacting the substrate. This knowledge can be utilized for devising a targeted powder feeding strategy to ensure particles will land on the substrate with maximum speed and temperature, an indication that they passed through the area of elevated flow energy.

5.3.1 Presentation of Results

A method is developed to represent the results of particle tracking where a graph is created, similar to that used in the gas dynamic study. In this case, however, the horizontal axis represents the axial location of particle initial injection point along the tube length, the vertical axis represents the time during a pulse at which the particle was injected at that specific location, while the color represents the magnitude of a particle characteristic (namely velocity or temperature) as it impacts on the substrate. The Matlab program and relevant functions that were developed for this purpose are included in Appendix H.

An example is shown in Figure 45 (a) for impact velocity of stainless steel 316 particles of 20-micron size. For example, one can deduce that for a particle injected at 1.5m from the valve and within the first 10 milliseconds of its opening, it will achieve an impact speed of above 450 m/s (marked 1), whereas one that is injected at 50 ms will reach less than 250 m/s (marked 2). A similar image for the temperature is shown in Figure 45 (b). Using these two contours one is able to predict the fate of each particle in the space-time domain.

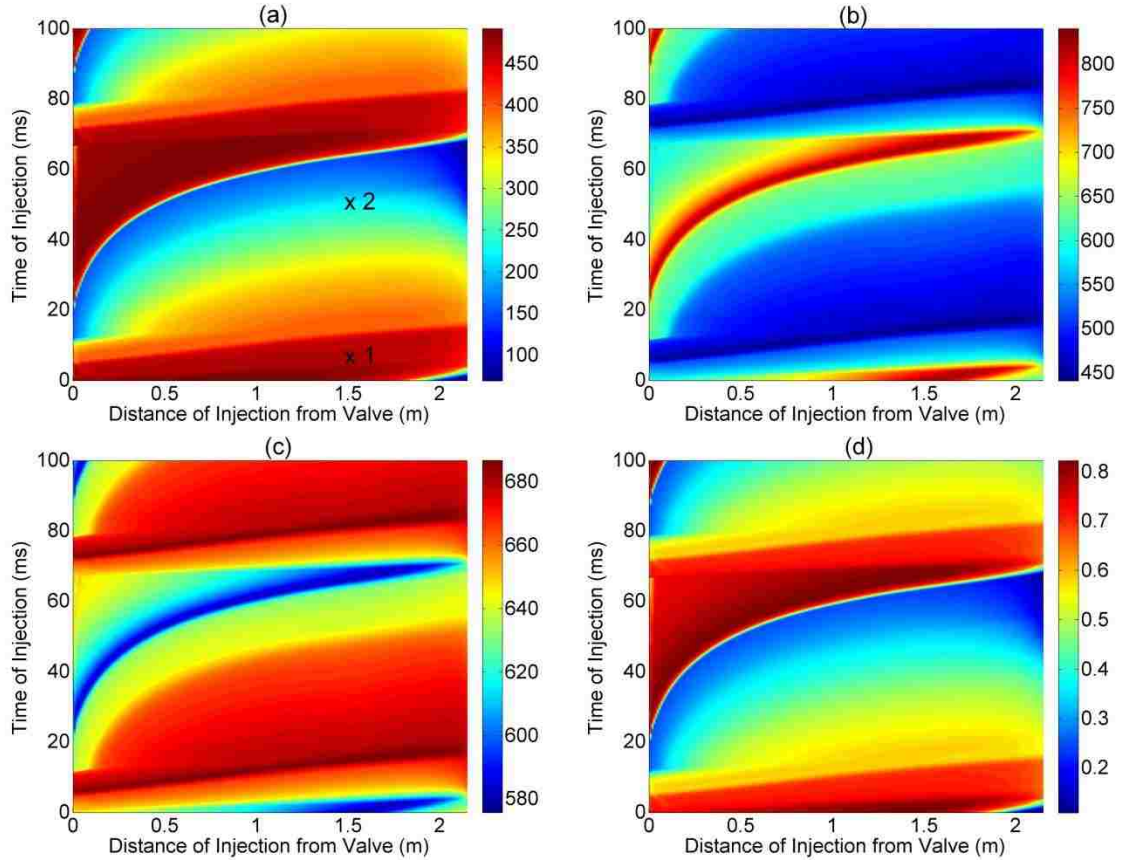


Figure 45: Contours of particle characteristics upon impacting on the substrate for 20-micron stainless steel 316 particles initiated at various locations and times in the domain: (a) speed (m/s), (b) temperature (K), (c) critical velocity (m/s) and (d) critical velocity ratio V/V_{cr} .

Based on published work [29] and using Equation 15 it is possible to estimate the values of critical velocity at impact for each individual particle in the domain. The names and corresponding values of variables and constants used in Equation 15 are listed in Table 7. The only variable whose value is not readily available and should be extracted from simulation results is T_i . The value of this parameter is available from the simulation results. Therefore using the data shown in Figure 45(b) and the prescribed equation it is possible to construct a similar contour to plot critical velocity values. This is shown in Figure 45(c).

$$V_{cr} = \sqrt{\frac{F_1 \cdot 4 \cdot \sigma_{TS} \left(1 - \frac{T_i - T_R}{T_m - T_R}\right)}{\rho} + F_2 \cdot c_p} \quad (15)$$

Table 7: Parameters used to calculate critical velocity.

Parameter	Name (Unit)	Value		
		Aluminum	Copper	SS 316
F_1, F_2	Empirical factors	1.2, 0.3 [29]		
σ_{TS}	Tensile strength (MPa)	110	250	500
T_i	Impact temperature	Simulation result		
T_R	Reference temperature	293 K		
T_M	Melting temperature (K)	933	1357	1783
ρ	Density (kg/m ³)	2719	8978	8030
c_p	Specific heat, (J/kg.K)	871	381	502

The most important aspect of the particle velocity is how close it is to the critical velocity. This relation can be revealed by considering the non-dimensional parameter V/V_{cr} , and comparing it to unity. It is additionally shown [64] that this parameter can be considered as a very important indicator of coating quality and can be utilized in parameter selection for cold spraying. A contour is constructed based on the two contours of V and V_{cr} and shown in Figure 45(d). Using this contour one can determine an optimum location along the spray device and a periodic injection scheme that ensures the high-energy zone of the flow is best utilized.

These plots can be used as a guideline for determining the range of time and location at which particle injection can yield the best results. As presented here a qualitative judgment of color is required to determine the value of interest at a particular time and location of particle injection. It is possible to extract results at a specific injection location if a more quantitative comparison with experimental results is desired. At the typical location of injection (where powder is typically injected in the physical device, as shown in Figure 29), non-dimensional velocity ratios, V/V_{cr} , corresponding to different injection times are extracted from the results presented in Figure 45 and plotted in Figure 46. Similar analyses are conducted for all other powder materials and particle sizes of interest and also included in the same plot. Based on this plot it is seen that a coating of aluminum and copper can be formed if injected at certain times, however a coating of stainless steel 316 will not form regardless of injection time.

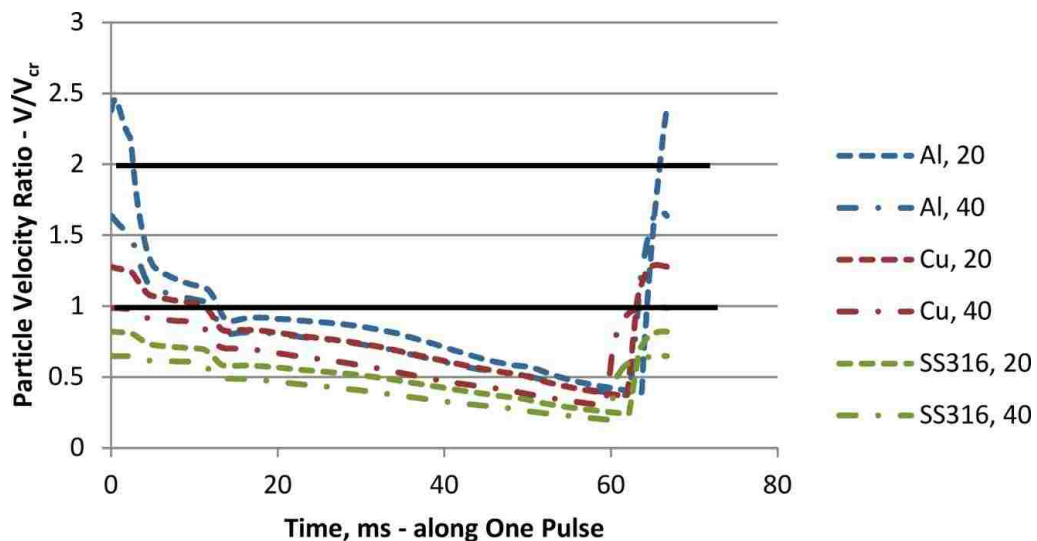


Figure 46: Calculated values of V/V_{cr} for particles of various sizes and materials injected at typical location and various times.

The results demonstrated in Figure 46 are very helpful in understanding the behavior of various powder materials in the device, and in establishing the criteria for a powder feeder device. For example, regardless of the material of the powder, a powder feeder should begin placing powder particles in the device approximately 8 ms prior to the opening of the valve, and continue to do so until approximately 15 ms after the opening of the valve. The remainder of the time is not very favorable for achieving good deposition performance.

5.3.2 Experimental Work and Comparison with Discrete Phase Predictions

The results from Figure 46 are further analyzed in order to allow for better comparison with experimental observations. It is known that when the non-dimensional parameter V/V_{cr} has a value between 1.0 and 2.0, impacts will result in deposition, with higher values corresponding to improved coating properties (e.g. coating density and bond strength) [29, 64]. At values below 1.0 bonding will not occur, and above 2.0 erosive behavior, rather than bonding, starts. In order to assess whether a coating will form or not under a given set of conditions, and predict its expected quality, the maximum value of this parameter should be considered.

Presently, particle injection in the real spray device is achieved through a conventional powder feeder designed to provide a steady stream of gas-powder mixture. The gas and powder mixture from this powder feeder is allowed to interact naturally with the main carrier gas flow, therefore it is not known how and at what time instances powder particles are introduced into the flow. However, one can use the time per cycle during which V/V_{cr} falls above 1.0 and below 2.0 as a measure for predicting deposition

efficiency (DE) - the higher this value the more likely particles will attain the required speed for bonding and therefore the higher the predicted DE. This trend is clearly visible in data presented in Table 8.

Table 8: Maximum value of V/V_{cr} and time per cycle during which this value falls between 1.0 and 2.0, in comparison with experimental values of deposition efficiency, for various particle materials and sizes.

Particle Properties		Maximum Value of V/V_{cr}	Time per Cycle: $1.0 \leq V/V_{cr} \leq 2.0$		Experimental Value of Deposition Efficiency (%)
Material	Size - micron		Absolute (ms)	Percentage (%)	
Aluminum	20	2.5	11.5	16.5	11±2
Aluminum	40	1.6	15.0	22.5	
Copper	20	1.3	15	22.5	12±1
Copper	40	1.0	14.5	21.7	
Stainless Steel 316	20	0.8	0.0	0.0	0.5
Stainless Steel 316	40	0.6	0.0	0.0	

Deposition efficiency is an important measure of the performance of a spray process. It is defined as the mass ratio of powder deposited on a substrate to the powder delivered towards the substrate. This is a well-established concept in the field of cold spray and procedural details of the measurements are available in the existing literature [65]. The values of deposition efficiency which are calculated based on these measurements are also included in Table 8 for comparison. These calculations assume that powder feeding occurs uniformly throughout a pulse.

The aluminum powder used in the experiment is the H-15 type of pure aluminum (99.7% weight aluminum) produced by Valimet Inc. (Stockton, California, USA) and the copper powder is the TEKMAT™ CU-38-X1 type of pure copper (99.5% purity, less than 0.1% oxygen) available from Tekna Advanced Materials Inc. (Sherbrooke, Quebec, Canada), both sieved to the 25-38 micron size range. It is evident from the results summarized in Table 8 that the model used in this study correctly predicts the general outcome of the spray process. For stainless steel, the powder is acquired from Atlantic Equipment Engineers: AEE (Bergenfield, New Jersey, USA). The model predicts that no particle will reach the critical velocity under these conditions. The spray trial reflects the same, as a DE of only 0.5% is negligible.

If powder injection occurs uniformly throughout the duration of a pulse, the model predicts that, on average, $19.5 \pm 3\%$ of aluminum particles and $22.1 \pm 0.4\%$ of copper particles will attain appropriate velocity to form a coating. An actual DE of 11% and 12% for aluminum and copper respectively correlate reasonably to these predictions. The discrepancy between the predicted values and the actual values can be attributed to two factors. Firstly, particles are added to the carrier gas via a gas-particle mixture. The particle feed gas mixes with the main carrier gas which will have a detrimental effect on the main flow, as well as the zone of interest that forms in the flow.

Additionally, the percentage values predicted by the model are based on the assumption that powder injection occurs uniformly throughout the duration of a gas

pulse. This is very unlikely to be the case. In reality, the interaction between the main gas flow and the particle feed flow may result in a more favorable or less favorable particle injection regime. The results obtained here suggest that the injection regime under these conditions is less favorable and detrimental to the process. In fact, this scenario can be seen to be likely by considering the results in Figure 46. From this plot it is evident that a slight decrease in the value will hurt copper results more severely than the aluminum results. This is reflected in a larger gap between simulation and prediction in the case of copper than aluminum.

5.3.3 Summary of Stage Three: Discrete Phase Model in Representative Geometry

A technique is implemented where particles can be injected at various location and time instances in order to help determine an appropriate particle injection location and timing. It is shown that timing of particle injection is an important factor in the efficiency of the coating process.

Results from the particle tracking study are analyzed and compared with actual spray results. It is found that the model correctly predicts the trends in spray results in terms of DE. A discrepancy between the predicted and actual DE values suggests that the method of injecting particles is perhaps not optimized. This highlights the importance of more closely studying the interaction between the particle feed flow and the main carrier gas flow. Ultimately a powder feeding mechanism that allows positively synchronizing powder injection with the main gas pulses can result in better utilizing the potential of the process.

In conducting the DE experiments coated coupons are created. These coupons, however, are not suitable for the purpose of obtaining cross-sections and generating micrographs. The operating conditions used in this study are only for validating the model. They correspond to the onset of the deposition process and hence the resulting coating properties and structures obtained through these experiments are not of interest. Micrographs of coating cross-sections generated using this technology under practical conditions can be found in literature for WC-based coatings [45], metallic coatings of aerospace carbon/epoxy composites [46], SiC particulate reinforced Al-12Si alloy composite coatings [47], as well as various traditional cold spray materials (Cu, Zn, Al) and new ones (amorphous Fe-based) [39].

In this study particle-particle [39] interaction and the effect of particles on the flow are not considered [39]. This is not required as the device is normally expected to operate under the 'dilute' condition where these effect are indeed negligible.

Chapter 6. Case Studies

The numerical tool that has been developed is used to study certain cases that are useful in the development of the technology. The fact that the model allows for qualitative and, more importantly quantitative predictions of the fate of sprayed powder particles makes it suitable for conducting targeted case studies. The effects of a few important geometrical and operational parameters of the device are considered.

6.1 Coating with Stainless Steel Powder

It was observed from both the experimental and numerical results of Stage Three of the study that a coating of stainless steel was not achieved. This was using nitrogen at 2 MPa (300 psi) as propellant and at a gas temperature of 550 °C with no preheating of the powder particles. An immediate question that arises is could a coating of stainless steel be made possible by increasing the gas temperature or by preheating the feedstock.

In Section 5.3.1 it was shown that gas temperature has a more pronounced impact on the process than supply pressure; it affects the process by increasing both gas speed and temperature. Therefore this parameter will be varied here. With recent technical progress made in the design and manufacturing of the device it has become possible to reach a heater temperature of 900 °C. The simulation is performed again with this heater temperature. Values of V/V_{cr} are plotted for the two cases of 550 °C and 900 °C heater temperature.

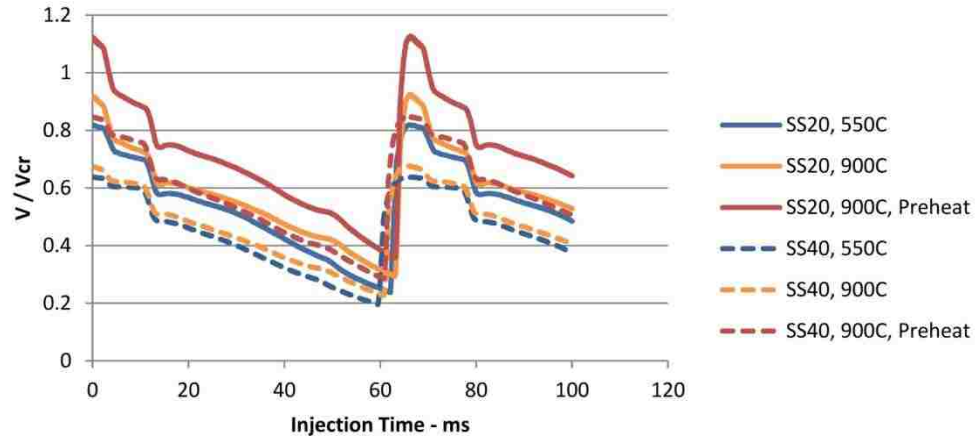


Figure 47: Effect of increased heater temperature setting and powder preheating on the fate of powder particles upon reaching the substrate.

This plot shows that increasing heater temperature will result in a slight increase in the value of V/V_{cr} however not sufficiently high for either 20 micron or 40 micron particles to reach deposition conditions. Another possible remedy under these conditions is to preheat the feedstock prior to introducing it to the spray device. The effect of this preheating action, to 900 °C, is also shown in Figure 47. It is observed that stainless steel particles of 20 micron can now reach the critical velocity, although for a brief period of time. These findings are in agreement with general findings of experiments, from unpublished internal reports, where coatings of stainless steel can be formed using nitrogen at extreme conditions [66].

6.2 Effect of Heater Length

An important aspect of the design of the SISIP process is the length of the heater. In fact one may wonder why such a long tube length, that is 1.4 m, is required. It may appear that this length will only contribute to the strong shock-wave losing its strength and hence hindering the performance of the device.

The current length of this tube has been determined through numerous preliminary lab experimentations. It has been found that a good compromise of coating quality and deposition rate can be achieved when the heater length is in the range of (1.2-1.6) meters [66]. Here, a few length are considered to study this effect in greater detail. The lengths studied are (0.2, 0.6, 0.9, 1.4 and 2.1) meters and the simulation is repeated with the same conditions as previously described. Powder particles of Al, Cu and SS are injected in the tube at the typical injection location and their fate is determined upon impact on the substrate. The value of V/V_{cr} is chosen to determine this fate. Plots showing this value as a function of injection time during a pulse are shown for Al, Cu and SS in Figure 48 top, middle and bottom respectively.

The maximum and minimum values of V/V_{cr} , and the percentage of pulse during which this value falls above unity are the values of interest in these graphs. For ease of analysis these results are summarized in detail in Table 9. The maximum value of V/V_{cr} can be used as an indication of best coating quality achievable under the conditions, and the cycle time percentage above parity is an indication of deposition rate.

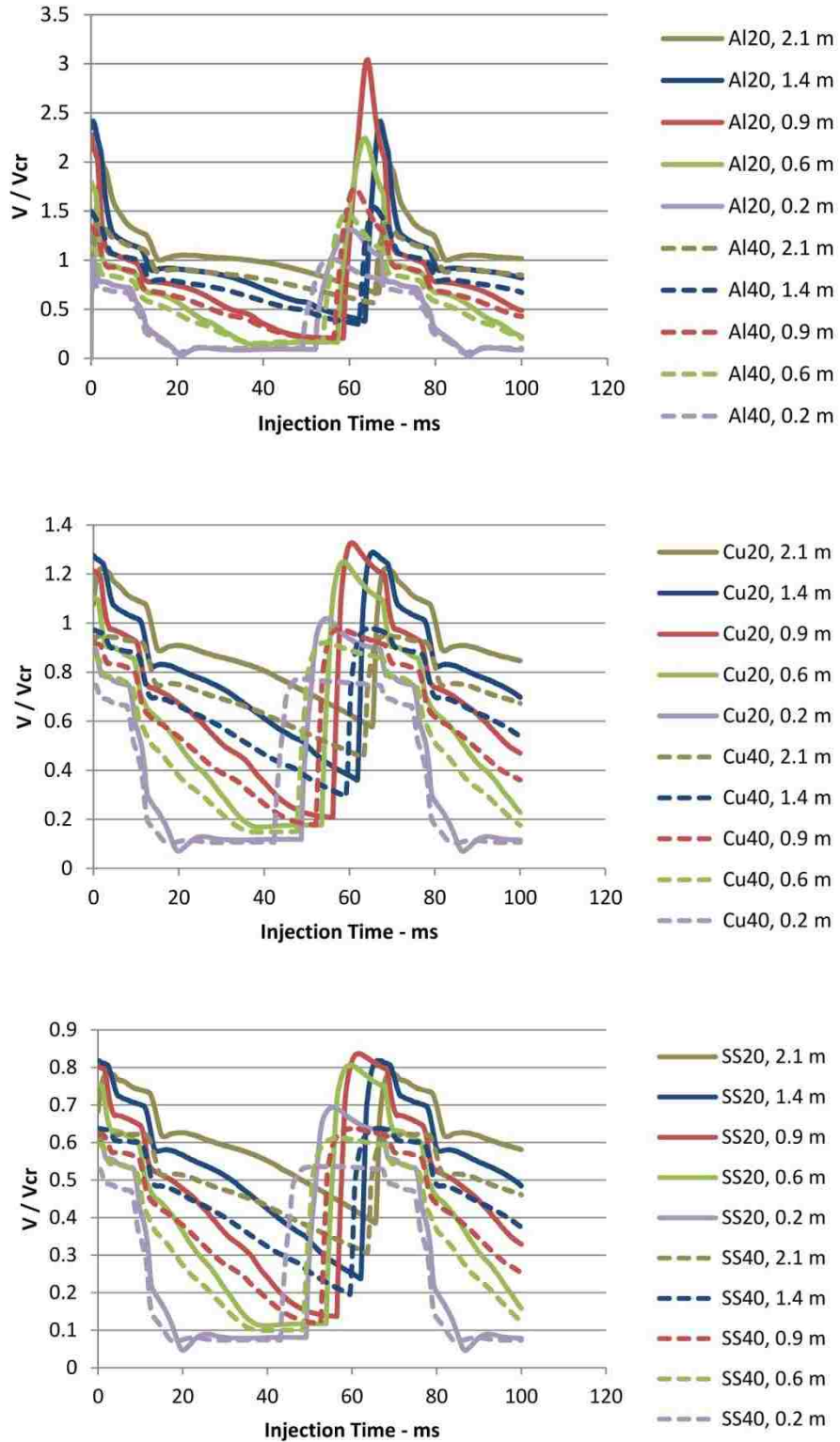


Figure 48: Values of V/V_{cr} as a function of injection time for aluminum (top), copper (middle) and stainless steel (bottom) powder particles.

Table 9: Minimum and maximum values of V/V_{cr} , and the percentage of a cycle during which this value falls above unity, as a function of heater length, for particles of aluminum, copper and stainless steel.

Heater Length (m):	V/V_{cr} Analysis														
	Max V/V_{cr}					Cycle Percentage > 1					Min V/V_{cr}				
	0.2	0.6	0.9	1.4	2.1	0.2	0.6	0.9	1.4	2.1	0.2	0.6	0.9	1.4	2.1
Aluminum 20	1.3	2.2	3	2.4	2	18	16	24	23	54	0	0.1	0.2	0.4	0.7
Aluminum 40	1	1.5	1.7	1.5	1.4	4	19	17	22	21	0.1	0.2	0.2	0.3	0.6
Copper 20	1	1.3	1.3	1.3	1.2	4	19	19	22	21	0.1	0.2	0.2	0.4	0.6
Copper 40	0.8	0.9	1	1	1	0	0	0	0	0	0.1	0.1	0.2	0.3	0.5
Stainless Steel 20	0.7	0.8	0.8	0.8	0.8	0	0	0	0	0	0.1	0.1	0.1	0.2	0.4
Stainless Steel 40	0.5	0.6	0.6	0.6	0.6	0	0	0	0	0	0	0.1	0.1	0.2	0.3

For many variations of particle materials and sizes the maximum value of V/V_{cr} is not sensitive to heater length. This is more evident with heavier particle materials and sizes. However, where sensitive to length, the value of V/V_{cr} reaches a maximum value at a length of 0.9 m and stays relatively high up to a length of 1.4 m. This indicates that it is favorable to have a heated length of tube prior to injection within the range of (0.9-1.4) m.

Besides the exceptional case of Aluminum 20, the percentage of injection cycle during which V/V_{cr} holds a value above parity is also maximum at a length of (0.9-1.4) m. The case of Al20 with a 2.1 m heater length can be discounted as a lucky incident when the shape of the graph is considered.

The minimum value of V/V_{cr} uniformly increases with increasing heater length. This may suggest an advantage for a very long heated portion however this indicator is insignificant since a V/V_{cr} value below one will not result in the creation of a coating anyway.

Overall it seems that where results are sensitive to the heater length, a length of (0.9-1.4) m is rather optimal in most regards. This is in agreement with an experimentally obtained optimal length specification, which is recommended to be in this range. It also appears that increasing the length beyond this range results in the minimum and maximum V/V_{cr} values approaching each other and creating a rather flat shape. This will

ultimately resemble a steady-state process which will contradict the promise of the technology.

6.3 Effect of Process Frequency

Effect of process frequency is studied by conducting the same simulation as the Stage Three of the study at 15 Hz, compared to 30 Hz at that stage. The range of frequencies achievable by the device is (10-50) Hz, however frequencies in the range of (15-30) Hz are more typical of the actual operation of the device. These effects for aluminum, copper and stainless steel particles are shown in Figure 49 top, middle and bottom respectively. These plots show values of V/V_{cr} as a function of injection time during a pulse. Immediately one can see there are twice as many pulses in the 30 Hz case as there are in the 15 Hz.

The results show that the range of critical velocity narrows from approximately 0.2-1.3 at 15 Hz down to approximately 0.3-1.2 at 30 Hz. This suggests that if one is able to time the particles perfectly then running the device at 15 Hz can yield better results, however if injection timing is not possible then it is likely that operating at 30 Hz will yield a more 'uniform' coating.

Also, these results suggest that in the extreme case of very high frequency the range may become very narrow. This is expected from the flow physics too where at very high frequencies residual pressure after a pulse will weaken the subsequent shock-wave, approaching a steady-state flow.

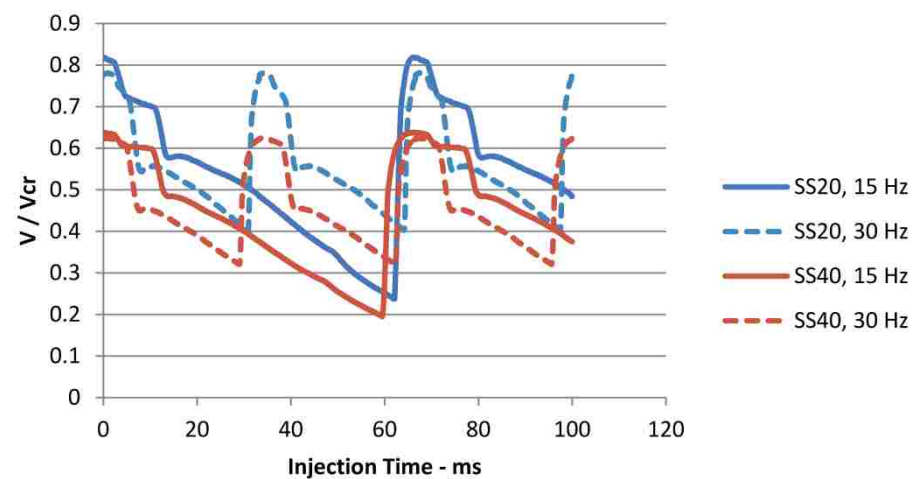
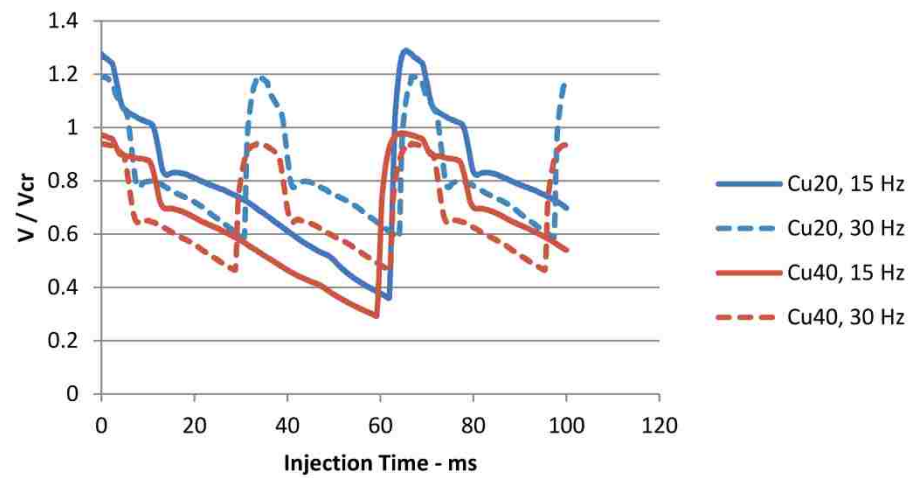
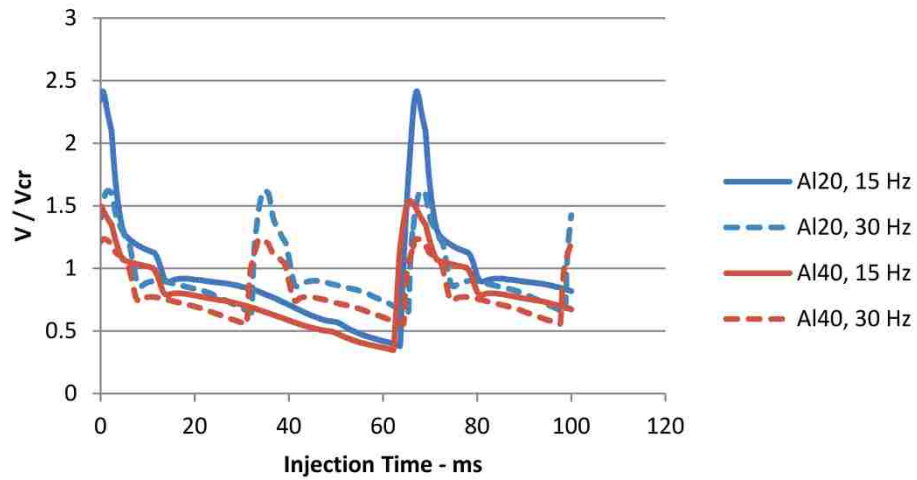


Figure 49: Effect of frequency on values of V/V_{cr} for aluminum (top), copper (middle) and stainless steel (bottom) powder feedstock.

6.4 Effect of Powder Heating Temperature

Effect of powder heating temperature has been studied by varying the powder preheat temperature from room temperature to 300 °C and then 700 °C. The effect of this change on particle temperatures upon impacting the substrate is shown in Figure 50. These effects are shown for aluminum, copper and stainless steel particles.

It is evident that smaller particles show little change with preheat temperature. This can be explained by the low energy content stored in them and by the large surface to volume ratio that will lead to increased heat transfer from the particles. Subsequently the initial energy in the form of temperature gets dissipated quickly.

Moreover, aluminum sees the largest temperature variation. This can be associated with shorter flight times due to less weight and therefore less chance of dissipating the initial heat. Between steel and copper, it seems steel sees a greater effect from preheating. This is because copper has a larger heat transfer coefficient.

The effect of powder preheat temperature on the ultimate fate of particles is considered next. This is shown in top, middle and bottom portions of Figure 51 for aluminum, copper and steel particles respectively.

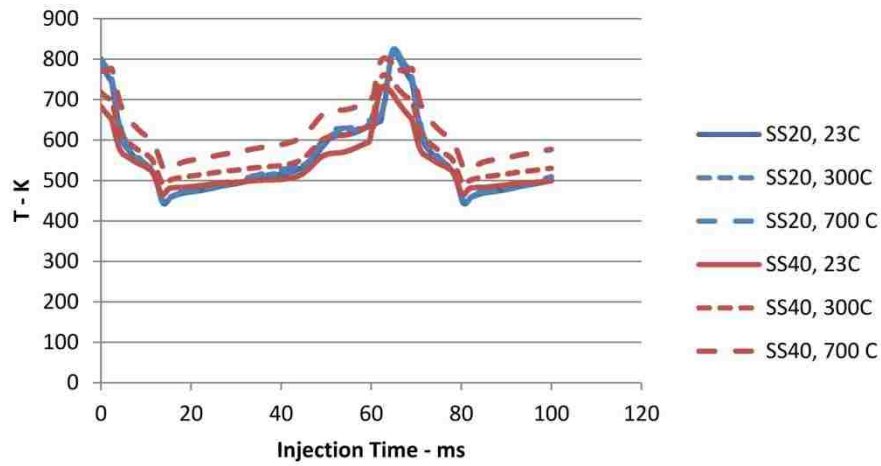
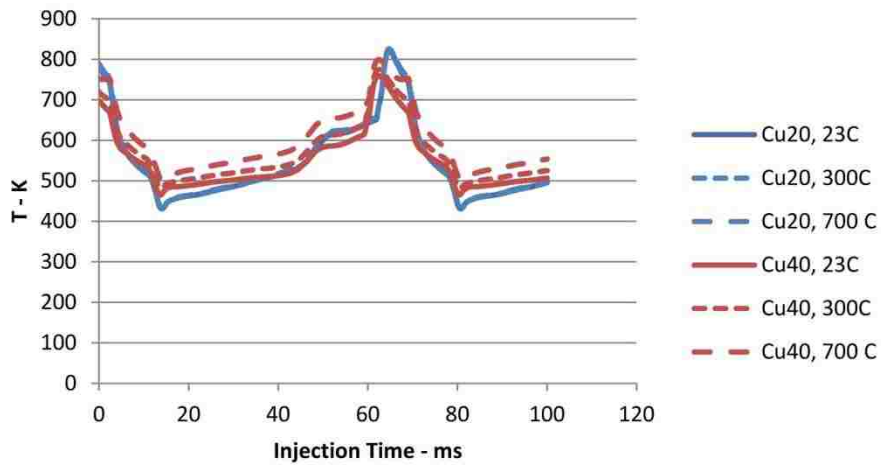
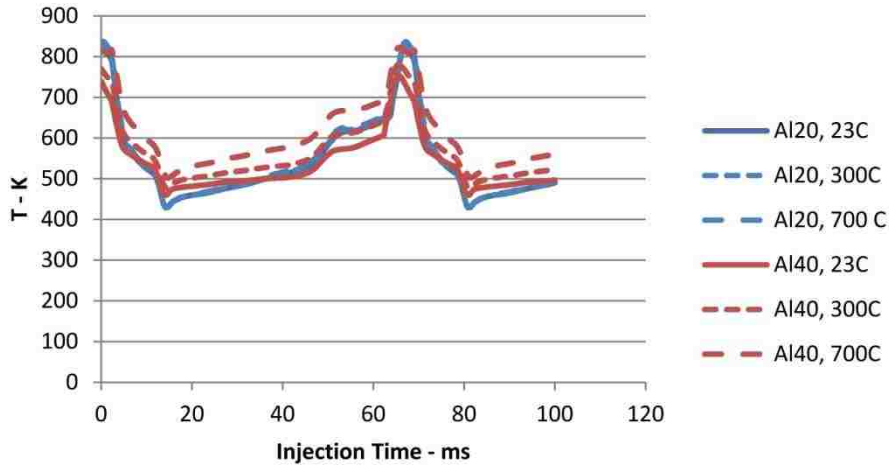


Figure 50: Effect of powder preheat temperature setting on the value of V/V_{cr} for particles of (top) aluminum, (middle) copper, and (bottom) stainless steel

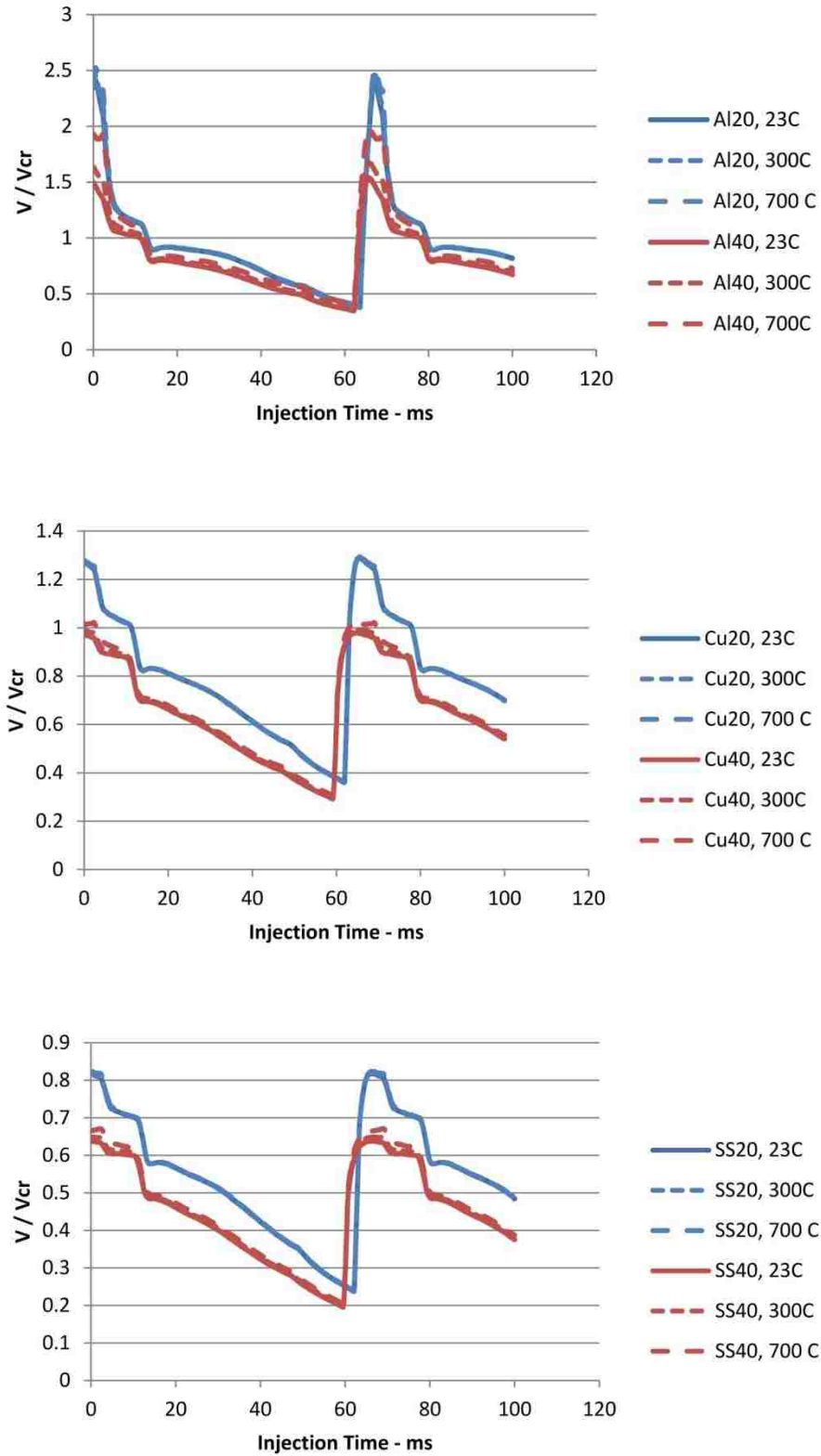


Figure 51: Effect of powder preheat temperature setting on the value of V/V_{cr} for particles of (top) aluminum, (middle) copper, and (bottom) stainless steel

Under the conditions of this simulation, the end result of varying powder preheat temperature on the critical velocity ratio is not very significant (except perhaps for 40-micron aluminum particles). This appears to contradict some historical experimental observations [66]. It seems the gain due to increasing the temperature to 700 °C from 300 °C is considerably greater than the gain due to increasing from 25 °C to 300 °C. This agrees very well with historical experimental observations [66]. This may also suggest that a further jump to perhaps 900 °C could lead to more significant gains. This is in agreement with the greater enhancement observed from increasing preheat temperature to 900 °C in Section 6.1. Solid experimental evidence does not exist to make any firm conclusions, however it can be expected that the results should be understated because they ignore entrainment of powder feed gas at elevated temperatures.

6.5 Effect of Powder Loading

In general, in kinetic spraying processes it has been observed that powder loading has an effect on the performance of the system. Powder loading is defined as the average mass of the discrete phase materials to the average mass of the gaseous phase. In SISP this can be defined as the ratio of mass of powder per pulse, to the mass of gas per pulse.

In other kinetic spraying processes, it has been observed that above a loading of approximately 1% [56], the effect of discrete phase on the gaseous phase becomes significant, and the gaseous phase is visibly affected by the presence of the discrete phase. At loading ratios of around 5% the effect becomes so significant that the

performance of the system in creating a coating is significantly hindered. A similar trend is expected in the SISP.

In order to examine this, two cases, one with 0.4% and one with 4.3% loading were considered in addition to the baseline case of 0.0% (no particle effect on the flow field). In conducting these simulations, the effect of powder particle phase on the gas phase has been enabled in the model. The resulting particle characteristics, in terms of V/V_{cr} , are plotted in Figure 52. It is observed that here is a slight decrease in velocity, only for the slowest particles, from the baseline for both cases and nearly no change in temperature. The two cases of 0.4% and 4.3% loading are nearly identical in both velocity and temperature. Higher particle loading levels are not attempted due to the limitations of the memory allocation capability of Fluent not allowing greater number of particles simultaneously in a simulation.

It is concluded that the simulation technique developed here does not distinguish between the cases of various powder loading. In fact, this technique and software has previously been shown to be ineffective in predicting the influence of the discrete phase on the flow field [56]. Instead a specialty CFD solver, called CFDLIB, developed by the Los Alamos National Laboratory, was used. The code uses an Eulerian approach in order to account for the discrete phase. Building a new model using a different solver and a new approach is considered to be beyond the scope of this work.

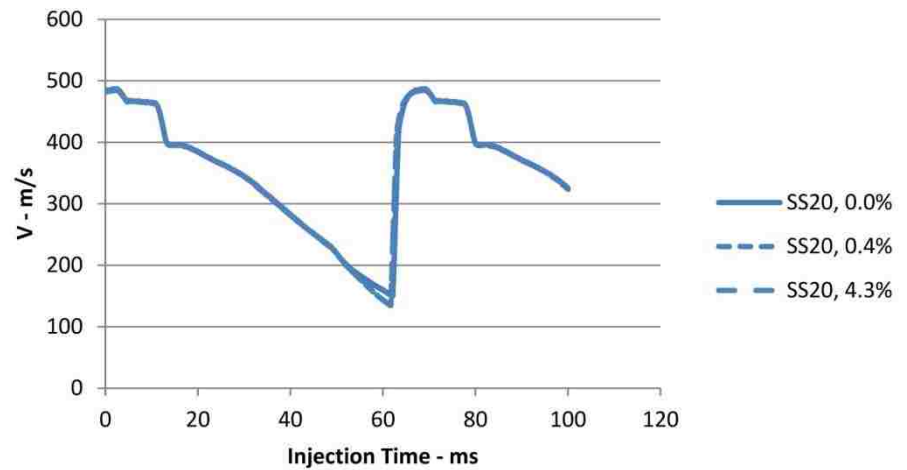
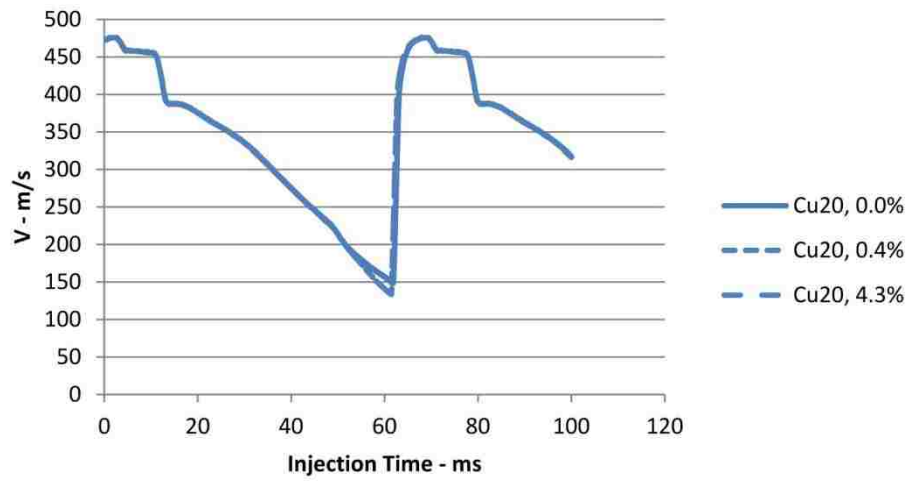
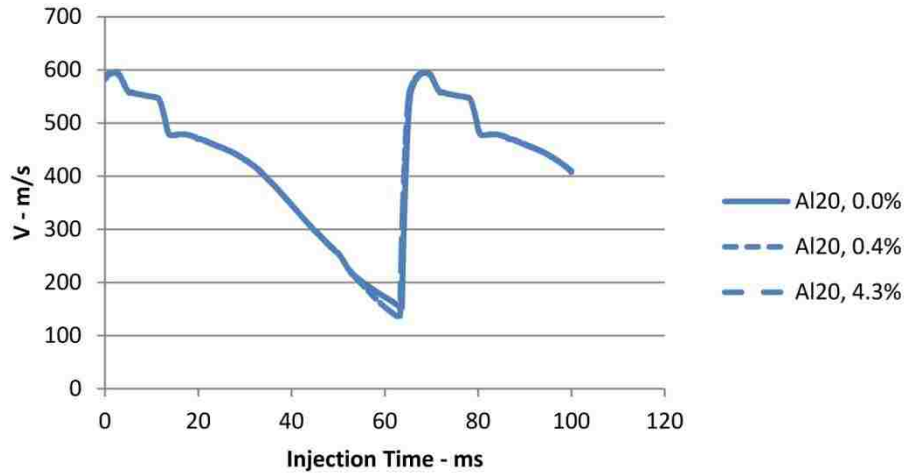


Figure 52: Effect of powder loading on the value of V/V_{cr} for particles of (top) aluminum, (middle) copper, and (bottom) stainless steel.

Chapter 7. Conclusion

A CFD model is successfully developed and used to simulate the Shock-wave Induced Spraying Process. Considering the unsteady nature of the flow, the usual space domain that is commonly used for plotting flow variables is replaced by a space-time domain with the color indicating flow variable values. Using a geometry that generally resembles that proposed for the process, the underlying physical principles of the process are explored.

It is found that due to the unsteady nature of the process, it is possible to form a region in the flow where both velocity and temperature are simultaneously elevated. This is a very important feature of the flow that is unique to this process and sets it apart from its steady counterparts (traditional cold spray methods). In steady-state cold spray processes, the main focus is on increasing the velocity of the flow as well as that of the powder particles. This is often achieved at the expense of losing thermal energy. It is possible to utilize this high velocity and temperature region by correctly injecting powder particles in a way that they will be in this zone for a sufficient portion of their flight period in order to land on the substrate at energy levels that are higher than steady-state cold spray methods.

Also important is the discovery that this zone of elevated energy level elongates as the flow evolves in time and distance along the tube. This means that by selecting a longer tube it is possible to increase the opportunity for the particles to stay within this

zone for the entire duration of their flight. It should be noted that there is a limit to this, if the tube is extended too long the strength of the shock-wave will start to dissipate. Therefore, its speed and total energy content will be diminished.

It is found that increasing process pressure causes a region of elevated gas speed to last longer in time. Increasing the process temperature, however, will result in increasing the energy content of the flow by increasing its temperature as well as velocity. The increase in velocity is a result of a higher speed of sound due to the increased temperature, although Mach number profiles remain largely unaffected.

The effect of gas type on the flow field is mainly driven by the speed of sound in the medium. When helium is used, all flow features propagate in the flow significantly faster than when air is used. The pressure builds up in the tube much faster and the shock-wave reaches a higher speed. For the same reason, the region of elevated energy also tends to dissipate faster. This shows that although use of helium can result in a higher velocity for the powder particles, realizing this potential demands a more careful tuning of the process.

This model agrees well with an existing one-dimensional model in predicting major characteristics of the flow, however, it offers several advantages. Firstly, the one-dimensional model divides the flow in a few zones and approximates all flow variables with one value in each zone. This ignores a lot of details of the flow that are captured using this CFD model. Additionally, it only considers the propagation of features

initiating from the valve. Although these are the most dominant effects, there are a lot of features that initiate elsewhere in the flow.

Additionally, the existing one-dimensional model can only predict the opening of the valve, not its closing. It is also limited in accounting for a tapered portion at the tip of the tube as well as the effects of the tube exit and a substrate. All these effects are captured using the CFD model.

The gas phase results are validated by examining temporal variations of gas pressure at two locations that are important to the spray process, namely immediately after the gas valve and at the location of particle injection. A good match is achieved. Important features of the flow are examined; a zone develops in the flow that enjoys a high content of both velocity and temperature.

The model is then enhanced to accurately account for valve opening and closing, gas heating, as well as particle tracking. Additionally, it is capable of capturing the two-dimensional effects in the surroundings outside of the nozzle. Finally, it offers great flexibility for conducting subsequent particle tracking calculations throughout the domain.

A technique is implemented where particles are injected at various locations and time instances in order to determine an appropriate particle injection location and timing.

It is shown that timing of particle injection is an important factor in the effectiveness of the coating process.

Results from the particle tracking study are analyzed and compared with actual spray results. It is found that the model correctly predicts the trends in spray results in terms of Deposition Efficiency. A discrepancy between the predicted and actual Deposition Efficiency values suggests that the method of injecting particles is perhaps not optimized. This highlights the importance of more closely studying the interaction between the particle feed flow and the main carrier gas flow. Ultimately a powder feeding mechanism that allows positively synchronizing powder injection with the main gas pulses can result in better utilizing the potential of the process.

The model is then used for conducting parametric studies. First, conditions for achieving a coating of stainless steel using nitrogen as driving gas is examined. It is found that coatings of stainless steel cannot be obtained under the typical conditions of the flow, but increasing heater temperature and powder preheating temperature simultaneously can result in onset of a coating.

Further, it was found that an increase in powder preheat temperature of up to 700°C results in a modest increase in powder temperature upon impact, and little difference in particle speed. This suggests negligible impact on process performance. It is expected that further increase of this temperature can yield more significant gains in process performance.

An analysis of effect of heater length showed that a length in the range of 0.9 m - 1.4 m is likely to yield the best results for the case of aluminum, copper and stainless steel particles of typical 20-micron size. It was further found that increasing spray frequency results in a dilution of extreme particle characteristics upon impacting the substrate. Both peaks and valleys in the V/V_{cr} values of particle upon impact are moderated. A moderation of the valleys is perhaps favorable, potentially leading to a larger number of particles adhering to the substrate. A moderation of the peaks, however, is detrimental to the performance of the device. It is speculated that the extreme case of high frequency shall yield near-constant particle characteristics upon impact, defeating the purpose of an interrupted process.

An attempt was made to account for particle–particle interaction and the effect of particles on the flow. This may not be required as the device is normally expected to operate under the ‘dilute’ condition where these effects are indeed negligible.

Chapter 8. Recommendation for Future Work

The most significant outcome of the present research is the characterization of particle behavior, and time dependence of this behavior. It has been demonstrated that there is a certain time period over each pulse during which powder injection yields favorable particle energy upon impact. This result can serve as a guideline for designing a discrete powder feeder. It is recommended that implementing such powder feeding mechanism be pursued.

The interaction of the main gas flow with the gas and particle flow from powder feeding line is unknown. A knowledge of this interaction is very desirable as it helps better explain the results of this research by indicating the actual injection scheme that occurs in the spray process. It is recommended that flow visualization be used to find this interaction and observe the actual powder injection scheme. An understanding of this powder injection scheme also allows for attempting to improve this interaction by adjusting parameters related to powder feeding to optimize powder injection timing. These parameters include gas flow rate through the powder feeding line, the diameter and size of the powder feeding line, as well as the gas volume of the powder feeding canister. A flow visualization study also allows better understanding of the interaction between particles and the shock-wave, as well as the interaction between the shock-wave and the substrate.

The same kind of understanding can be alternatively achieved by expanding the CFD model of this study to a three-dimensional model. This enhancement will allow the inclusion of powder feeding gas flow and therefore the interaction between this flow and the main SISP flow can be studied. This enhancement allows for incorporating an accurate model of the rotary valve instead of approximating it with a ball-seat valve. Furthermore, it will allow an assessment of the axisymmetric assumption used in the present study.

The results of the present study, pertaining to V/V_{cr} ratio of powder particles, can be used to predict the quality of the coating. Correlations between this ratio and coating quality measures such as coating density and bond strength exist in the literature [64]. These correlations can be used to further post-process the results of this study to enable predictions of coating quality.

Finally, the current at modeling the effect of powder loading was unsuccessful. It is recommended that an alternative modeling tool, namely CFDLIB (Los Alamos National Laboratory, Los Alamos, New Mexico, USA), be used to study this effect [56].

References

1. P. Fauchais, A. Vardelle and B. Dussoubs, Quo Vadis Thermal Spraying?, *Journal of Thermal Spray Technology* (2001), **10**, 44-66.
2. P. Fauchais, Understanding Plasma Spraying, *Journal of Physics D (Applied Physics)* (2004), **37**, 86-108.
3. Y. Bartosiewicz, P. Proulx and Y. Mercadier, A Self-Consistent Two-Temperature Model for the Computation of Supersonic Argon Plasma Jets, *Journal of Physics D (Applied Physics)* (2002), **35**, 2139-2148.
4. P. Pei, S. G. Malghan, S. J. Dapkunas and P. H. Zajchowski, Characterization and Processing of Spray-Dried Zirconia Powders for Plasma Spray Application, *Journal of Thermal Spray Technology* (1996), **5**, 343-351.
5. L. L. Shaw, D. Goberman, R. Ren, M. Gell, S. Jiang, Y. Wang, T. D. Xiao and P. R. Strutt, The Dependency of Microstructure and Properties of Nanostructured Coatings on Plasma Spray Conditions, in "IUMRS-ICAM '99 Sumposium X, Surface Engineering, June 13, 1999 - June 18, 1999", Elsevier S.A., Beijing, China (2000).
6. K. Mabey, B. L. Smith, G. Whichard and T. McKechnie, Coanda-Assisted Spray Manipulation Collar for a Commercial Plasma Spray Gun, *Journal of Thermal Spray Technology* (2011), **20**, 782-790.
7. A.-F. Kanta, G. Montavon, C. C. Berndt, M.-P. Planche and C. Coddet, Intelligent System for Prediction and Control: Application in Plasma Spray Process, *Expert Systems with Applications* (2011), **38**, 260-271.
8. Gordon England, Independent Metallurgist and Consultant to the Thermal Spraying Industry, www.gordonengland.co.uk, (2012).
9. T. Watanabe, T. Sato and A. Nezu, Electrode Phenomena Investigation of Wire Arc Spraying for Preparation of Ti-Al Intermetallic Compounds, in "14th Symposium on Plasma Science for Materials (SPSM-14), 13-14 June 2001 - Thin Solid Films", Elsevier, Switzerland (2002).

10. T. Watanabe, X. Wang, E. Pfender and J. Heberlein, Correlations between Electrode Phenomena and Coating Properties in Wire Arc Spraying, *in* "10th Symposium on Plasma Science for Materials, 11-12 June 1997 - Thin Solid Films", Elsevier, Switzerland (1998).
11. N. Hussary and J. Heberlein, Effects of Metal Atomization, Arc and Pressure Fluctuations on the Final Particle Size Distribution in the Wire Arc Spraying Process, *in* "2003 IEEE International Conference on Plasma Science, June 2, 2003 - June 5, 2003", Institute of Electrical and Electronics Engineers Inc., Jeju, Korea, Republic of (2003).
12. N. A. Hussary and J. V. R. Heberlein, Atomization and Particle-Jet Interactions in the Wire-Arc Spraying Process, *Journal of Thermal Spray Technology* (2001), **10**, 604-610.
13. S. S. Madaeni, M. E. Aalami-Aleagha and P. Daraei, Preparation and Characterization of Metallic Membrane Using Wire Arc Spraying, *Journal of Membrane Science* (2008), **320**, 541-548.
14. A. Heuberger, P. Izquierdo, T. Haug, T. Wittrowski and F. Lampmann, Twin Wire Arc Spraying as a New Coating Technology for Liner-Free Cylinder Bores, *Welding and Cutting* (2004), **3**, 356-361.
15. M. R. Saghi Beyragh, S. Khameneh Asl, R. Vasfpour, F. Tazesh and P. Khallagi, A Comparison between the Corrosion Resistances of High Velocity Oxy Fuel (Hvof) Sprayed Coatings and Hard Chromium Coatings, *in* "3rd International Symposium on Explosion, Shock Wave and High-Energy Reaction Phenomena, ESHP 2010, September 1, 2010 - September 3, 2010", Trans Tech Publications Ltd, Seoul, Korea, Republic of (2011).
16. L. Jacobs, M. M. Hyland and M. De Bonte, Comparative Study of Wc-Cermet Coatings Sprayed Via the Hvof and the Hvaf Process, *Journal of Thermal Spray Technology* (1998), **7**, 213-218.
17. P. Richer, M. Yandouzi, L. Beauvais and B. Jodoin, Oxidation Behaviour of Conical Bond Coats Produced by Plasma, Hvof and Cold Gas Dynamic Spraying, *Surface and Coatings Technology* (2010), **204**, 3962-3974.

18. A. Houdkova, O. Blahova, F. Zahalka and M. Kaparova, The Instrumented Indentation Study of Hvf-Sprayed Hardmetal Coatings, *Journal of Thermal Spray Technology* (2012), **21**, 77-85.
19. C. Lyphout, P. Nylen and L. G. Ostergren, Adhesion Strength of Hvf Sprayed In718 Coatings, *Journal of Thermal Spray Technology* (2012), **21**, 86-95.
20. A. Maatta, U. Kanerva and P. Vuoristo, Structure and Tribological Characteristics of Hvf Coatings Sprayed from Powder Blends of Cr₃C₂-25NiCr and NiCrBSi Alloy, Springer New York, 233 Springer Street, New York, NY 10013-1578, United States (2011).
21. J. A. Picas, M. Punset, M. T. Baile, E. Martin and A. Forn, Effect of Oxygen/Fuel Ratio on the in-Flight Particle Parameters and Properties of Hvf Wc-Cocr Coatings, *Surface and Coatings Technology* (2011), **205**, S364-S368.
22. P. Saravanan, V. Selvarajan, S. V. Joshi and G. Sundararajan, Experimental Design and Performance Analysis of Alumina Coatings Deposited by a Detonation Spray Process, *Journal of Physics D: Applied Physics* (2001), **34**, 131-140.
23. G. Sundararajan, K. U. M. Prasad, D. S. Rao and S. V. Joshi, A Comparative Study of Tribological Behavior of Plasma and D-Gun Sprayed Coatings under Different Wear Modes, in "Journal of Materials Engineering and Performance", ASM Int, USA (1998).
24. E. Irissou, J.-G. Legoux, A. Ryabinin, B. Jodoin and C. Moreau, Review on Cold Spray Process and Technology. Part I. Intellectual Property, *Journal of Thermal Spray Technology* (2008), **17**, 495-516.
25. J. Villafuerte, Current and Future Applications of Cold Spray Technology, *Metal Finishing* (2010), **108**, 37-39.
26. M. Karimi, A. Fartaj, G. Rankin, D. Vanderzwet, W. Birtch and J. Villafuerte, Numerical Simulation of the Cold Gas Dynamic Spray Process, *Journal of Thermal Spray Technology* (2006), **15**, 518-523.
27. J. Karthikeyan, Evolution of Cold Spray Technology, *Advanced Materials and Processes* (2006), **164**, 12-13.

28. W.-Y. Li, C.-J. Li and G.-J. Yang, Effect of Impact-Induced Melting on Interface Microstructure and Bonding of Cold-Sprayed Zinc Coating, *Applied Surface Science* (2010), **257**, 1516-1523.
29. T. Schmidt, F. Gartner, H. Assadi and H. Kreye, Development of a Generalized Parameter Window for Cold Spray Deposition, *Acta Materialia* (2006), **54**, 729-742.
30. B. Jodoin, Cold Spray Nozzle Mach Number Limitation, *Journal of Thermal Spray Technology* (2002), **11**, 496-507.
31. T. Stoltenhoff, H. Kreye and H. J. Richter, An Analysis of the Cold Spray Process and Its Coatings, *Journal of Thermal Spray Technology* (2002), **11**, 542-550.
32. G. Mirshekari and M. Brouillette, One-Dimensional Model for Microscale Shock Tube Flow, *Shock Waves* (2009), **19**, 25-38.
33. H. G. Stever and R. L. Bisplinghoff, Shock Tube in Aerodynamic and Structural Research, *National Academy of Sciences -- Proceedings* (1954), **40**, 557-565.
34. S. Udagawa, W. Garen, B. Meyerer and K. Maeno, Motion Analysis of a Diaphragmless Driver Section for a Narrow Channel Shock Tube, *Shock Waves* (2008), **18**, 345-351.
35. D. E. Zeitoun and Y. Burtschell, Navier-Stokes Computations in Micro Shock Tubes, *Shock Waves* (2006), **15**, 241-246.
36. M. Karimi, B. Jodoin and G. Rankin, Shock-Wave-Induced Spraying: Modeling and Physics of a New Spray Process, *Journal of Thermal Spray Technology* (2011), **20**, 866-881.
37. M. Karimi, G. W. Rankin and B. Jodoin, Shock-Wave Induced Spraying: Gas and Particle Flow and Coating Analysis, *Surface and Coatings Technology* (2012), **207**, 435-442.
38. B. Jodoin, Method and Apparatus for Material Deposition, University of Ottawa, Ottawa, Ontario, Canada, US (2008).
39. B. Jodoin, P. Richer, G. Berube, L. Ajdelsztajn, A. Erdi-Betchi and M. Yandouzi, Pulsed-Gas Dynamic Spraying: Process Analysis, Development and Selected Coating Examples, *Surface and Coatings Technology* (2007), **201**, 7544-7551.

40. J. Villafuerte, D. Vanderzwet, M. Yandouzi and B. Jodoin, Shockwave Induced Spraying, *Advanced Materials and Processes* (2009), **167**, 32-34.
41. D. Goldbaum, J. Ajaja, R. R. Chromik, W. Wong, S. Yue, E. Irissou and J.-G. Legoux, Mechanical Behavior of Ti Cold Spray Coatings Determined by a Multi-Scale Indentation Method, *Materials Science & Engineering: A (Structural Materials: Properties, Microstructure and Processing)* (2011), **530**, 253-265.
42. H. Nakano, M. Yamada, M. Fukumoto and E. Yamaguchi, Microstructure of Interfacial Region between Cold-Sprayed Copper Coating and AlN Substrate Coated with Sputtered Titanium and Copper, *Journal of Thermal Spray Technology* (2011), **20**, 407-411.
43. E. Irissou, J.-G. Legoux, B. Arsenault and C. Moreau, Investigation of Al-Al₂O₃ Cold Spray Coating Formation and Properties, *Journal of Thermal Spray Technology* (2007), **16**, 661-668.
44. M. Yandouzi, E. Sansoucy, L. Ajdelsztajn and B. Jodoin, Wc-Based Cermet Coatings Produced by Cold Gas Dynamic and Pulsed Gas Dynamic Spraying Processes, *Surface and Coatings Technology* (2007), **202**, 382-390.
45. M. Yandouzi, L. Ajdelsztajn and B. Jodoin, Wc-Based Composite Coatings Prepared by the Pulsed Gas Dynamic Spraying Process: Effect of the Feedstock Powders, *Surface & Coatings Technology* (2008), **202**, 3866-3877.
46. F. Robitaille, M. Yandouzi, S. Hind and B. Jodoin, Metallic Coating of Aerospace Carbon/Epoxy Composites by the Pulsed Gas Dynamic Spraying Process, *Surface and Coatings Technology* (2009), **203**, 2954-2960.
47. M. Yandouzi, P. Richer and B. Jodoin, Sic Particulate Reinforced Al-12si Alloy Composite Coatings Produced by the Pulsed Gas Dynamic Spray Process: Microstructure and Properties, *Surface and Coatings Technology* (2009), **203**, 3260-3270.
48. Centerline Windsor Limited, www.centrline.com, (2012).
49. Supersonic Spray Technologies - a Division of Centerline, www.supersonicspray.com, (2012).
50. E. Kadyrov, Gas-Particle Interaction in Detonation Spraying Systems, *Journal of Thermal Spray Technology* (1996), **5**, 185-195.

51. K. Ramadan and P. B. Butler, Analysis of Particle Dynamics and Heat Transfer in Detonation Thermal Spraying Systems, *Journal of Thermal Spray Technology* (2004), **13**, 248-264.
52. J. E. Cannon, M. Alkam and P. B. Butler, Efficiency of Pulsed Detonation Thermal Spraying, *Journal of Thermal Spray Technology* (2008), **17**, 456-464.
53. J. D. Anderson Jr, Modern Compressible Flow: With Historical Perspective McGraw Hill Book Co., Inc. New York (1990).
54. A. Papyrin, Cold Spray Technology, *Advanced Materials and Processes* (2001), **159**, 49-51.
55. Fluent 6.3 User's Guide, Ansys Fluent, 275 Technology Drive, Canonsburg, PA 15317 U.S.A. (2012).
56. B. Samareh and A. Dolatabadi, Dense Particulate Flow in a Cold Gas Dynamic Spray System, *Journal of Fluids Engineering* (2008), **130**, 081702 (081711 pp.).
57. R. Clift, J. R. Grace and M. E. Weber, Bubbles, Drops, and Particles Academic Press New York (1978).
58. M. A. Kuczmariski, R. A. Miller and D. Zhu, Cfd-Guided Development of Test Rigs for Studying Erosion and Large-Particle Damage of Thermal Barrier Coatings, *Modelling and Simulation in Engineering* (2011), 1-13.
59. M. Karimi, An Investigation of the Cold Gas Dynamic Spray Process Particle / Flow Field, Mechanical, Automotive and Materials Engineering, University of Windsor, Windsor (2005).
60. Ansys Fluent, www.fluent.com, (2012).
61. PCB-Piezotronics-http://www.pcb.com/techsupport/tech_pres.php, Introduction to Piezoelectric Pressure Sensors, http://www.pcb.com/techsupport/tech_pres.php.
62. Omega, www.omega.com, (2012).
63. A.-F. Kanta, M.-P. Planche, G. Montavon and C. Coddet, In-Flight and Upon Impact Particle Characteristics Modelling in Plasma Spray Process, *Surface and Coatings Technology* (2010), **204**, 1542-1548.
64. H. Assadi, T. Schmidt, H. Richter, J.-O. Kliemann, K. Binder, F. Gartner, T. Klassen and H. Kreye, On Parameter Selection in Cold Spraying, *Journal of Thermal Spray Technology* (2011), **20**, 1161-1176.

65. D. L. Gilmore, R. C. Dykhuizen, R. A. Neiser, T. J. Roemer and M. F. Smith, Particle Velocity and Deposition Efficiency in the Cold Spray Process, *Journal of Thermal Spray Technology* (1999), **8**, 576-582.
66. Y. Yin, Design Validation Testing of the Waverider: A Prototype Based on Shockwave Induced Spraying Process, *CenterLine (Windsor) Limited* (2011).

Appendix A Written Permission from the Copyright Holders



<http://www.elsevier.com>

[About Elsevier](#) > Rights & Responsibilities

Author Rights & Responsibilities

At Elsevier, we request transfers of copyright, or in some cases exclusive rights, from our journal authors in order to ensure that we have the rights necessary for the proper administration of electronic rights and online dissemination of journal articles. Authors and their employers retain (or are granted/transferred back) significant scholarly rights in their work. We take seriously our responsibility as the steward of the online record to ensure the integrity of scholarly works and the sustainability of journal business models, and we actively monitor and pursue unauthorized and unsubscribed uses and re-distribution (for subscription models).

In addition to [authors' scholarly rights](#), authors have certain responsibilities for their work, particularly in connection with [publishing ethics issues](#).

- Rights
- FAQ
- Responsibilities
- Permissions

As a journal author, you have rights for a large range of uses of your article, including use by your employing institute or company. These rights can be exercised without the need to obtain specific permission.

How authors can use their own journal articles

Authors publishing in Elsevier journals have wide rights to use their works for teaching and scholarly purposes without needing to seek permission.

Table of Authors' Rights

	Preprint version (with a few exceptions- see below *)	Accepted Author Manuscript	Published Journal Articles
Use for classroom teaching by author or author's institution and presentation at a meeting or conference and distributing copies to attendees	Yes	Yes	Yes
Use for internal training by author's company	Yes	Yes	Yes
Distribution to colleagues for their research use	Yes	Yes	Yes
Use in a subsequent compilation of the author's works	Yes	Yes	Yes
Inclusion in a thesis or dissertation	Yes	Yes	Yes

Related Links

[Elsevier principles and policies](#) >

[ScienceDirect](#) >

Access peer-reviewed full-text articles through ScienceDirect.

[Elsevier Author WebShop](#) >

Language editing and illustration services for your manuscripts, personal reprints, Personal Selections for iPads and more.



Reuse of portions or extracts from the article in other works	Yes	Yes with full acknowledgement of final article	Yes with full acknowledgement of final article
Preparation of derivative works (other than for commercial purposes)	Yes	Yes with full acknowledgement of final article	Yes with full acknowledgement of final article
Preprint servers	Yes	Yes with the specific written permission of Elsevier	No
Voluntary posting on open web sites operated by author or author's institution for scholarly purposes	Yes (author may later add an appropriate bibliographic citation, indicating subsequent publication by Elsevier and journal title)	Yes, with appropriate bibliographic citation and a link to the article once published	Only with the specific written permission of Elsevier
Mandated deposit or deposit in or posting to subject-oriented or centralized repositories	Yes under specific agreement between Elsevier and the repository	Yes under specific agreement between Elsevier and the repository**	Yes under specific agreement between Elsevier and the repository
Use or posting for commercial gain or to substitute for services provided directly by journal	Only with the specific written permission of Elsevier	Only with the specific written permission of Elsevier	Only with the specific written permission of Elsevier

**Voluntary posting of Accepted Author Manuscripts in the arXiv subject repository is permitted.

Examples of use or posting for commercial gain:

- Posting by companies of employee-authored works for use by customers of those companies (e.g. pharmaceutical companies and physician prescribers)
- Commercial exploitation such as directly associating advertising with posting or charging fees for document delivery or access

*Which journals have different preprint policies?

If an electronic preprint of an article is placed on a public server prior to its submission to an Elsevier journal, this is not generally viewed by Elsevier as 'prior publication' and will not disqualify the article from further consideration by Elsevier, nor will Elsevier require the removal of that preprint version.

However Cell Press and The Lancet have different preprint policies and will not consider for publication articles that have already been posted publicly. This is a rule agreed upon by The International Committee of Medical Journal Editors. Information on [Cell Press policy on preprints](#) is available, as is [The Lancet preprint policy](#). There are a number of other journals published by Elsevier (principally journals published on behalf of third party owners) that also have their own preprint policies which will be set out in the Guide for Authors for the relevant journal.

Does Elsevier request a transfer of copyright?

Elsevier requests a transfer of copyright for articles published under subscription-based business models but we generally use different licensing approaches for other publishing models where we offer authors a variety of Creative Commons licenses for some of our author-pays journals and are piloting a range of options. [Learn more](#) about Creative

Commons licenses.

For subscription-based publishing, we ask for a transfer of copyright for a number of reasons, mainly because:

- i. By having the ability to exercise all rights under copyright, Elsevier is able to quickly launch new products and services, and to make agreements with other platforms and services to enrich published content and to make it more accessible and usable. Authors may be based in a number of different countries, which will have their own copyright regimes. Copyright assignments give more legal certainty, particularly in relation to future rights in new technologies.
- ii. Elsevier uses copyright to protect the integrity of the journal articles in cases of plagiarism, copyright infringement and other third party infringements. The journal subscription business model depends on a substantial body of subscribing customers providing financial support to a particular journal, and "free-riding" infringements diminish this model.
- iii. An assignment of rights under copyright means that we can more easily show that we own the rights and do not have to seek the participation of the author or obtain power of attorney from the author in order to bring an enforcement action.

Remember, even though we ask for a transfer of copyright, our journal authors retain (or are granted back) significant scholarly rights, as outlined above.

For a more detailed discussion, see the [STM Position Paper](#) on the benefits of copyright assignments.

Does Elsevier claim rights in an author's supporting data?

Elsevier supports the general principle that raw research data should be made freely available to all researchers and encourages the public posting of the raw data outputs of research. (Note that this is distinct from charts, tables, etc. which may be included within an article and in which rights would be transferred or licensed to Elsevier as part of the article, in the same way as text, illustrations or photographs). Elsevier therefore does not claim rights in the raw datasets that may be submitted with an article and the author can make these datasets freely available from other (web) locations.

If supported by the author and journal editor, and when a dataset is hosted in a repository that ensures data integrity and supports long-term preservation and inward linking, Elsevier can further support the discoverability of that dataset by connecting it with the published journal article on ScienceDirect through linking from an article or entity or through article interoperability. [Click here](#) to review examples of how this could work in practice.

For more information on industry positions on this issue supported by Elsevier, view the:

[Joint Statement from STM and DataCite](#) on the Linkability and Citability of Research Data, June 2012

[Brussels Declaration on STM Publishing](#), November 2007

[STM/ALPSP Statement](#), June 2006

Can I post my published journal article on open websites?

A published journal article is the definitive final record of published research that appears in the journal and embodies all value-adding publisher activities, including copy editing, formatting and, if relevant, pagination, along with the stewardship of the scholarly record.

You can use your branded and formatted published article for all of the personal and institutional purposes described above. However, in order to safeguard the correct scientific record, Elsevier does not permit the posting of published journal articles (either the pdf provided by Elsevier or HTML files) on any open websites.

As part of its contribution to the stewardship of the scientific literature, Elsevier works with third parties (e.g. national libraries) to preserve its journal articles for posterity and in perpetuity, and invests to drive their usage. Elsevier strictly enforces an absolute guideline on the location of its published journal articles: each branded and formatted published journal article will reside only on a completely controlled site because this is the only way that we as the publisher can guarantee that each published journal article is permanent,

authentic and unaltered as part of the 'minutes of science'.

Since Elsevier adds significant value to the final published journal article, we need to take these steps to ensure that this value is maintained, both for Elsevier and for our authors. However, we view preprints and accepted author manuscripts as less formal versions of the article and we therefore take a more liberal approach towards these, as described in more detail on our [Article Posting Policies](#) information page.

Copyright Transfer Statement

The copyright to this article, including any graphic elements therein (e.g. illustrations, charts, moving images), is hereby assigned for good and valuable consideration to Springer Science+Business Media B.V. effective if and when the article is accepted for publication and to the extent assignable if assignability is restricted for by applicable law or regulations (e.g. for U.S. government or crown employees).

Author warrants (i) that he/she is the sole owner or has been authorized by any additional copyright owner to assign the right, (ii) that the article does not infringe any third party rights and no license from or payments to a third party is required to publish the article and (iii) that the article has not been previously published or licensed. The copyright assignment includes without limitation the exclusive, assignable and sublicensable right, unlimited in time and territory, to reproduce, publish, distribute, transmit, make available and store the article, including abstracts thereof, in all forms of media of expression now known or developed in the future, including pre- and reprints, translations, photographic reproductions and microform. Springer may use the article in whole or in part in electronic form, such as use in databases or data networks for display, print or download to stationary or portable devices. This includes interactive and multimedia use and the right to alter the article to the extent necessary for such use.

An author may self-archive an author-created version of his/her article on his/her own website and/or the repository of Author's department or faculty. Author may also deposit this version on his/her funder's or funder's designated repository at the funder's request or as a result of a legal obligation, provided it is not made publicly available until 12 months after official publication by Springer. He/she may not use the publisher's PDF version, which is posted on www.springerlink.com, for the purpose of self-archiving or deposit. Furthermore, Author may only post his/her own version, provided acknowledgement is given to the original source of publication and a link is inserted to the published article on Springer's website. The link must be accompanied by the following text: "The final publication is available at www.springerlink.com".

Prior versions of the article published on non-commercial pre-print servers like arXiv.org can remain on these servers and/or can be updated with Author's accepted version. The final published version (in pdf or html/xml format) cannot be used for this purpose. Acknowledgement needs to be given to the final publication and a link must be inserted to the published article on Springer's website, accompanied by the text "The final publication is available at springerlink.com". Author retains the right to use his/her article for his/her further scientific career by including the final published journal article in other publications such as dissertations and postdoctoral qualifications provided acknowledgement is given to the original source of publication.

Author is requested to use the appropriate DOI for the article. Articles disseminated via www.springerlink.com are indexed, abstracted and referenced by many abstracting and information services, bibliographic networks, subscription agencies, library networks, and consortia.

After submission of the agreement signed by the corresponding author, changes of authorship or in the order of the authors listed will not be accepted by Springer.

**COPYRIGHT TRANSFER FORM**

Print

The following transfer agreement must be signed and returned to ASM International® before your manuscript and/or presentation slides can be published in the International Thermal Spray Conference and Exposition (ITSC)'s Conference Proceedings or other print/electronic publications produced by ASM International® or any of its Affiliate Societies.

Manuscript/Presentation Title: **Shockwave Induced Spraying Process: Effect of Parameters On Coating Performance**

Abstract ID#: **32546**

Names of All Authors: **Mr. Mo Karimi¹, Dr. Bertrand Jodoin² and Dr. Gary W. Rankin¹,**

¹Mechanical, Automotive and Materials Engineering, University of Windsor, Windsor, ON, Canada,

²Mechanical Engineering, University of Ottawa, Ottawa, ON, Canada

Copyright, title interest and all rights to the Article(s) are hereby assigned and transferred to ASM International® - Materials Park, Ohio 44073. The author(s) reserve(s) the following rights:

1. All proprietary rights other than copyright, such as patent rights.
2. The right to personally reuse all or portions of the content of the work in other works of his own authorship, including lectures, textbooks, reviews, and articles, provided proper notice of ASM International's copyright is given.
3. The right to post an electronic form of the final ASM International file of the work without revision or modification on the author's own personal or current employer's website, provided that such posting is noncommercial in nature and the work is made available to users without a fee or charge, and provided that proper notice of ASM's copyright is included.. Such posting shall include a link to the homepage of ASM International or a relevant ASM Affiliate Society.

The following statement must appear on the first page, or screen, of the work as posted:

 - Copyright [year; for example, 2011] ASM International This paper was published in [work bibliographic information] and is made available as an electronic reprint with the permission of ASM International. One print or electronic copy may be made for personal use only. Systematic or multiple reproduction, distribution to multiple locations via electronic or other means, duplications of any material in this paper for a fee or for commercial purposes, or modification of the content of this paper are prohibited.

In the case of work performed under U.S. Government contract, ASM International grants the U.S. Government royalty-free permission to reproduce all or portions of the Article, and to authorize others to do so for U.S. Government purposes. U.S. Government employees whose work is not subject to copyright may certify such employment status in Part B below.

By signing this Agreement, the authors warrant that this manuscript is their original work, does not infringe any copyright, does not violate any other right of any third parties, and that any required clearances from their own organization(s), contract sources, government agencies, etc., have been obtained prior to submitting the manuscript to ASM International. Signing this Agreement also gives permission to have the presentation recorded, including projected images, during the conference. The authors understand that the recording will be made available for purchase to members and other interested parties and hereby waive all claims and royalties in conjunction with such sales. The authors also understand that this agreement does not preclude them from publishing their presentation at any time.

If each author's signature does not appear below, the signing author(s) represent that they sign this Agreement as authorized agents for and on behalf of all the authors, and that this Agreement and

authorization is made on behalf of all the authors.

Has this manuscript been copyrighted, published, or submitted for publication elsewhere?

Please circle one: YES NO

Author Signature(s):

Fax or email this signed release form to: DeAna Morgan, ASM International, 9639 Kinsman Road, Materials Park, OH 44073 - (440) 338-4634 - deana.morgan@asminternational.org

www.gordonengland.co.uk/copyright.html

© **Copyright 1996-2013 Gordon England**

Most of the material featured on this site is subject to copyright protection.

The copyright protected material may be reproduced free of charge in any format or medium for education, research, private study or for internal circulation within an organisation.

This is subject to the material being reproduced accurately and not used in a misleading context. Where any of the copyright items on this site are being republished or copied to others, the source of the material must be identified and the copyright status acknowledged.

Any other proposed use of the material, you should apply for permission from Gordon England.

The permission to reproduce copyright material does not extend to any material on this site, which is identified as being the copyright of a third party. Authorisation to reproduce such material would need to be obtained from the copyright holders concerned.

The use of our logo is restricted and may not be used by other individuals or organisations without formal permission from us.



The logo for the Surface Engineering Forum is a dark rectangular box. Inside the box, the text "Surface Engineering Forum" is written in a light blue, sans-serif font. Below the text is a horizontal, glowing white streak that tapers to a point on the right side, resembling a laser beam or a stylized arrow.

Appendix B Profile for Valve Motion and Heater Temperature

((xposition transient 5 1)

(time

0.000

0.001222

0.011111

0.012333

0.066667

)

(x

0.000

-0.0007177

-0.0007177

0.000

0.000

)

)

((tuebtemp point 141)

(x

-1.095

-1.085

-1.075

-1.065

-1.055

-1.045

-1.035

-1.025

-1.015

-1.005

-0.995

-0.985

-0.975

-0.965

-0.955

-0.945

-0.935

-0.925

-0.915

-0.905

-0.895

-0.885

-0.875

-0.865

-0.855

-0.845

-0.835

-0.825

-0.815

-0.805

-0.795

-0.785

-0.775

-0.765
-0.755
-0.745
-0.735
-0.725
-0.715
-0.705
-0.695
-0.685
-0.675
-0.665
-0.655
-0.645
-0.635
-0.625
-0.615
-0.605
-0.595
-0.585
-0.575
-0.565
-0.555
-0.545
-0.535
-0.525
-0.515
-0.505
-0.495
-0.485
-0.475
-0.465
-0.455
-0.445
-0.435
-0.425
-0.415
-0.405
-0.395
-0.385
-0.375
-0.365
-0.355
-0.345
-0.335
-0.325
-0.315
-0.305
-0.295
-0.285
-0.275
-0.265
-0.255
-0.245
-0.235
-0.225
-0.215

-0.205
-0.195
-0.185
-0.175
-0.165
-0.155
-0.145
-0.135
-0.125
-0.115
-0.105
-0.095
-0.085
-0.075
-0.065
-0.055
-0.045
-0.035
-0.025
-0.015
-0.005
0.005
0.015
0.025
0.035
0.045
0.055
0.065
0.075
0.085
0.095
0.105
0.115
0.125
0.135
0.145
0.155
0.165
0.175
0.185
0.195
0.205
0.215
0.225
0.235
0.245
0.255
0.265
0.275
0.285
0.295
0.305
)
(temperature
300
303.7357143

307.4714286
311.2071429
314.9428572
318.6785715
322.4142858
326.1500001
329.8857144
333.6214287
337.357143
341.0928573
344.8285716
348.5642859
352.3000002
356.0357145
359.7714288
363.5071431
367.2428574
370.9785717
374.714286
378.4500003
382.1857146
385.9214289
389.6571432
393.3928575
397.1285718
400.8642861
404.6000004
408.3357147
412.071429
415.8071433
419.5428576
423.2785719
427.0142862
430.7500005
434.4857148
438.2214291
441.9571434
445.6928577
449.428572
453.1642863
456.9000006
460.6357149
464.3714292
468.1071435
471.8428578
475.5785721
479.3142864
483.0500007
486.785715
490.5214293
494.2571436
497.9928579
501.7285722
505.4642865
509.2000008
512.9357151

516.6714294
520.4071437
524.142858
527.8785723
531.6142866
535.3500009
539.0857152
542.8214295
546.5571438
550.2928581
554.0285724
557.7642867
561.500001
565.2357153
568.9714296
572.7071439
576.4428582
580.1785725
583.9142868
587.6500011
591.3857154
595.1214297
598.857144
602.5928583
606.3285726
610.0642869
613.8000012
617.5357155
621.2714298
625.0071441
628.7428584
632.4785727
636.214287
639.9500013
643.6857156
647.4214299
651.1571442
654.8928585
658.6285728
662.3642871
666.1000014
669.8357157
673.57143
677.3071443
681.0428586
684.7785729
688.5142872
692.2500015
695.9857158
699.7214301
703.4571444
707.1928587
710.928573
714.6642873
718.4000016
722.1357159

725.8714302
729.6071445
733.3428588
737.0785731
740.8142874
744.5500017
748.285716
752.0214303
755.7571446
759.4928589
763.2285732
766.9642875
770.7000018
774.4357161
778.1714304
781.9071447
785.642859
789.3785733
793.1142876
796.8500019
800.5857162
804.3214305
808.0571448
811.7928591
815.5285734
819.2642877
823.000002
)
)

Appendix C User-Defined Function to Model Heat Transfer under High-Mach-Number Gas-Particle Relative Flow

```
#include "udf.h"
#include "dpm.h

//#define RE_NUMBER(rho,v,d,mu) (rho*v*d/mu)
#define PR_NUMBER(cpg,mu,k) (cpg*mu/k)
#define MA_NUMBER(v,gamma,r,t) (v/sqrt(gamma*r*t))
#define pi 3.14159265
```

```
/*
12.3.8 Convective Heat and Mass Transfer Modeling
```

In FLUENT, turbulent heat transport is modeled using the concept of Reynolds' analogy to turbulent momentum transfer. The "modeled" energy equation is thus given by the following:

$$\frac{\partial}{\partial t} (\rho E) + \frac{\partial}{\partial x_j} (u_j (\tau_{ij})_{\text{eff}}) + S_h \quad (12.3-18)$$

where k , in this case, is the thermal conductivity, E is the total energy, and $(\tau_{ij})_{\text{eff}}$ is the deviatoric stress tensor, defined as

$$(\tau_{ij})_{\text{eff}} = \mu_{\text{eff}} \left(\frac{\partial u_i}{\partial x_j} + \frac{\partial u_j}{\partial x_i} - \frac{2}{3} \frac{\partial u_k}{\partial x_k} \delta_{ij} \right)$$

The term involving $(\tau_{ij})_{\text{eff}}$ represents the viscous heating, and is always computed in the density-based solvers. It is not computed by default in the pressure-based solver, but it can be enabled in the Viscous Model panel. The default value of the turbulent Prandtl number is 0.85. You can change the value of Pr t in the Viscous Model panel.

Turbulent mass transfer is treated similarly, with a default turbulent Schmidt number of 0.7. This default value can be changed in the Viscous Model panel.

Wall boundary conditions for scalar transport are handled analogously to momentum, using the appropriate "law-of-the-wall".

3.2.3 Cell Macros

```
.
.
.
Material Property Macros
```

The macros listed in Tables 3.2.14- 3.2.16 can be used to return real material property variables in SI units. The variables are available in

both the pressure-based and the density-based solver. Argument `real prt` is the turbulent Prandtl number. Definitions for material property macros can be found in the referenced header file (e.g., `mem.h`).

Table 3.2.14: Macros for Diffusion Coefficients Defined in `mem.h` Macro Argument Types Returns

Macro	Argument Types	Returns
<code>C_MU_L(c,t)</code>	<code>cell_t c, Thread *t</code>	laminar viscosity
<code>C_MU_T(c,t)</code>	<code>cell_t c, Thread *t</code>	turbulent viscosity
<code>C_MU_EFF(c,t)</code>	<code>cell_t c, Thread *t</code>	effective viscosity
<code>C_K_L(c,t)</code>	<code>cell_t c, Thread *t</code>	thermal conductivity
<code>C_K_T(c,t,prt)</code>	<code>cell_t c, Thread *t, real prt</code>	turbulent thermal conductivity
<code>C_K_EFF(c,t,prt)</code>	<code>cell_t c, Thread *t, real prt</code>	effective thermal conductivity
<code>C_DIFF_L(c,t,i,j)</code>	<code>cell_t c, Thread *t, int i, int j</code>	laminar species diffusivity
<code>C_DIFF_EFF(c,t,i)</code>	<code>cell_t c, Thread *t, int i</code>	effective species diffusivity

```

*/

//#define PrTurb 0.85

DEFINE_DPM_LAW(rmgeneral,p,ci)
{
  cell_t c = P_CELL(p);
  Thread *t = P_CELL_THREAD(p);
  real h, gamma, betap;
  real d = P_DIAM(p);
  real Ap = pi*d*d;
  //real k = C_K_EFF(c,t,PrTurb);
  real k = C_K_L(c,t);
  real mu_lam = C_MU_L(c,t);
  //real mu_eff = C_MU_EFF(c,t);
  real cpg = C_CP(c,t);
  real r = C_RGAS(c,t);
  real tg = C_T(c,t);
  real tp = P_T(p);
  real NV_VEC(v), vel, Re, Pr, Ma, Nu;

  NV_DD(v,=,C_U(c,t),C_V(c,t),C_W(c,t),-
,P_VEL(p)[0],P_VEL(p)[1],P_VEL(p)[2]);
  vel = NV_MAG(v);

  gamma = cpg/(cpg-r);

  Re = RE_NUMBER(C_R(c,t),vel,d,mu_lam);
  Pr = PR_NUMBER(cpg,mu_lam,k);
  Ma = MA_NUMBER(vel,gamma,r,tg);
  //Nu = (2. + 0.6*sqrt(Re)*pow(Pr,1./3.));

  if (Ma>0.24 && tg>tp)

```

```

        Nu = 2. + 0.44*sqrt(Re)*pow(Pr,1./3.)*exp(0.1+0.872*Ma);
else
        Nu = 2. + 0.6*sqrt(Re)*pow(Pr,1./3.);

h = k*Nu/d;

/*
22.9.2 Particle Types in FLUENT
Eq. 22.9.13-22.9.16
with no radiation alphap = tg
*/

betap = (Ap*h)/(P_MASS(p)*DPM_SPECIFIC_HEAT(p,tp));

// Message ("d=%g, Ap=%g, k=%g, mu_lam=%g, mu_eff=%g, Cpg=%g, R=%g,
Tg=%g, Tp=%g \n", d, Ap, k, mu_lam, mu_eff, cpg, r, tg, tp);
// Message ("U=%g, V=%g, W=%g, Up=%g, Vp=%g, Wp=%g, Vr=%g, Re=%g,
Pr=%g, Ma=%g, Nu=%g\n",
C_U(c,t),C_V(c,t),C_W(c,t),P_VEL(p)[0],P_VEL(p)[1],P_VEL(p)[2], vel,
Re, Pr, Ma, Nu);
// Message ("gamm=%g, Dt=%g, rho_g=%g, h=%g, m_p=%g, k_p=%g, betap=%g,
", gamma, P_DT(p), C_R(c,t), h, P_MASS(p), DPM_SPECIFIC_HEAT(p,tp),
betap);

P_T(p) = tg + (tp-tg)*exp(-betap*P_DT(p));

// Message ("Tp=%g \n", P_T(p));

//P_T(p) = tp+(P_DT(p)*h*A)/(P_MASS(p)*DPM_SPECIFIC_HEAT(p,tp))*(tg-
tp);
}

```

Appendix D Effect of Radial Location of Particle Injection

Comparison of speed and temperature of 20-micron aluminum particles upon impacting on substrate:

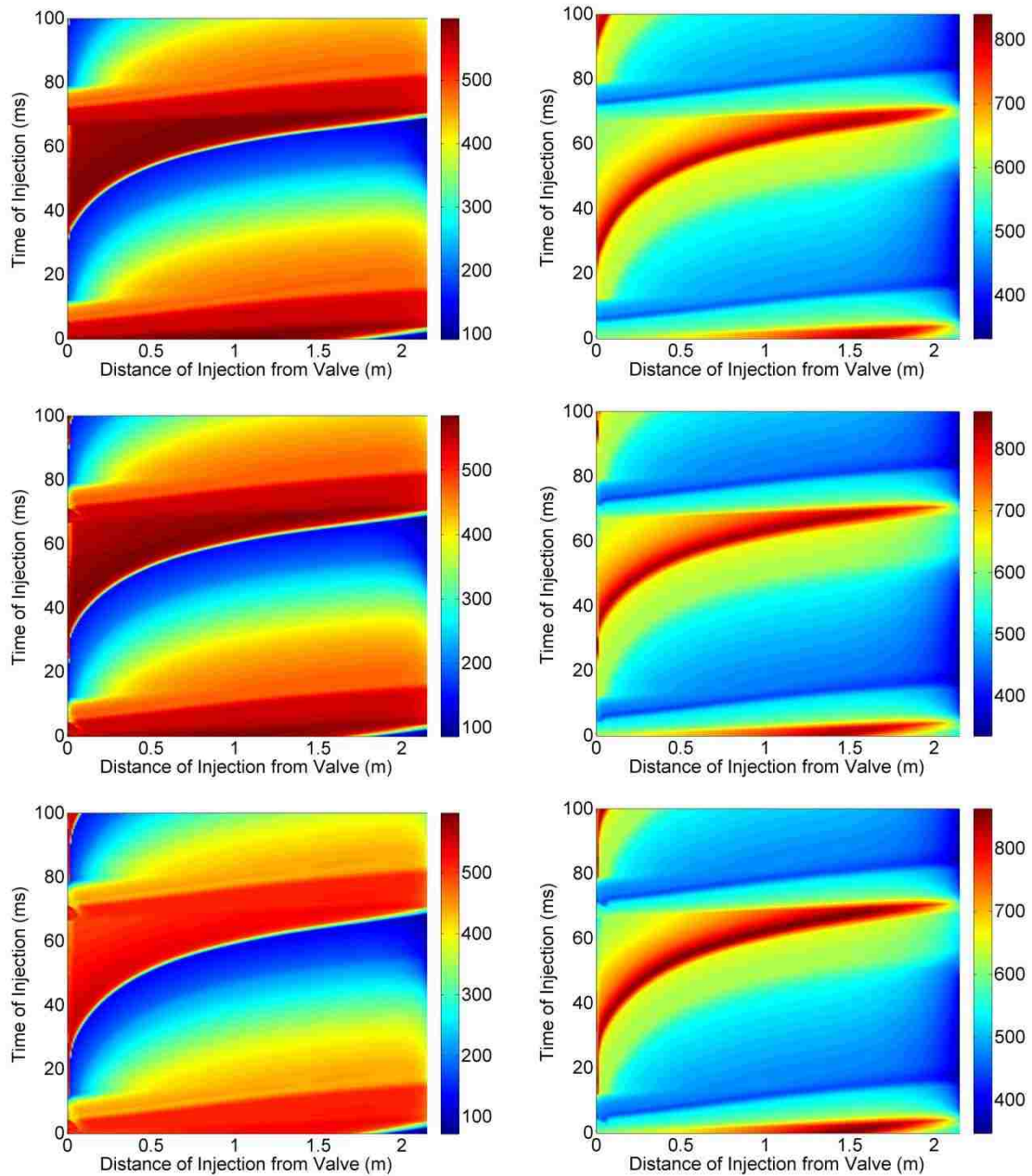


Figure D1: Speed (left) and temperature (right) of 20-micron aluminum particles upon impacting on substrate, initiated at 0.0R (top), 0.5R (center), and 0.8R (bottom)

Comparison of speed and temperature of 20-micron copper particles upon impacting on substrate:

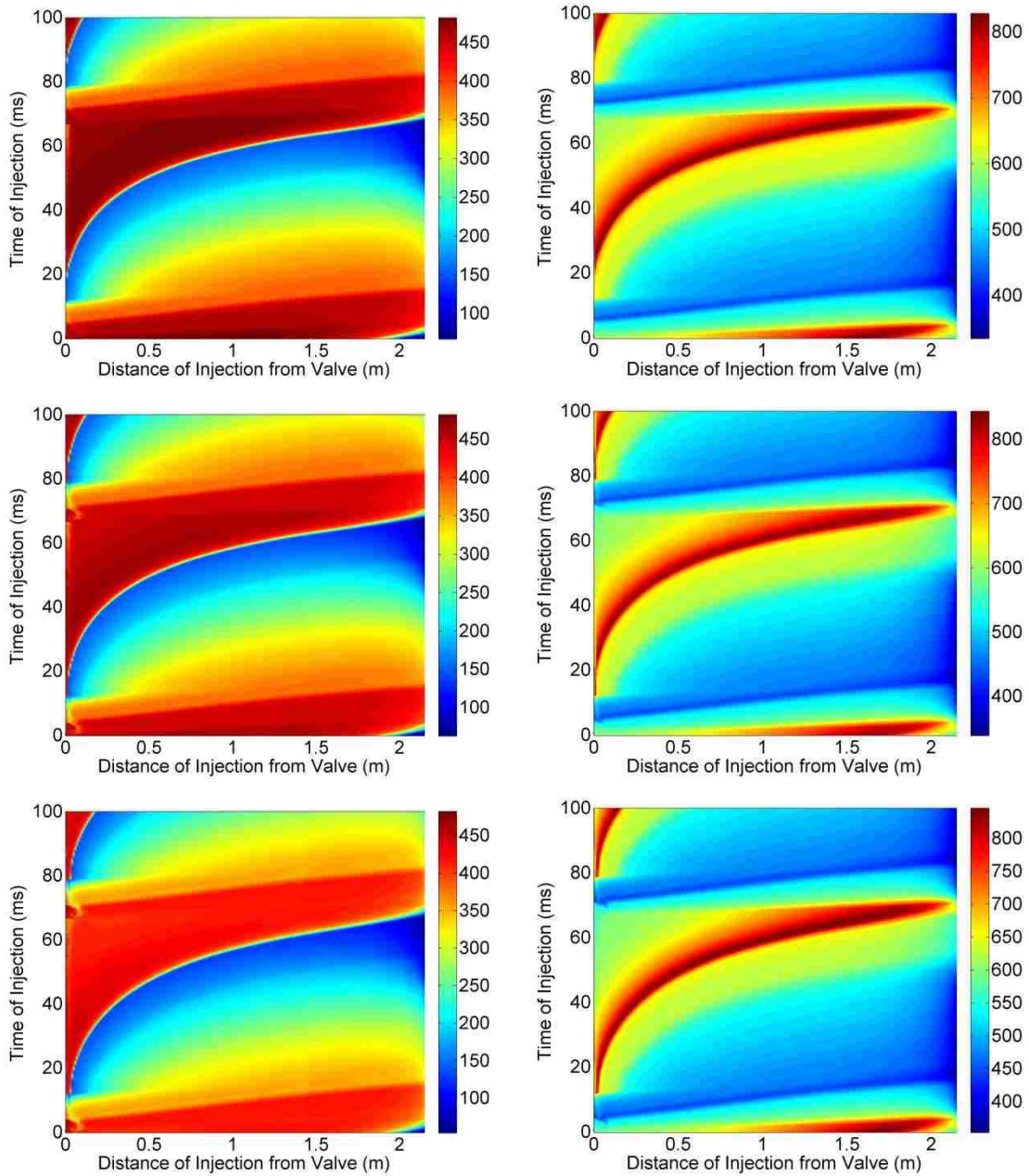


Figure D2: Speed (left) and temperature (right) of 20-micron copper particles upon impacting on substrate, initiated at 0.0R (top), 0.5R (center), and 0.8R (bottom)

Comparison of speed and temperature of 20-micron stainless steel particles upon impacting on substrate:

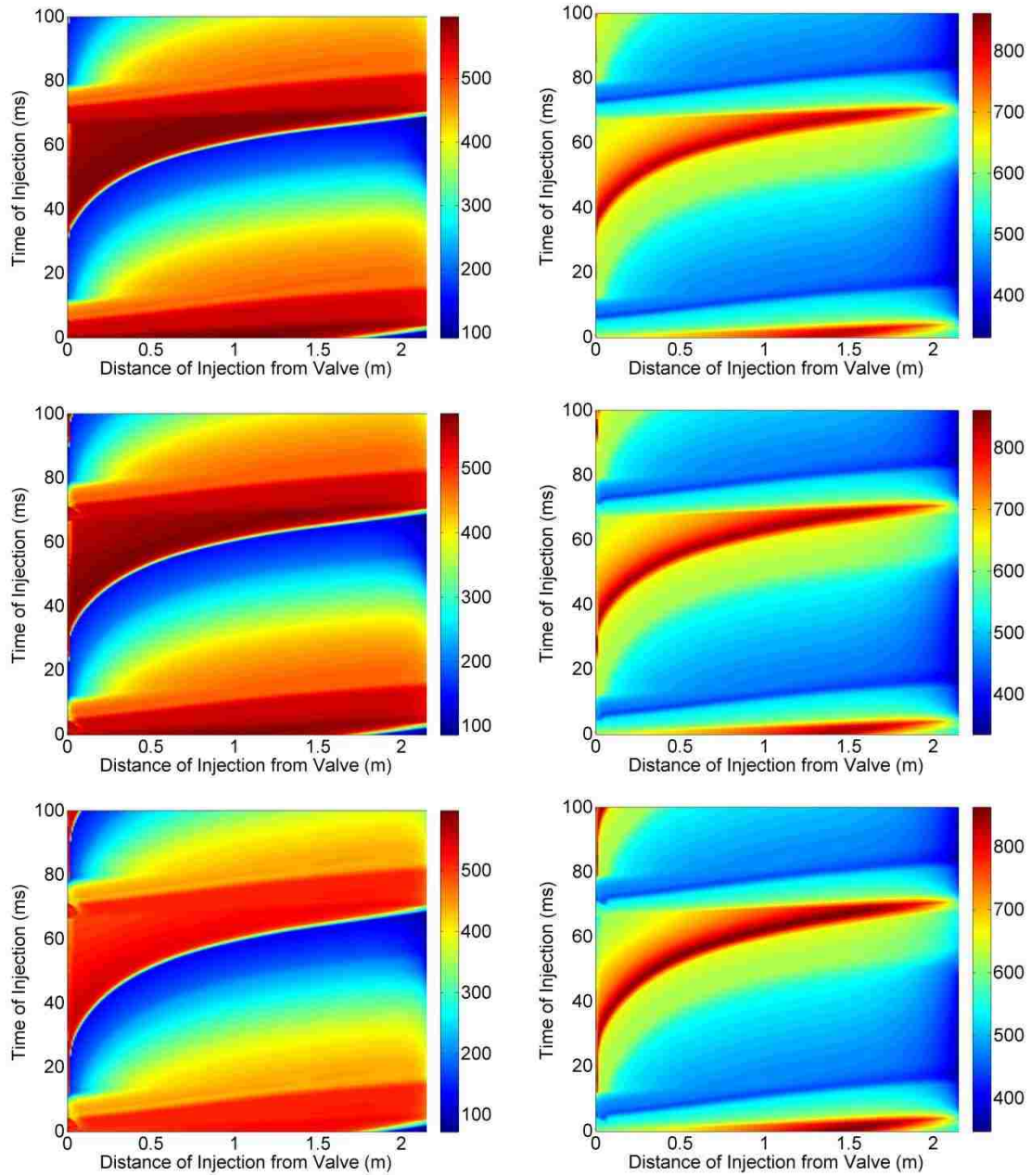


Figure D3: Speed (left) and temperature (right) of 20-micron stainless steel particles upon impacting on substrate, initiated at 0.0R (top), 0.5R (center), and 0.8R (bottom)

Comparison of V/V_{cr} value of 20-micron aluminum particles upon impacting on substrate:

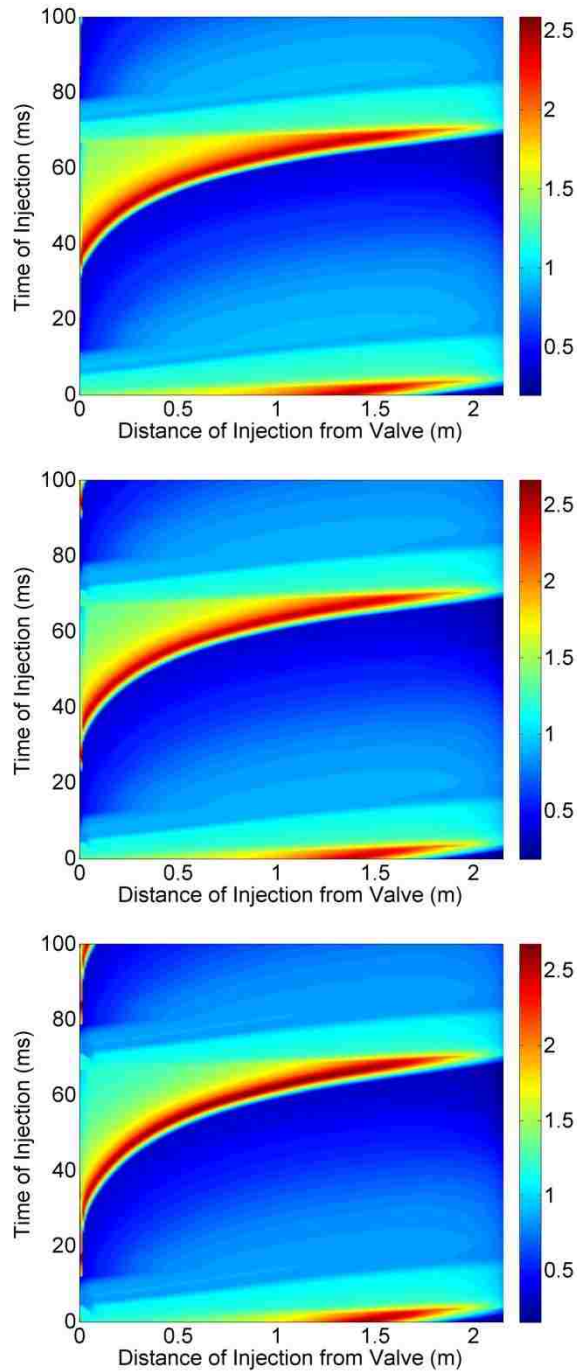


Figure D4: V/V_{cr} values for 20-micron aluminum particles upon impacting on substrate, initiated at 0.0R (top), 0.5R (middle), and 0.8R (bottom)

Comparison of V/V_{cr} value of 20-micron copper particles upon impacting on substrate:

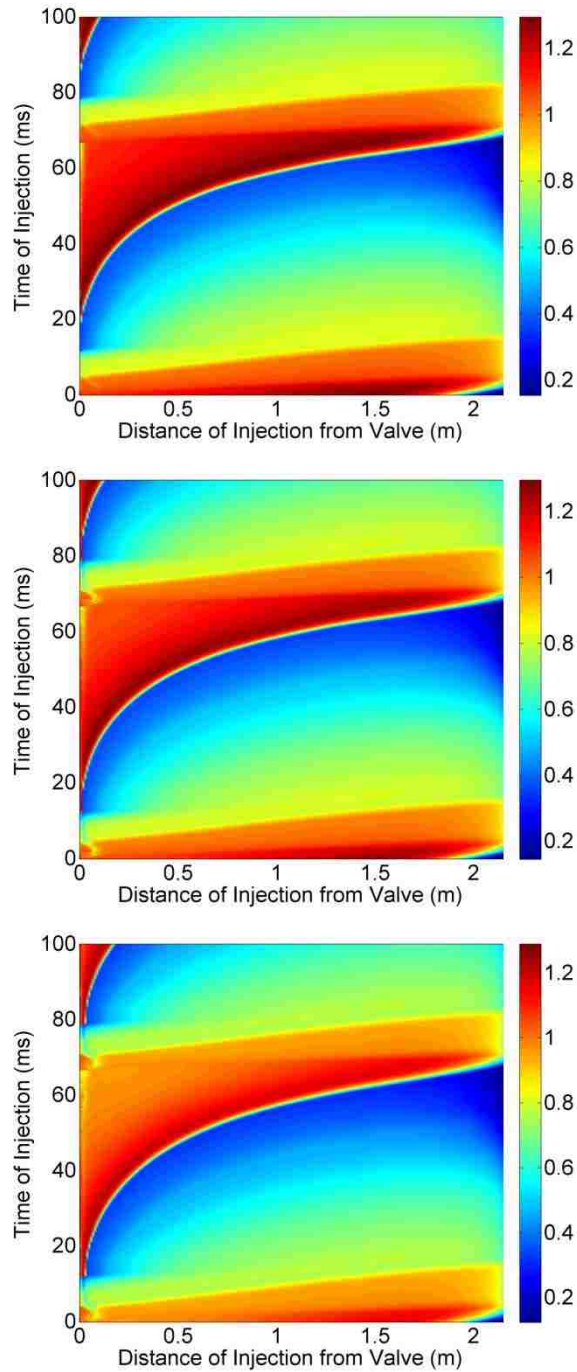


Figure D5: V/V_{cr} values for 20-micron copper particles upon impacting on substrate, initiated at 0.0R (top), 0.5R (middle), and 0.8R (bottom)

Comparison of V/V_{cr} value of 20-micron stainless steel particles upon impacting on substrate:

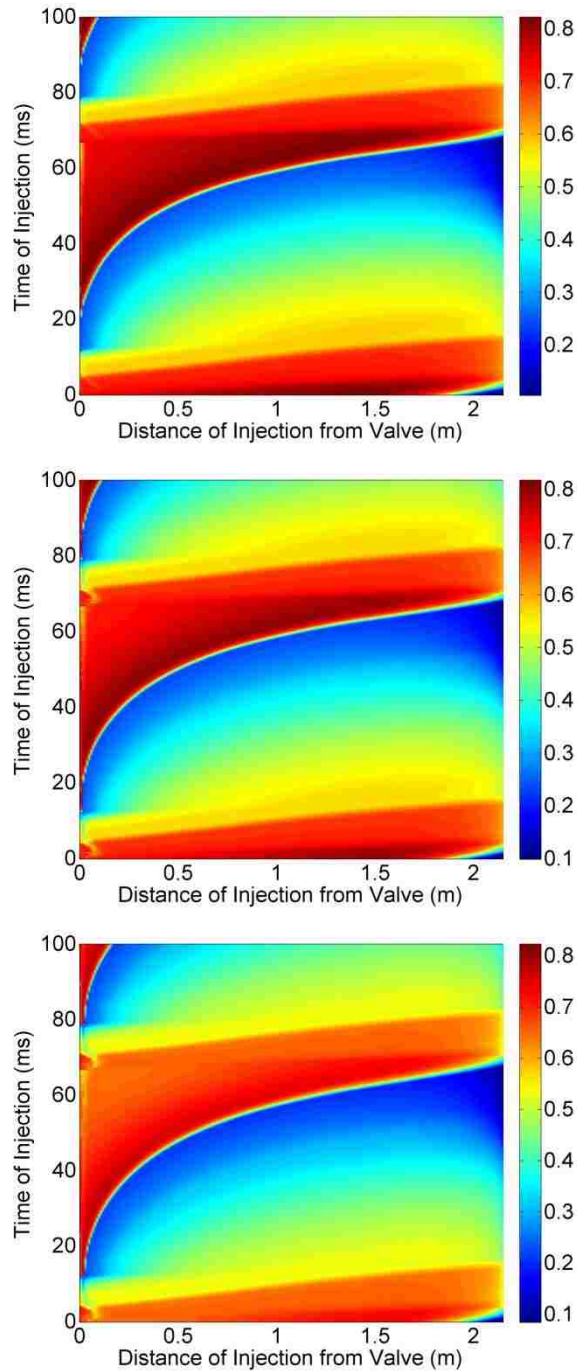


Figure D6: V/V_{cr} values for 20-micron stainless steel particles upon impacting on substrate, initiated at 0.0R (top), 0.5R (middle), and 0.8R (bottom)

Appendix E Journal File for Extracting Data on the Centerline

```
/ file read-case-data 2d-30_ss-setup.cas.gz
/ file export ascii 2d-42Data-Points (14) y pressure total-
pressure density velocity-magnitude axial-velocity mach-number
temperature total-temperature viscosity-turb q n

/ file read-case-data 2d-42_ts-0.066700.cas.gz
/ file export ascii 2d-4206670 (14) y pressure total-pressure
density velocity-magnitude axial-velocity mach-number temperature
total-temperature viscosity-turb q n
/ file read-case-data 2d-42_ts-0.066800.cas.gz
/ file export ascii 2d-4206680 (14) y pressure total-pressure
density velocity-magnitude axial-velocity mach-number temperature
total-temperature viscosity-turb q n
/ file read-case-data 2d-42_ts-0.066900.cas.gz
/ file export ascii 2d-4206690 (14) y pressure total-pressure
density velocity-magnitude axial-velocity mach-number temperature
total-temperature viscosity-turb q n
/ file read-case-data 2d-42_ts-0.067000.cas.gz
/ file export ascii 2d-4206700 (14) y pressure total-pressure
density velocity-magnitude axial-velocity mach-number temperature
total-temperature viscosity-turb q n
/ file read-case-data 2d-42_ts-0.067100.cas.gz
/ file export ascii 2d-4206710 (14) y pressure total-pressure
density velocity-magnitude axial-velocity mach-number temperature
total-temperature viscosity-turb q n
/ file read-case-data 2d-42_ts-0.067200.cas.gz
/ file export ascii 2d-4206720 (14) y pressure total-pressure
density velocity-magnitude axial-velocity mach-number temperature
total-temperature viscosity-turb q n
/ file read-case-data 2d-42_ts-0.067300.cas.gz
/ file export ascii 2d-4206730 (14) y pressure total-pressure
density velocity-magnitude axial-velocity mach-number temperature
total-temperature viscosity-turb q n
/ file read-case-data 2d-42_ts-0.067400.cas.gz
/ file export ascii 2d-4206740 (14) y pressure total-pressure
density velocity-magnitude axial-velocity mach-number temperature
total-temperature viscosity-turb q n
/ file read-case-data 2d-42_ts-0.067500.cas.gz
/ file export ascii 2d-4206750 (14) y pressure total-pressure
density velocity-magnitude axial-velocity mach-number temperature
total-temperature viscosity-turb q n
/ file read-case-data 2d-42_ts-0.067600.cas.gz
/ file export ascii 2d-4206760 (14) y pressure total-pressure
density velocity-magnitude axial-velocity mach-number temperature
total-temperature viscosity-turb q n
/ file read-case-data 2d-42_ts-0.067700.cas.gz
```

```
/ file export ascii 2d-4206770 (14) y pressure total-pressure
density velocity-magnitude axial-velocity mach-number temperature
total-temperature viscosity-turb q n
/ file read-case-data 2d-42_ts-0.067800.cas.gz
/ file export ascii 2d-4206780 (14) y pressure total-pressure
density velocity-magnitude axial-velocity mach-number temperature
total-temperature viscosity-turb q n
/ file read-case-data 2d-42_ts-0.067900.cas.gz
/ file export ascii 2d-4206790 (14) y pressure total-pressure
density velocity-magnitude axial-velocity mach-number temperature
total-temperature viscosity-turb q n
/ file read-case-data 2d-42_ts-0.068000.cas.gz
/ file export ascii 2d-4206800 (14) y pressure total-pressure
density velocity-magnitude axial-velocity mach-number temperature
total-temperature viscosity-turb q n
/ file read-case-data 2d-42_ts-0.068100.cas.gz
/ file export ascii 2d-4206810 (14) y pressure total-pressure
density velocity-magnitude axial-velocity mach-number temperature
total-temperature viscosity-turb q n
```

Appendix F MATLAB Codes to Generate x-t Contours of Flow Variables

Main Program: xtplot.m

```
clear all;

% Set up the case, text to appear on title, time period and limits of x
% after shifting in position.
casedescription = ' Air, 2MPa, 300C, Valve 1-0-2ms';
sizeoftext = 20;
timestart = 0; timestep = 0.05; timeend = 10;
limitsofx = [0 1];

datafilenamecommon = '2d-28';
importfile([datafilenamecommon 'Data-Points']);

coordinates = data(:, 2:3);
variablenames = textdata;
clear data textdata colheaders;

position = coordinates(:, 1);
positioncount = length(position);
time = (timestart:timestep:timeend); timecount = length(time);

Z = zeros(timecount, positioncount);

% Shift zero in position axes on the start of the domain (after valve)
posmin = min(position);
shiftedposition = position - posmin;

for column = 4:length(variablenames)
    variablename = strtrim(variablenames(column));

    for j = 0:timecount-1
        jtime = 100*timestep*j;
        jthousands = floor(jtime/1000); jtime = jtime-1000*jthousands;
        jhundreds = floor(jtime/100); jtime = jtime-100*jhundreds;
        jtens = floor(jtime/10); jtime = jtime-10*jtens;
        jones = floor(jtime);
        jfilename = [datafilenamecommon char(48+jthousands)
char(48+jhundreds) char(48+jtens) char(48+jones)];
        importfile(jfilename);
        Z(j+1, :) = dataextract(data, column, position);
    end
end
```

```

h=figure;
axes('fontsize', sizeoftext)
pcolor(shiftedposition, time, Z)
colormap(jet)
shading interp

switch char(variablename)
    case 'pressure'
        scale = [0 1.3e6];
        variabletitle = ' Static Pressure (Pa)';
    case 'total-pressure'
        scale = [0 2.3e6];
        variabletitle = ' Total Pressure (K)';
    case 'density'
        scale = [0 15];
        variabletitle = ' Density (kg/m^3)';
    case 'velocity-magnitude'
        scale = [0 1100];
        variabletitle = ' Valocity Magnitude (m/s)';
    case 'axial-velocity'
        scale = [-100 1100];
        variabletitle = ' Axial Valocity (m/s)';
    case 'mach-number'
        scale = [0 2.5];
        variabletitle = ' Mach Number';
    case 'temperature'
        scale = [0 1300];
        variabletitle = ' Static Temperature (K)';
    case 'total-temperature'
        scale = [0 1300];
        variabletitle = ' Total Temperature (K)';
    case 'viscosity-turb'
        variabletitle = ' Turbulent Viscosity (kg/m-s)';
        scale = [0 0.04];
end

    %title(strcat('Contours of', variabletitle, ' -', casedescription),
'fontsize', sizeoftext)
    xlabel('Distance from Valve (m)', 'fontsize', sizeoftext)
    ylabel('Time (ms)', 'fontsize', sizeoftext)
    colorbar('EastOutside', 'fontsize', sizeoftext)

    %Set the limits of the plot, in x direction
    %xlim(limitsofx)

    %Set the color scale - prescribed in the second line of each case
switch above
    caxis(scale)

    print(h, '-djpeg90', '-r600', char(variablename));
end

```


Function I: importfile.m

```
function importfile(fileToRead1)
%IMPORTFILE(FILETOREAD1)
% Imports data from the specified file
% FILETOREAD1: file to read

% Auto-generated by MATLAB on 15-Jul-2010 17:20:58

% Import the file
newData1 = importdata(fileToRead1);

% Create new variables in the base workspace from those fields.
vars = fieldnames(newData1);
for i = 1:length(vars)
    assignin('base', vars{i}, newData1.(vars{i}));
end
```

Function II: dataextract.m

```
function extracted = dataextract(dataset, columnnumber, positionvector)

% Extract a vector from a given column of the data set based on a
% position
% vector, discarding data points whose positions do not match the
% position
% vector
targetlength = length(positionvector);
%rawlength = length(dataset(:, columnnumber));
extracted = zeros(1, targetlength);

icoordinates = dataset(:, 2:3);
iposition = icoordinates(:, 1);
for i = 1:targetlength
    ipositionpointer = 1;
    while not(iposition(ipositionpointer) == positionvector(i)),
        ipositionpointer = ipositionpointer+1;
    end
    extracted(1, i) = dataset(ipositionpointer, columnnumber);
end
```

Appendix G MATLAB Codes to Generate Time History Plots of Flow Variables

Main Program: timehistory.m

```
clear all;

% Set up the case, text to appear on title, time period and limits of x
% after shifting in position.
casedescription = ' N, 2MPa, 550C, Valve 1.2-11.1-1.2ms';
sizeoftext = 20;
timestart = 66.7; timestep = 0.1; timeend = 133.3; timeshift = -66.7;
limitsofx = [0 1];
targetlocations = [1129 404 10 1];

datafilenamecommon = '2d-42';
importfile([datafilenamecommon 'Data-Points']);

coordinates = data(:, 2:3);
variablenames = textdata;
clear data textdata colheaders;

position = coordinates(:, 1);
positioncount = length(position);
time = (timestart:timestep:timeend); timecount = length(time);

Z = zeros(timecount, positioncount);

% Shift zero in position axes on the start of the domain (after valve)
posmin = min(position);
shiftedposition = position - posmin;
time = time + timeshift;

for column = 4:length(variablenames)
    variablename = strtrim(variablenames(column));

    for j = 0:timecount-1
        jtimeactual = timestart + timestep*j;
        jtime = jtimeactual*100;
        jtenthousands = floor(jtime/10000 + 0.0000001); jtime = jtime-
10000*jtenthousands;
        jthousands = floor(jtime/1000 + 0.0000001); jtime = jtime-
1000*jthousands;
        jhundreds = floor(jtime/100 + 0.0000001); jtime = jtime-
100*jhundreds;
        jtens = floor(jtime/10 + 0.0000001); jtime = jtime-10*jtens;
```

```

        jones = floor(jtime + 0.0000001);
        jfilename = [datafilenamecommon char(48+jtenths)
char(48+jthousands) char(48+jhundreds) char(48+jtens) char(48+jones)];
        importfile(jfilename);
        Z(j+1, :) = dataextract([data(:,2) data(:,column)], position);
    end

h=figure;
axes('fontsize', sizeoftext)
plot(time, Z(:,1129), time, Z(:,404), time, Z(:,10), time, Z(:,1))
%pcolor(shiftedposition, time, Z)
%colormap(jet)
%shading interp

switch char(variablename)
    case 'pressure'
        %scale = [0 1.6e6];
        variabletitle = ' Static Pressure (psi)';
        %plot(time, Z(:,384)/6895, time, Z(:,1029)/6895)
    case 'total-pressure'
        %scale = [0 2.3e6];
        variabletitle = ' Total Pressure (K)';
    case 'density'
        %scale = [0 15];
        variabletitle = ' Density (kg/m^3)';
    case 'velocity-magnitude'
        %scale = [0 2500];
        variabletitle = ' Valocity Magnitude (m/s)';
    case 'axial-velocity'
        %scale = [-100 2500];
        variabletitle = ' Axial Valocity (m/s)';
    case 'mach-number'
        %scale = [0 2.5];
        variabletitle = ' Mach Number';
    case 'temperature'
        %scale = [0 900];
        variabletitle = ' Static Temperature (K)';
    case 'total-temperature'
        %scale = [0 900];
        variabletitle = ' Total Temperature (K)';
    case 'viscosity-turb'
        variabletitle = ' Turbulent Viscosity (kg/m-s)';
        scale = [0 0.04];
    case 'n2'
        variabletitle = ' Mass Fraction of N';
        scale = [0 1];
end

%title(strcat('Contours of', variabletitle, ' -', casedescription),
'fontsize', sizeoftext)
%ylabel('Time (ms)', 'fontsize', sizeoftext)
%colorbar('EastOutside', 'fontsize', sizeoftext)
%NEW
title(strcat(casedescription), 'fontsize', sizeoftext)
xlabel('Time (ms)', 'fontsize', sizeoftext)

```

```

ylabel(variabletitle, 'fontsize', sizeoftext)
legend('x1','x2', 'x3', 'x4', 'Location','NorthEastOutside')
%END

%Set the limits of the plot, in x direction
%xlim(limitsofx)

%Set the color scale - prescribed in the second line of each case
switch above
%caxis(scale)

print(h, '-djpeg90', '-r600', char(variablename));

exportdata = [time', Z(:,1129), Z(:,404), Z(:,10), Z(:,1)];
exportdatafilename = char(strcat(datafilenamecommon, '-',
variablename, '.dat'));
save (exportdatafilename, 'exportdata', '-ASCII');

h=figure;
axes('fontsize', sizeoftext)
pcolor(shiftedposition, time, Z)
colormap(jet)
shading interp

xlabel('Distance from Valve (m)', 'fontSize', sizeoftext)
ylabel('Time (ms)', 'fontSize', sizeoftext)
colorbar('EastOutside', 'fontSize', sizeoftext)

%caxis(scale)

print(h, '-djpeg90', '-r300', char(variablename));

end

```

Function I: importfile.m

```
function importfile(fileToRead1)
%IMPORTFILE(FILETOREAD1)
% Imports data from the specified file
% FILETOREAD1: file to read

% Auto-generated by MATLAB on 15-Jul-2010 17:20:58

% Import the file
newData1 = importdata(fileToRead1);

% Create new variables in the base workspace from those fields.
vars = fieldnames(newData1);
for i = 1:length(vars)
    assignin('base', vars{i}, newData1.(vars{i}));
end
```

Function II: dataextract.m

```
function extracted = dataextract(dataset, positionvector)

% Extract a vector from a given column of the data set based on a
% position
% vector, discarding data points whose positions do not match the
% position
% vector
targetlength = length(positionvector);
%rawlength = length(dataset(:, columnnumber));
extracted = zeros(1, targetlength);

%icoordinates = dataset(:, 2:3);
%iposition = icoordinates(:, 1);
for i = 1:targetlength
    ipositionpointer = 1;
    %while and(not(abs(dataset(ipositionpointer, 1) -
positionvector(i)) < 0.001), (ipositionpointer < targetlength)),
    while not(abs(dataset(ipositionpointer, 1) - positionvector(i)) <
0.00001),
        ipositionpointer = ipositionpointer+1;
    end
    extracted(1, i) = dataset(ipositionpointer, 2);
end
```

Appendix H MATLAB Code to Generate x-t Contours and Extract Time History Data of Particle Variables

Main Program: DPMxtplotPrint.m

```
clear all;

% Set up the case, text to appear on title, injection time period and
% limits of x after shifting in position.
casedescription = ' N, 2MPa, 550C, Valve 0.6-5.6-0.6ms';
casename = '42';
sizeoftext = 20;
timestart = 0; timestep = 0.1; timeend = 66.7; timerepeat = 33.3;
xstart = -1.1; xstreams = 216; xend = 1.05;
limitsofx = [0 1];

diameter = [5 10 20 40]; diameters = length(diameter);
materials = 3;
material = {'a' 'c' 's'};
mfullname = {'Aluminum' 'Copper' 'Stainless Steel'};
mCp = [871 381 502.48];

% Set up constants and properties
F1 = 1.2; F2 = 0.3; TR = 293;
mTS = [110e6 250e6 500e6]; % material tensile strength
mTm = [933 1357 1783]; % material melting temperature
mrho = [2719 8978 8030]; % material density

position = (xstart: (xend-xstart)/(xstreams-1) :xend);
positioncount = length(position);
time = (timestart:timestep:timeend+timerepeat); timecount =
length(time); timeperiod = (timeend-timestart)/timestep;

particledata = importdata ('DPMdata.txt', '\t');
particlenames = importdata ('DPMnames.txt', '\t');

TEMP = zeros(materials, diameters, positioncount, timecount);
VELX = TEMP; TMPT10 = TEMP; TMPT09 = TEMP; VCR = TEMP; VRATIO = TEMP;
xtplotvar = zeros(positioncount, timecount);
xtexportvar = zeros(positioncount+1, timecount+1);
%VELM = TEMP;

PARTICLECOUNT = zeros(materials, diameters, positioncount);

% Shift zero in position axes on the start of the domain (after valve)
posmin = min(position);
```



```

shiftedposition = position - posmin;

xtexportvar(2:positioncount+1,1) = shiftedposition';
xtexportvar(1,2:timecount+1) = time;

for datarow = 1:length(particlenames)

    currentn = cell2mat(particlenames(datarow));

    currentm = find (char(material) == char(currentn(1)));

    dvalue = str2double(currentn(2:3));
    currentd = find (diameter == dvalue);

    currentx = sscanf(currentn(5:length(currentn)), '%d') + 1;

    PARTICLECOUNT(currentm, currentd, currentx) =
    PARTICLECOUNT(currentm, currentd, currentx) + 1;

    TEMP(currentm, currentd, currentx, PARTICLECOUNT(currentm,
    currentd, currentx)) = particledata(datarow, 5);
    VELX(currentm, currentd, currentx, PARTICLECOUNT(currentm,
    currentd, currentx)) = particledata(datarow, 2);

end

for period = 0:floor(timerepeat/(timeend-timestart))
    timerows = uint16(min((timeend-timestart)/timestep,1+(timerepeat-
    period*(timeend-timestart))/timestep));
    timetransferz = uint16((period+1)*timeperiod);
    TEMP(:, :, :, timetransferz+1:timetransferz+timerows) =
    TEMP(:, :, :, 1:timerows);
    VELX(:, :, :, timetransferz+1:timetransferz+timerows) =
    VELX(:, :, :, 1:timerows);
end

for currentm = 1:materials
    TMPT10(currentm, :, :, :) = TEMP(currentm, :, :, :) +
    1.0.*VELX(currentm, :, :, :).^2./(2*mCp(currentm));
    TMPT09(currentm, :, :, :) = TEMP(currentm, :, :, :) +
    0.9.*VELX(currentm, :, :, :).^2./(2*mCp(currentm));
    VCR(currentm, :, :, :) = sqrt(F1*4*mTS(currentm)*(1-
    (TEMP(currentm, :, :, :)-TR)/(mTm(currentm)-TR))/rho(currentm) +
    F2*mCp(currentm)*(mTm(currentm)-TEMP(currentm, :, :, :)));
    VRATIO = VELX ./ VCR;
end

dlmwrite(char(strcat(casename, '-shiftedposition.txt')), shiftedposition,
' ');
dlmwrite(char(strcat(casename, '-time.txt')), time, ' ');

```

```

for m = 1:materials
    for d = 1:diameters

        %TEMPERATURE
        xtplotvar(:, :) = TEMP(m,d, :, :);
        h=figure;
        axes('fontsize', sizeoftext)
        pcolor(shiftedposition, time, xtplotvar')
        colormap(jet)
        shading interp

        xlabel('Distance of Injection from Valve (m)', 'fontsize',
sizeoftext)
        ylabel('Time of Injection (ms)', 'fontsize', sizeoftext)
        %title(strcat('Temperature (K)', ', mfullname(m), ', ',
num2str(diameter(d)), 'micron'), 'fontsize', sizeoftext)
        colorbar('EastOutside', 'fontsize', sizeoftext)

        %Set the limits of the plot, in x direction
        %xlim(limitsofx)
        outputfilename = strcat(casename, 'Print-', material(m),
num2str(diameter(d)), 'Temperature');
        print(h, '-djpeg90', '-r300', char(outputfilename));
        xtexportvar(2:positioncount+1, 2:timecount+1) = xtplotvar;
        dlmwrite(char(strcat(outputfilename, '.txt')), xtexportvar, ' ');

        %SPEED
        xtplotvar(:, :) = VELX(m,d, :, :);
        h=figure;
        axes('fontsize', sizeoftext)
        pcolor(shiftedposition, time, xtplotvar')
        colormap(jet)
        shading interp

        xlabel('Distance of Injection from Valve (m)', 'fontsize',
sizeoftext)
        ylabel('Time of Injection (ms)', 'fontsize', sizeoftext)
        %title(strcat('Speed (m/s)', ', mfullname(m), ', ',
num2str(diameter(d)), 'micron'), 'fontsize', sizeoftext)
        colorbar('EastOutside', 'fontsize', sizeoftext)

        %Set the limits of the plot, in x direction
        %xlim(limitsofx)
        outputfilename = strcat(casename, 'Print-', material(m),
num2str(diameter(d)), 'Speed');
        print(h, '-djpeg90', '-r300', char(outputfilename));
        xtexportvar(2:positioncount+1, 2:timecount+1) = xtplotvar;
        dlmwrite(char(strcat(outputfilename, '.txt')), xtexportvar, ' ');

        %FINAL TEMPERATURE 100%CONVERSION
        xtplotvar(:, :) = TMPT10(m,d, :, :);

```

```

h=figure;
axes('fontsize', sizeoftext)
pcolor(shiftedposition, time, xtplotvar')
colormap(jet)
shading interp

xlabel('Distance of Injection from Valve (m)', 'fontsize',
sizeoftext)
ylabel('Time of Injection (ms)', 'fontsize', sizeoftext)
%title(strcat('Final Temp 1.0 (K)', ', mfullname(m)', ', ',
num2str(diameter(d)), 'micron'), 'fontsize', sizeoftext)
colorbar('EastOutside', 'fontsize', sizeoftext)

%Set the limits of the plot, in x direction
%xlim(limitsofx)
outputfilename = strcat(casename, 'Print-', material(m),
num2str(diameter(d)), 'FinalT10');
print(h, '-djpeg90', '-r300', char(outputfilename));
xtexportvar(2:positioncount+1,2:timecount+1) = xtplotvar;
dlmwrite(char(strcat(outputfilename, '.txt')), xtexportvar, ' ');

%FINAL TEMPERATURE 90%CONVERSION
xtplotvar(:, :) = TMPT09(m,d, :, :);
h=figure;
axes('fontsize', sizeoftext)
pcolor(shiftedposition, time, xtplotvar')
colormap(jet)
shading interp

xlabel('Distance of Injection from Valve (m)', 'fontsize',
sizeoftext)
ylabel('Time of Injection (ms)', 'fontsize', sizeoftext)
%title(strcat('Final Temp 0.9 (K)', ', mfullname(m)', ', ',
num2str(diameter(d)), 'micron'), 'fontsize', sizeoftext)
colorbar('EastOutside', 'fontsize', sizeoftext)

%Set the limits of the plot, in x direction
%xlim(limitsofx)
outputfilename = strcat(casename, 'Print-', material(m),
num2str(diameter(d)), 'FinalT09');
print(h, '-djpeg90', '-r300', char(outputfilename));
xtexportvar(2:positioncount+1,2:timecount+1) = xtplotvar;
dlmwrite(char(strcat(outputfilename, '.txt')), xtexportvar, ' ');

%CRITICAL VELOCITY
xtplotvar(:, :) = VCR(m,d, :, :);
h=figure;
axes('fontsize', sizeoftext)
pcolor(shiftedposition, time, xtplotvar')
colormap(jet)
shading interp

```

```

        xlabel('Distance of Injection from Valve (m)', 'fontsize',
sizeoftext)
        ylabel('Time of Injection (ms)', 'fontsize', sizeoftext)
        %title(strcat('Critical Velocity, ', mfullname(m), ', ',
num2str(diameter(d)), 'micron'), 'fontsize', sizeoftext)
        colorbar('EastOutside', 'fontsize', sizeoftext)

        %Set the limits of the plot, in x direction
        %xlim(limitsofx)
        outputfilename = strcat(casename, 'Print-', material(m),
num2str(diameter(d)), 'CritVel');
        print(h, '-djpeg90', '-r300', char(outputfilename));
        xtexportvar(2:positioncount+1,2:timecount+1) = xtplotvar;
        dlmwrite(char(strcat(outputfilename, '.txt')), xtexportvar, ' ');

        %VELOCITY RATIO
        xtplotvar(:, :) = VRATIO(m, d, :, :);
        h=figure;
        axes('fontsize', sizeoftext)
        pcolor(shiftedposition, time, xtplotvar)
        colormap(jet)
        shading interp

        xlabel('Distance of Injection from Valve (m)', 'fontsize',
sizeoftext)
        ylabel('Time of Injection (ms)', 'fontsize', sizeoftext)
        %title(strcat('Ratio Vp/Vcr, ', mfullname(m), ', ',
num2str(diameter(d)), 'micron'), 'fontsize', sizeoftext)
        colorbar('EastOutside', 'fontsize', sizeoftext)

        %Set the limits of the plot, in x direction
        %xlim(limitsofx)
        outputfilename = strcat(casename, 'Print-', material(m),
num2str(diameter(d)), 'VelRatio');
        print(h, '-djpeg90', '-r300', char(outputfilename));
        xtexportvar(2:positioncount+1,2:timecount+1) = xtplotvar;
        dlmwrite(char(strcat(outputfilename, '.txt')), xtexportvar, ' ');

        end
end

```

Vita Auctoris

NAME: Mohammad Karimi Esfahani

PLACE OF BIRTH: Tehran, Iran

YEAR OF BIRTH: 1982

EDUCATION: University of Windsor, Windsor
2003-2005 M.A.Sc

University of Tehran, Tehran
1999-2003 B.Sc.